Dissertation
submitted to the
Combined Faculties for the Natural Sciences and for Mathematics
of the Ruperto-Carola University of Heidelberg, Germany
for the degree of
Doctor of Natural Sciences

presented by

Dipl.Phys. Thomas Anker

born in Bishkek, Kyrgyz Republic

Oral examination: 16.11.2005

Ultracold quantum gases in one-dimensional optical lattice potentials
– nonlinear matter wave dynamics –

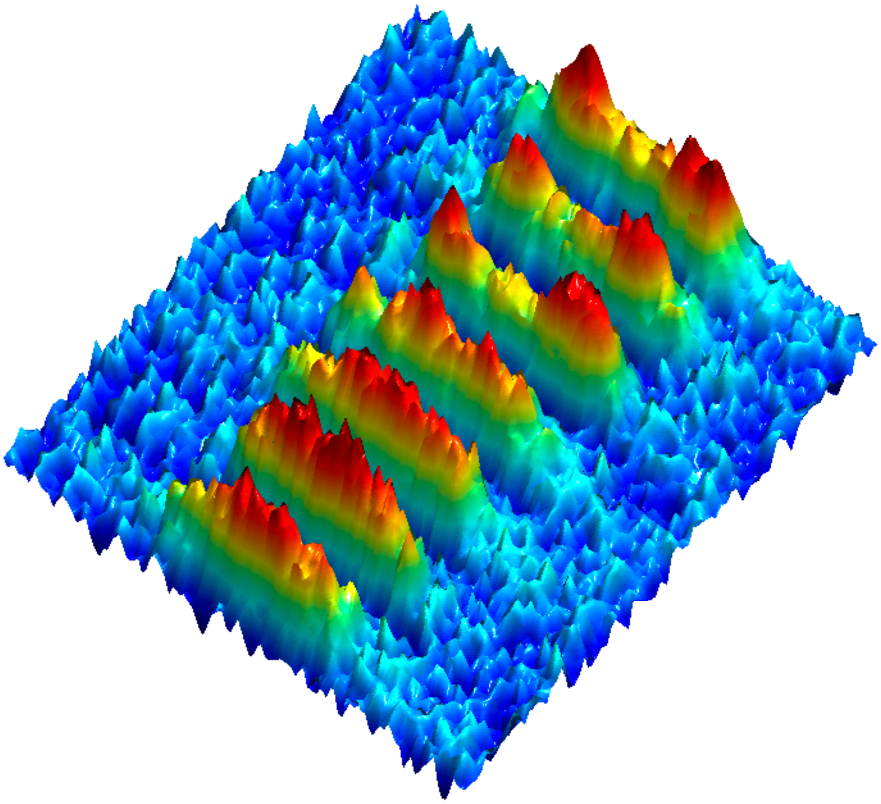

Referees:	Prof. M.K. Oberthaler Prof. J. Schmiedmayer

meiner Mutter

Zusammenfassung

In dieser Dissertation werden Experimente zur Quantendynamik von Materiewellen in einem eindimensionalen periodischen Potenzial vorgestellt. Ein ^{87}Rb Bose-Einstein Kondensat wird in einem eindimensionalen Wellenleiter im untersten Band eines überlagerten optischen periodischen Potenzials präpariert.

Durch die Wirkung eines schwachen periodischen Potenzials läßt sich die lineare Wellendispersion verändern. Wir konnten *Dispersionsmanagement* realisieren, indem wir während der Evolution von normaler zu anomaler Dispersion wechseln. Die anfängliche Expansion eines Wellenpaketes konnte zu einer Kompression umgekehrt und damit effektiv das Auseinanderlaufen verhindert werden. Mit dieser Kontrolle der Dispersion wurde es möglich erstmals *helle atomare Gap-Solitonen* – nicht auseinanderlaufende Wellenpakete – zu beobachten. Diese entstehen, wenn die Atomzahl und die Potenzialtiefe so eingestellt werden, dass die Wirkung der repulsiven Wechselwirkung von ^{87}Rb und die Wirkung der anomalen Dispersion sich kompensieren.

Für tiefe periodische Potenziale wird unser System von einer diskreten nichtlinearen Schrödingergleichung beschrieben, deren Dynamik durch das Tunneln zwischen den einzelnen Potenzialtöpfen und der nichtlinearen Phasenentwicklung bestimmt wird. Im Hauptteil dieser Arbeit berichte ich über die erstmalige experimentelle Beobachtung von *nichtlinearem Self-Trapping* von Materiewellen. Der Übergang vom diffusen Regime, charakterisiert durch eine stetige Expansion eines Wellenpaketes, in das Self-Trapping Regime wurde durch eine Erhöhung der atomaren Dichte realisiert. Die dadurch erhöhte repulsive Wechselwirkung führt dazu, daß die anfängliche Expansion stoppt und die Breite des Wellenpaketes endlich bleibt. Der Vergleich mit einer durchgeführten numerischen Analyse zeigt, dass die Wirkung der nichtlinearen Phasenentwicklung das Tunneln zwischen den einzelnen Gitterplätzen verhindert.

Abstract

In this thesis I report on experiments on the quantum dynamics of matter waves in a one-dimensional lattice potential. A ^{87}Rb Bose-Einstein condensates is prepared in a one-dimensional waveguide in the lowest band of a superimposed optical lattice potential.

The action of a weak lattice potential allows to modify the linear wave dispersion. We realized *dispersion management* by switching from normal to anomalous dispersion during the evolution. In this way the initial expansion of a wave packet is reversed to a compression and thus the effective spreading can be suppressed. By preparing a BEC at the Brillouin zone edge, we observed *bright atomic gap solitons* – non-spreading wave packets. They form, if the atom number and the lattice potential depth is tuned such that the effect of the repulsive atomic interaction and the anomalous dispersion cancel.

For deep lattice potentials our system is described by a discrete nonlinear Schrödinger equation, whose dynamics is determined by the tunneling between adjacent lattice sites and the nonlinear phase evolution. In the main part of this thesis I report on the first experimental observation of *nonlinear self-trapping* for matter waves. The transition from the diffusive regime, characterized by an continuous expansion of the condensate, to the self-trapping regime is accomplished by increasing the atomic density. Due to the corresponding increase of the repulsive atomic interaction the initial expansion stops and the width of the wave packet remains finite. The comparison with a numerical analysis reveals that the effect is due to an inhibition of the site-to-site tunneling induced by the nonlinear phase evolution.

Contents

1 Introduction

In the last year of high school our teacher told us that the picture of the world, which consists of countless particles that behave like billiard balls and move according to Newton's law is not complete. Even so Newton mechanics describes the "daily" or macroscopic world correctly, it fails, when looking at the fine details, the microscopic world. The dynamics of microscopic objects, such as electrons and atoms is of *wave nature* and is correctly described by quantum mechanics. This means that you can diffract atoms at a grating (Keith *et al.*, 1988) or perform Young's double-slit experiment with atoms (Carnal/Mlynek, 1991) just as you would do with light. At that time I was so fascinated by the technical and philosophical implications of this *quantum mechanical world picture* that I decided to study physics, instead of biology or medicine. During the time as a PhD student I had the chance to explore the field of atom optics, and thus could come very close to the heart of quantum mechanics.

Matter wave optics

The experiments described in this thesis are situated in the field of *nonlinear atom optics*. Here the role of matter and light is reversed in comparison to the field of light optics (Meystre, 2001). The wave fields are realized by atomic de Broglie waves and the components for the wave manipulation, such as lenses, mirrors, etc. are implemented with the help of electromagnetic fields. In the early experiments matter wave sources were realized by incoherent collimated atom beams, e.g. in neutral-atom lithography experiments (Timp *et al.*, 1992). The development of laser cooling and trapping (see e.g. Cohen-Tannoudji, 1998) allowed to realize bright sources of ultra cold, yet incoherent atoms.

Bose-Einstein condensates

With the realization of Bose-Einstein condensates (BEC) in dilute atomic gases (Anderson *et al.*, 1995; Davis *et al.*, 1995) nowadays a source of giant coherent matter waves is available. The realization of Bose-Einstein condensates is a step in technology, which is in close analogy to the advancement from the tungsten or arc-lamp to the light laser. BEC allows to realize the atom laser – a matter wave source with a coherence length (Andrews *et al.*, 1997) and a wavelength on the order of $1 - 100\,\mu$m. By introducing a loss in the atom trap, which corresponds to the cavity of a light laser, a pulsed (Mewes *et al.*, 1997) and a continuous (Bloch *et al.*, 1999) beam of coherent atoms could be realized.

Research field of coherent atom optics

In analogy to the invention of the light laser, the realization of BEC opened the wide and rich research field of coherent atom optics. Here only a glimpse of the research activity in connection with BEC is given.

Bose-Einstein condensates constitute a superfluid many-particle system. The investigation of the phenomenon of superfluidity in a BEC offers many advantages over the system of superfluid liquid Helium, since the atomic interaction is much weaker. E.g., the superfluid character of a BEC could be demonstrated easily by observing directly the formation of vortices (Madison *et al.*, 2000).

Due to the atomic interaction, Bose-Einstein condensates also allow for the investigation of nonlinear atom optics. In analogy to the field of nonlinear light optics, e.g. four-wave mixing with matter waves could be demonstrated (Deng *et al.*, 1999).

The low temperatures in a BEC allow for a detailed investigation of binary atomic collisions in the gas. This leads e.g. to the observation of Feshbach resonances in a Bose-Einstein condensate (Inouye *et al.*, 1998).

Whenever a new physical phenomenon is demonstrated, one of the first subsequent research activities is the realization of *detectors*, which utilize the new phenomenon. In the case of BEC this is e.g. the realization of interferometers (Shin *et al.*, 2004). The advantages of atom interferometers compared to optical ones are greater precision due to the large atomic mass, sensitivity to vibrations, inertial, and gravitational forces, access to quantum decoherence and to atomic scattering properties, etc. (Godun *et al.*, 2001).

The system of Bose-Einstein condensates in connection with optical lattice potentials allows for the investigation of the often mentioned field of quantum computing. One example is the implementation of quantum gates via cold controlled collisions between two atoms (Jaksch *et al.*, 1999).

BEC in optical lattices – a versatile model system

Our understanding of the physical world is based on abstract mathematical models we use to describe the reality. With these models it is also possible to discover unknown phenomena in the physical world by investigating the model itself with analytical or numerical mathematical tools. In order to fill these theoretical discoveries with life, *real* experimental systems are designed which demonstrate the discovered phenomena. In this context, ultra cold atoms in optical lattice potentials proved to be a very versatile model system to build *real artificial* crystals, i.e. systems of interacting waves in periodic potentials. The properties of these crystals allowed to directly demonstrate many phenomena, which were predicted theoretically in the field of solid state physics, e.g. the Quantum phase transition from a superfluid to a Mott insulator (Jaksch *et al.*, 1998; Greiner *et al.*, 2002).

From a different point of view, the system of BEC in optical lattices can also be seen as a quantum simulator for different differential equations, such as the different discrete Schrödinger equations or the Bose-Hubbard model !

Dispersion management and Solitons

In the domain of small nonlinear interaction the lattice potential and thus the lattice dispersion relation dominates the dynamics. Solid state physics text books tell us that the dispersion relation in a lattice potential is a periodic function with a band structure. The resulting dynamics is described by the group velocity, the dispersion, the inter band tunneling, etc. In a series of remarkable experiments, all these theoretical concepts could be visualized and thus provided a deeper understanding: Bloch oscillations (Dahan *et al.*, 1996), the momentum composition of Bloch states (Hecker *et al.*, 2002), the momentum distribution in different Bloch bands (Greiner *et al.*, 2001; Greiner, PhD thesis 2003) – just to mention a few.

In the first experiments described in this thesis, we explore the technical possibilities to control the dynamics of a ^{87}Rb BEC in a shallow 1D lattice potential prepared in the lowest Bloch band. Our key parameter is the precise position in quasi momentum space and thus the dispersion of the wave packet. In contrast to similar experiments, our setup allows a very long observation time, since the dynamics takes place in a horizontally oriented 1D waveguide.

We could demonstrate the technique of dispersion management for the first time for matter waves (Eiermann *et al.*, 2003; Anker *et al.*, 2003). After an initial expansion in the normal dispersion regime, the atomic wave packet is prepared in the regime of anomalous dispersion, where it compresses again. This technique, originally developed in the field of nonlinear fiber optics (Agrawal, 2001), allows to prevent the spreading of a wave packet.

For nonlinear wave systems, such as water waves in a channel (Russel, 1844) or laser light pulses in optical fibers (Agrawal, 1995), non-spreading localized wave packets – so called solitons – are known. Solitons form if the nonlinear dynamics compensates the spreading due to linear dispersion. By preparing a wave packet at the Brillouin zone boundary, we observed the formation of a bright atomic gap soliton (Eiermann *et al.*, 2004). The technical challenge for this realization was the preparation of atomic wave packets with only ~ 1000 atoms in a shallow lattice potential at the band edge of the lowest Bloch band.

Tunneling dynamics and nonlinear Self-trapping

For Bose-Einstein condensates trapped in a lattice potential, the dynamics depends strongly on the ratio between the kinetic energy and the interaction energy. In the case of deep lattice potentials, the kinetic energy is given by the nearest neighbor tunneling. The dynamical description changes therefore from a global *dispersion picture* to a local picture, where the main physical processes are the tunneling between adjacent lattice sites and the nonlinear phase evolution inside a single lattice site.

If the tunneling is large enough to allow a stable relative phase between two adjacent sites, the resulting dynamics is very similar to that of a Josephson current through a potential barrier between two superfluids (Cataliotti *et al.*, 2001).

In this thesis the dynamics of a Bose-Einstein condensate in a 1D waveguide with a superimposed deep 1D lattice potential is investigated. This setup is an experimental implementation of the well known dynamical system described by the discrete nonlinear Schrödinger equation (DNLS). Especially the transport properties of this system are of interest, e.g. the predicted existence of localized excitations such as discrete solitons (Ahufinger *et al.*, 2004; Trombettoni, 2001) and stable edges (Darmanyan *et al.*, 1999).

In this thesis the effect of nonlinear self-trapping, first predicted in (Trombettoni, 2001) could be demonstrated (Anker *et al.*, 2005). Increasing the nonlinearity the system is moved from the diffusive regime, characterized by an expansion of the condensate, to the nonlinearity dominated self-trapping regime, where the initial expansion stops and the width remains finite. The transition between both regimes is governed by a critical parameter, which can be identified by the ratio between the mean local interaction energy and the width of the lowest Bloch band.

In addition a detailed numerical investigation of the effect of nonlinear self-trapping is done, using discrete nonlinear Schrödinger equations with different nonlinearities. The analysis shows that nonlinear self-trapping is a local effect, which occurs due to nonlinearity induced inhibition of site to site tunneling. This behavior is closely connected to the phenomenon of macroscopic self-trapping for matter waves in double-well systems (Smerzi *et al.*, 1997; Albiez *et al.*, 2005). Finally the decay of self-trapping is investigated experimentally and compared with numerical calculations.

Overview

- The second chapter is an overview about the theory of a weakly interacting Bose gas, the experimental apparatus and experimental methods.
- The third chapter reports on experiments with matter waves in shallow 1D optical lattice potentials. The theory of the band structure of a lattice and the dispersive dynamics of matter waves is given. The experimental part describes the generation of optical lattice potentials, where the implemented calibration process of the lattice is of special interest. Since the demonstration of dispersion management and the realization of atomic gap solitons are described in detail in (Eiermann, PhD thesis 2004), in this thesis only a short introduction and a summary are given. The experiments on continuous dispersion management and their numerical analysis are presented in detail.
- In the fourth chapter, the effect of nonlinear self-trapping is presented. The Boson-Josephson junction and the discrete nonlinear Schrödinger equation is explained. A detailed numerical analysis of the effect of self-trapping is given. In the experimental part the realization of the transition from the diffusive to the self-trapping regime, the investigation of the scaling properties and the decay of self-trapping is presented and compared with the results of the numerical investigation.

Publications of the PhD Work

- *Dispersion Management for Atomic MatterWaves.*
  B. Eiermann, P. Treutlein, Th. Anker, M. Albiez, M. Taglieber, K.-P. Marzlin, and M. K. Oberthaler
  Physical Review Letters **91**, 060402 (2003)
- *Linear and nonlinear dynamics of matter wave packets in periodic potentials*
  Th. Anker, M. Albiez, B. Eiermann, M. Taglieber and M. K. Oberthaler
  Optics Express **12**, 11 (2003)
- *Bright Bose-Einstein Gap Solitons of Atoms with Repulsive Interaction*
  B. Eiermann, Th. Anker, M. Albiez, M. Taglieber, P. Treutlein, K.-P. Marzlin and M. K. Oberthaler
  Physical Review Letters **92**, 230401 (2004)
- *Nonlinear self-trapping of matter waves in periodic potentials*
  Th. Anker, M. Albiez, R. Gati, S. Hunsmann, B. Eiermann, A. Trombettoni and M. K. Oberthaler
  Physical Review Letters **94**, 020403 (2005)

2 Bose-Einstein condensation in a weakly interacting gas of atoms

Under certain experimental conditions massive matter like electrons, atoms or even very large molecules such as the C_{60} Buckminsterfullerene (Arndt *et al.*, 1999) exhibits a dynamics which is very similar to that of water waves or electro-magnetic waves. One thus has to attribute a wave character to matter – a fascinating idea both from a technical and philosophical point of view. In modern quantum mechanics textbooks this physical reality is described with the help of wave functions, which are governed by wave equations. These wave functions are very mathematical and abstract objects since the typical corresponding wavelength is so small that the resulting wave dynamics can often only be detected indirectly with a very sophisticated experimental apparatus and is thus *not* an every day experience.

With the realization of Bose-Einstein condensates in dilute atomic gases (Anderson *et al.*, 1995; Davis *et al.*, 1995) nowadays a bright source of giant coherent matter waves is available. The atomic matter waves generated from such condensates can be described by a single macroscopic wave function with typical length scales of several micrometers and thus allow to directly visualize and investigate quantum mechanical matter wave dynamics. The experimental realization (see e.g. Ketterle *et al.*, 1998) and the theoretical description (see e.g. Dalfovo *et al.*, 1999) of BEC in dilute atomic gases are now very well understood. They are used in many laboratories as a standard source for coherent matter wave optics experiments. With the help of laser light fields and magnetic fields it is now possible to realize atom optical components such as waveguides, mirrors, lenses, cavities etc. In addition, the weak interaction between the atoms leads to a nonlinear wave dynamics and thus opens up the rich field of nonlinear matter wave optics.

In the experiments described in this thesis ^{87}Rb Bose-Einstein condensates are used as a source of coherent matter wave packets to investigate nonlinear matter wave dynamics in a periodically modulated waveguide. The theoretical description as detailed as is necessary to understand the experiments is given in the first part of this chapter. As the main result the relevant nonlinear dynamical equation for the experimental system, the Gross-Pitaevskii equation (GPE), is explained. Also the reduced equations for the description of the (quasi) 1D dynamics in a waveguide and the method for their numerical propagation is given.

In the second part, the used experimental setup for the creation of the condensates is described. The experimental setup allows to capture and pre-cool atoms with a magneto-optical Funnel-MOT system and to further cool them in a magnetic trap. The final condensation is achieved in a purely optical trap consisting of two crossed laser beams. The setup provides atomic wave packets with very well controlled atom number and shape. The further manipulation of the wave packets by optical means proved to be very versatile allowing for the implementation of many different potentials.

2.1 Theory of Bose-Einstein condensates

The phenomenon of Bose-Einstein condensation was first predicted in (Bose, 1924; Einstein, 1925) for an ideal gas of bosonic particles and occurs when the gas is cooled below a critical temperature. In a Bose condensed gas the ground state of the system is occupied by a macroscopic number of atoms. BEC is a paradigm of quantum statistical mechanics and is due to the indistinguishability and wave nature of particles. The description of BEC for noninteracting particles is given in the first part of this section.

In real physical systems the atomic interaction changes the description of BEC drastically. In contrast to the complex situation of strongly interacting superfluid ^{4}He (London, 1938), BEC in dilute gases can be described very accurately in the framework of the Gross-Pitaevskii equation (see e.g. Dalfovo *et al.*, 1999), which is based on a mean field theory. The GPE for a 3D system and for the 1D waveguide system, as well as the numerical implementation is shown in the second and third part of this section.

2.1.1 Noninteracting gas of bosons

A many-particle system of identical bosons follows two important quantum statistical rules. First of all bosons do not underly the Pauli exclusion principle and are thus allowed to accumulate in a single state φ_j of the system. In addition the many-body wave function of the system does not change, when the position of two particles is exchanged

$$|\varphi_j \varphi_i \varphi_j \varphi_j ...\rangle = |\varphi_i \varphi_j \varphi_j \varphi_j ...\rangle. \tag{2.1}$$

The consequences of these two rules become important, when the lowest quantum states φ_j are populated with more than one particle. This happens, when the system is cooled below the critical temperature. For a system of N bosons in a harmonic trap the critical temperature is given by (see e.g. Dalfovo *et al.*, 1999)

$$T_{\mathrm{c}} = \frac{\hbar}{k_B} \omega_{\mathrm{ho}} \left(\frac{N}{\zeta(3)} \right)^{1/3}, \tag{2.2}$$

where $\omega_{\mathrm{ho}} = (\omega_x \omega_y \omega_z)^{1/3}$ is the geometric average of the oscillator frequencies and $\zeta(3) = 1.2$ is the Riemann zeta function. At the critical temperature the thermal de Broglie wavelength of the particles becomes comparable to the mean inter-particle distance and thus the bosons start to overlap, i.e. the lowest quantum states φ_j are populated with more than one particle. At this point the quantum statistics, governed by the rules given above, leads to the phenomenon of Bose-Einstein condensation: in thermal equilibrium (maximum Entropy) the ground state φ_0 of the system is macroscopically populated and the energy is distributed between the remaining atoms, which populate many high energy states. At $T = 0$ all the particles are in the ground state and the many-body wave function is a product of N identical single-particle ground state wave functions. Such a condensate can be described by a macroscopic wave function (order parameter)

$$\psi(\vec{r}) = \sqrt{N} \varphi_0(\vec{r}), \tag{2.3}$$

which is governed by the linear Schrödinger equation

$$i\hbar\frac{\partial}{\partial t}\psi(\vec{r},t) = \hat{H}\psi(\vec{r},t) = \left[-\frac{\hbar^2}{2m}\nabla^2 + V_{\text{ext}}(\vec{r})\right]\psi(\vec{r},t). \tag{2.4}$$

For a typical harmonic trapping potential $\varphi_0(\vec{r})$ is a Gaussian function with a length scale of several micrometer.

2.1.2 Dilute gas of interacting bosons

The many-body Hamiltonian for a system of N interacting bosons in an external trapping potential V_{ext} is given, in second quantization, by

$$\begin{aligned}\hat{H} = \int d\vec{r}\,\hat{\Psi}^\dagger(\vec{r})\left[-\frac{\hbar^2}{2m}\nabla^2 + V_{\text{ext}}(\vec{r})\right]\hat{\Psi}(\vec{r}) + \\ \frac{1}{2}\int d\vec{r}\,d\vec{r}\,'\hat{\Psi}^\dagger(\vec{r})\hat{\Psi}^\dagger(\vec{r}\,')V(\vec{r}\,'-\vec{r})\hat{\Psi}(\vec{r})\hat{\Psi}(\vec{r}\,'),\end{aligned} \tag{2.5}$$

where $\hat{\Psi}^\dagger(\vec{r})$ and $\hat{\Psi}(\vec{r})$ are the boson field operators, that create and annihilate a particle at the position $\vec{r}$, respectively, and $V(\vec{r}\,'-\vec{r})$ is the two-body interatomic scattering potential. For a dilute gas at very low temperatures the atomic interaction is given by binary collisions at low energy. This allows to replace the complicated interaction potential $V(\vec{r}-\vec{r}\,')$ by an effective interaction

$$V(\vec{r}\,'-\vec{r}) = g_0\delta(\vec{r}\,'-\vec{r}), \tag{2.6}$$

characterized by the coupling constant $g_0 = 4\pi\hbar^2 a_s/m$ with the s-wave scattering length a_s. This approximation is valid in the case that the scattering length is much smaller than the inter-particle distance, i.e. $na_s^3 \ll 1$ and n is the mean particle density.

For a Bose condensed gas, a mean field approach, which consists in separating out the condensate contribution to the bosonic field operators (Bogoliubov, 1947) can be applied. In general the field operators can be written as $\hat{\Psi}(\vec{r}) = \sum_\alpha \Psi_\alpha(\vec{r})a_\alpha$, where $\Psi_\alpha(\vec{r})$ are the single particle wave functions and a_α are the corresponding annihilation operators. In a Bose-Einstein condensate the number of atoms in the ground state becomes very large $N_0 \gg 1$ and, consequently, the operators a_0 and $a_0^\dagger$ can be treated like c-numbers: $a_0|N_0\rangle = \sqrt{N_0}|N_0-1\rangle \simeq a_0^\dagger|N_0\rangle = \sqrt{N_0+1}|N_0+1\rangle \simeq \sqrt{N_0}|N_0\rangle$. The bosonic field operator can then be written as $\hat{\Psi}(\vec{r}) = \Psi_0(\vec{r})\sqrt{N_0}$. In the general case of a time-dependent system, assuming the occurrence of a broken gauge symmetry in the many-body system, the bosonic field operator can be replaced by its expectation value $\hat{\Psi}(\vec{r},t) = \Psi(\vec{r},t) \equiv \langle\hat{\Psi}(\vec{r},t)\rangle$. This approximation together with 2.6 and 2.5 leads to the well known Gross-Pitaevskii equation (GPE)

$$i\hbar\frac{\partial}{\partial t}\Psi(\vec{r},t) = \left[-\frac{\hbar^2}{2m}\nabla^2 + V_{\text{ext}}(\vec{r}) + g_0N|\Psi(\vec{r},t)|^2\right]\Psi(\vec{r},t). \tag{2.7}$$

It has the form of a nonlinear Schrödinger equation, where the nonlinearity is coming from the mean-field term, which is proportional to the particle density $n(\vec{r}) = |\Psi(\vec{r},t)|^2$. Eq. 2.7 allows to describe, both qualitatively and quantitatively, the macroscopic behavior of a Bose-Einstein condensate on a length scale larger than the mean interatomic distance. From a many body point of view, the mean field description with eq. 2.7 is the simplest of all possible cases, containing no interaction-induced correlations between different atoms. The importance of direct interaction can be estimated from the ratio

$$\gamma = \frac{\epsilon_{\text{int}}}{\epsilon_{\text{kin}}} = \frac{g_0 n}{\hbar^2 n^{2/3}/m} \approx n^{1/3} a_s \tag{2.8}$$

between the interaction and the kinetic energy per particle (Zwerger, 2003). For the typical atomic densities n in the experiments described in this work, the average inter particle distance $n^{1/3}$ is much larger than the scattering length a_s and thus $\gamma \ll 1$. In this weak coupling limit the dynamics of the many body wave function is well described by a single macroscopic wave function and the Gross-Pitaevskii equation 2.7, which is used as the fundamental dynamical equation in the description of the experiments presented in this thesis.

2.1.3 A BEC in a harmonic 1D waveguide potential

In the experiment described in this work the dynamics of a coherent matter wave packet in a horizontal 1D waveguide potential is investigated. The waveguide can be described by a harmonic potential

$$V_{\text{wg}} = \frac{m}{2}\omega_\perp^2 (y^2 + z^2) + \frac{m}{2}\omega_\parallel^2 x^2, \tag{2.9}$$

with the transversal and longitudinal trapping frequencies $\omega_\perp$ and $\omega_\parallel$, respectively. In the experiments $\omega_\parallel \ll 2\pi/T_{\text{exp}}$, where T_{exp} is the time scale of the wave packet dynamics. Thus a free evolution in the longitudinal direction is realized.

In the experiments atomic wave packets are used with small atom numbers, such that corresponding interaction energy $g_0 N |\Psi(\vec{r},t)|^2 \leq \hbar\omega_\perp$ is smaller than the transverse vibrational level spacing. The resulting dynamics will thus be reduced to one dimension in longitudinal direction, whereas the transverse motion is almost frozen out. This situation is described by the 1D Gross-Pitaevskii equation, which is derived in the first part of this section.

For intermediate atomic densities with $g_{1\text{D}} N |\Psi(x,t)|^2 \geq \hbar\omega_\perp$, an effective 1D equation is described in the second part. It models the longitudinal wave packet dynamics with a nonlinear coupling constant $g_{1\text{D}}(x,t)$, which is implicitly time- and space-dependent through the local atomic density $N|\Psi(x,t)|^2$.

In the last part of this section the numerical implementation of both equations of motion is described.

1D Gross-Pitaevskii equation

We consider matter wave experiments with small atomic densities, such that the corresponding energies due to the atomic interaction are smaller or on the order of the transverse vibrational level spacing $g_0 N |\Psi(\vec{r},t)|^2 \leq \hbar\omega_\perp$. In this case, the condensate wave function can be approximated by a product wave function $\Psi(\vec{r},t) = \Psi(x,t)\Psi_\perp(y)\Psi_\perp(z)$, where $\Psi_\perp$ is the ground state wave function of the harmonic oscillator. In this approximation the nonlinear coupling of the longitudinal and transversal degrees of freedom is neglected and the wave function is assumed to remain always in the transversal ground state. This ansatz is plugged into eq. (2.7) and by integrating out the transverse degrees of freedom, the 1D Gross-Pitaevskii equation

$$i\hbar\frac{\partial}{\partial t}\Psi(x,t)=\left[-\frac{\hbar^2}{2m}\frac{\partial^2}{\partial x^2}+V_{\mathrm{wg}}(x)+g_{1\mathrm{D}}N|\Psi(x,t)|^2\right]\Psi(x,t). \tag{2.10}$$

is obtained. Here $g_{1\mathrm{D}}=g_0/A_\perp$ and

$$A_\perp=\left[\int dydz|\Psi_\perp(y)|^4|\Psi_\perp(z)|^4\right]^{-1}=2\pi a_\perp^2 \tag{2.11}$$

is a measure for the transversal width of the wave function, where $a_\perp=\sqrt{\hbar/m\omega_\perp}$ is the width of the transverse ground state. The above stated criterium for the used approximation can now be written as

$$g_{1\mathrm{D}}N|\Psi(x,t)|^2\leq\hbar\omega_\perp\Leftrightarrow N\max\{|\Psi_\perp(x,t)|^2\}\leq\frac{1}{2a_s}, \tag{2.12}$$

In order for the wave function to remain always in the transversal ground state, the longitudinal atomic density must not exceed $1/2a_s$ (= 93 atoms/μm for ^{87}Rb). Please note that this limit of the linear density does not depend on the transversal trapping frequency $\omega_\perp$.

Effective 1D Schrödinger equation

For intermediate atomic densities $g_{1\mathrm{D}}|\Psi(x,t)|^2\geq\hbar\omega_\perp$ the transversal ground state can no longer be described by the ground state of the harmonic oscillator. The mean field pressure due to the repulsive atomic interaction leads to a broadening of the wave function. In steady state, the ground state can still be approximated by a Gaussian density distribution $\Psi_\perp(y)\propto\exp(-y^2/\sigma_\perp^2)$. The width $\sigma_\perp$ depends on the density of the wave packet and is obtained by a variational principle (Baym/Pethick, 1996).

A dynamic equation of motion can be derived, in the case that the density of the wave packet changes only slowly with respect to the transverse trapping frequency $dn(x)/dt<\omega_\perp$. The wave function will then remain in the transverse ground state with a time-dependent width $\sigma_\perp(t)$. In (Salasnich *et al.*, 2002) the effective 1D nonlinear Schrödinger equation

$$\begin{aligned}i\hbar\frac{\partial}{\partial t}\Psi(x,t)=&\left[-\frac{\hbar^2}{2m}\frac{\partial^2}{\partial x^2}+V_{\mathrm{ext}}(x)+g_{1\mathrm{D}}N\frac{|\Psi(x,t)|^2}{\sqrt{1+2a_sN|\Psi(x,t)|^2}}\right]\Psi(x,t)\\&+\left[\frac{\hbar\omega_\perp}{2}\left(\frac{1}{\sqrt{1+2a_sN|\Psi(x,t)|^2}}+\sqrt{1+2a_sN|\Psi(x,t)|^2}\right)\right]\Psi(x,t)\end{aligned} \tag{2.13}$$

is derived, based on the above assumptions. This equation is called non-polynomial nonlinear Schrödinger equation (NPSE). It allows to describe the dynamics of atomic wave packets in a 1D waveguide potential, where the dynamics takes place mainly in the axial direction. In the radial direction the wave function is assumed to remain in the ground state with a Gaussian density distribution, where the width $\sigma_\perp(x,t)^2=a_\perp^2\sqrt{1+2a_sN|\Psi(x,t)|^2}$ adjusts instantaneous according to the local density.

2.1.4 Numerical wave packet propagation in 1D

In this thesis physical insight into the dynamics of wave packets is gained by comparison with corresponding numerical calculations. The numerical propagation of wave packet dynamics in 3 dimensions requires very large computational resources. Regarding the experiments with wave packets in a 1D waveguide, already the propagation of the (effective) 1D Schrödinger equation, which requires only small computational resources, allows to reproduce the main aspects of the dynamics. In this section the implementation of the numerical propagation of the nonlinear 1D Schrödinger equations is described.

The evolution of a quantum mechanical state is determined by the time evolution operator $\hat{U}(t_0, t)$ (see e.g. Nolting, 1997):

$$\Psi(x,t) = \hat{U}(t_0,t)\Psi(x,t_0). \tag{2.14}$$

For conservative systems $\hat{U}(t_0,t) = \exp(-\frac{i}{\hbar}\hat{H}\Delta t)$, where $\Delta t = t - t_0$. Eq. 2.14 can be solved numerically with a split-step Fourier method ("spectral method") (Sterke/Sipe, 1986). In this method the Hamiltonian operator is split into the kinetic and the spatial part $\hat{H} = H_p(\hat{p}) + H_x(\hat{x},t)$ and the time evolution operator is approximated by

$$\hat{U}(t_0,t) = \exp(-\frac{i}{\hbar}\hat{H}\Delta t) \simeq \exp(-\frac{i}{\hbar}H_p\Delta t/2)\cdot\exp(-\frac{i}{\hbar}H_x\Delta t)\cdot\exp(-\frac{i}{\hbar}H_p\Delta t/2). \tag{2.15}$$

Here an error is introduced due to the fact that $[\hat{x},\hat{p}] \neq 0$. The symmetric splitting of the operators reduces the error to order Δt^3. In the numerical propagation the time interval is split into small steps $\Delta t = N_{\mathrm{st}} \cdot dt$, such that the error becomes negligible.

Both the kinetic and the spatial part of the time evolution operator can be evaluated by a simple multiplication in momentum and in real space, respectively. The switching between momentum and real space can be implemented very efficiently by a fast-fourier transformation (FFT). Thus a single propagation step is reduced to 2 FFT's and two multiplications. The complete propagation is given by

$$\Psi(x,t) = \hat{P}_{1/2}\hat{X}[\hat{P}\hat{X}]^{N_{\mathrm{st}}-1}\hat{P}_{1/2}\Psi(x,t_0), \tag{2.16}$$

where

$$\begin{aligned} \hat{P}_{1/2} &= (FFT)^{-1}e^{-\frac{i}{\hbar}E(p)dt/2}\,FFT \\ \hat{P} &= (FFT)^{-1}e^{-\frac{i}{\hbar}E(p)dt}\,FFT \\ \hat{X} &= e^{-\frac{i}{\hbar}E(x,t)dt}. \end{aligned} \tag{2.17}$$

$E(p)$ is the dispersion relation and $E(x,t)$ is determined by the external potentials (harmonic trap and/or periodic potential) and the density dependent mean field energy due to the atomic interaction. Thus $E(x,t)$ needs to be evaluated for each step[1]. An example program for the propagation of the NPSE in the programming language Matlab© is given in appendix A.1.

---

[1] In this way also time-dependent external potentials can be implemented easily.

2.2 Experimental setup to create a ^{87}Rb Bose-Einstein condensate

Bose-Einstein condensates of a an interacting gas of bosons are produced, as explained in the previous section, by increasing the phase-space density of the gas above a critical value. In a typical experiment this is achieved by trapping the gas in tight conservative atom trap with small heating. The phase transition to obtain a condensate is then realized by cooling the gas below the critical temperature, mostly with a series of different cooling techniques. An overview of the different implementations can be found in (see e.g. Ketterle *et al.*, 1998).

For the reader already familiar with this field a short summary of the setup used in this thesis is given in the first section. For the reader interested in the details of the implemented scheme, the trapping, cooling, detection and experiment control is described in the remaining sections. Additional technical details can be found in (Eiermann, PhD thesis 2004).

2.2.1 Setup summary

A gas of bosonic ^{87}Rb atoms is used in the experiment. This atomic species is the "workhorse" in the field of atom optics, since it can be held conveniently in a magnetic and in an optical trap and very efficient cooling techniques, like laser-cooling and evaporation cooling can be employed. The experimental setup consist of a double chamber vacuum system. A slow beam of atoms is produced by a magneto-optical funnel in the high vacuum chamber, and is injected into the ultra high vacuum chamber, where the atoms are trapped and precooled in a magneto-optical trap. Subsequently the atoms are transferred into a superimposed magnetic trap, where the temperature is further reduced by evaporative cooling. The gas of ultra cold atoms is then transferred into an optical trap, where the gas is cooled below the critical temperature again by evaporative cooling. The optical trap consists of two crossed laser beams, where one of the beams acts as a waveguide. The nonlinear matter wave dynamics of the condensate in the waveguide is observed by absorption imaging. In Fig 2.1 the schematic setup together with the laser system are shown.

2.2.2 Magneto-optical cooling and trapping

In the experiments on matter wave optics described in this thesis, light, i.e. the interaction of atoms with an electro-magnetic field, is used in order to create, manipulate and detect the matter waves. The basic processes of the interaction of atoms with light, i.e. absorption and emission of photons, allow to distinguish two categories of effects (see e.g. Cohen-Tannoudji, 1998): dissipative (or absorptive) and reactive (or dispersive) effects.

The interaction of atoms with laser modes with a frequency ω_l, which is far detuned from the atomic resonance frequency ω_0, is mainly governed by the redistribution of photons between the laser modes in stimulated absorption-emission cycles. These processes lead to the so called reactive (or dipole) force, which is used in the experiments to realize a conservative optical trap and a periodically modulated waveguide for the atoms (see section on the optical trap and chapter 3).

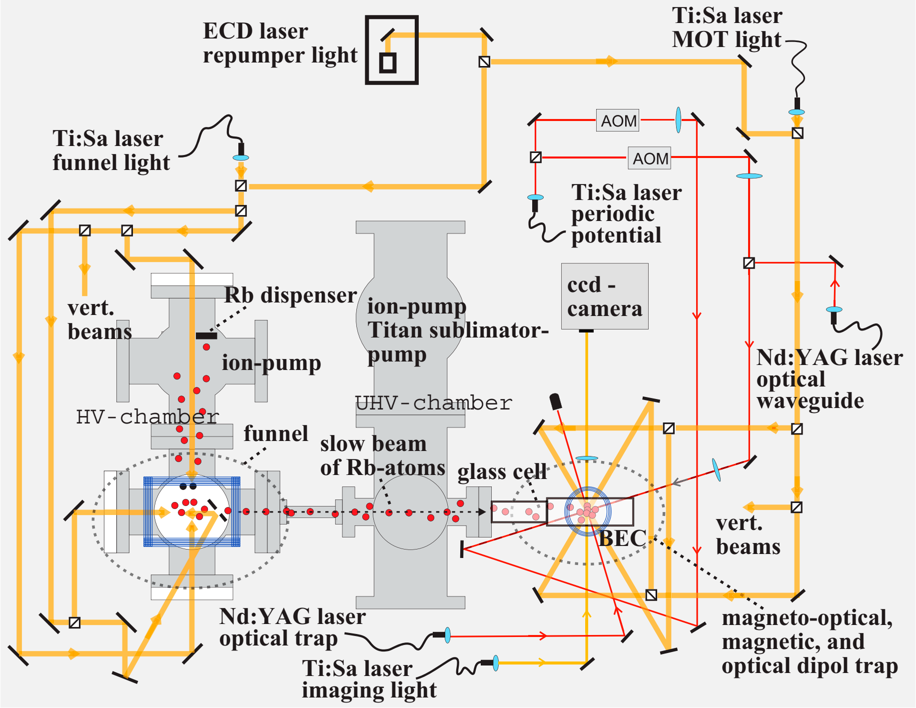

Figure 2.1: Schematic Setup of the experiment and laser system. The matter wave experiments with a Bose-Einstein condensate are realized in a vacuum system consisting of two chambers. The HV chamber (on the left, 10^{-9} mbar) and the UHV chamber (on the right, $< 2 \cdot 10^{-11}$ mbar) are connected by a differential pumping stage (500:1). In the HV chamber a ^{87}Rb background gas is produced with Rb dispensers. In a 2D magneto-optical trap (funnel) the atoms are cooled and compressed onto the symmetry axis of the funnel and pushed in the direction of the axis through a hole in one of the funnel mirrors into the UHV chamber. The resulting beam of slow atoms is captured and precooled in a 3D magneto-optical trap in the UHV chamber. A Ti:Saphire laser and a ECD laser provide the main- and the repumper-light for the MOT and the funnel. The atoms are transferred from the MOT into a superimposed magnetic time-orbiting trap, where they are further cooled by evaporative cooling. A sample of ultra-cold atoms is finally transferred into an optical dipole trap, realized with two crossed beams from a Nd:YAG laser. By further evaporative cooling a Bose-Einstein condensate is produced and its dynamics along the waveguide is detected by absorption imaging with a CCD-camera. An additional standing light wave, collinear with the waveguide, is used to realize and investigate matter wave dynamics in a periodic potential.

When atoms interact with almost resonant laser modes, the coupling of the atoms to the empty vacuum modes of the light field becomes important. An atom, which absorbs a photon from a single resonant laser mode with wave vector $\vec{k}_l$ experiences a momentum transfer of $\hbar\vec{k}_l$. The subsequent emission of the photon into one of the resonant vacuum modes is isotropic and thus, for many absorption-emission cycles, a net force (Cohen-Tannoudji *et al.*, 1992)

$$\vec{F}_{\mathrm{sc}} = \sigma_{\mathrm{ex}}\Gamma \cdot \hbar\vec{k}_l \tag{2.18}$$

is exerted onto the atom. It is called scattering (or dissipative) force and is proportional to the natural line width Γ and the occupation probability $\sigma_{ex}(\delta_l, I)$ of the excited state.

The force 2.18 depends on the detuning $\delta_l = (\omega_l - \omega_0)$ and the laser light intensity I. Together with the Zeeman-splitting in magnetic fields and the Doppler-shift for moving atoms, very efficient optical cooling and magneto-optical atoms traps (MOT) can be realized.

Optical cooling can be implemented by a configuration of counterpropagating waves, which are slightly red detuned from the atomic resonance frequency. For moving atoms, the apparent laser frequency is Doppler shifted and thus the wave with the opposite direction to the atomic velocity is closer to resonance. The net force is opposite to the atom velocity and can be written for small velocities as a friction force, which is proportional to the velocity of the atom. A system of three mutually orthogonal pairs of counterpropagating waves is called "optical molasses"(Chu *et al.*, 1985) and allows to cool the atoms down to the Doppler temperature limit $T_D = \frac{\hbar\Gamma}{2k_B}$. In such a system of counterpropagating waves an additional cooling mechanism results from the spatially dependent polarization of the optical field. This "polarization gradient cooling" (Dalibard *et al.*, 1989) allows to cool far below the Doppler limit.

By adding a suitable magnetic field to the "optical molasses" configuration, a spatial dependence of the scattering force is introduced, which allows to realize a 3D magneto-optical trap (MOT) combined with optical cooling. The principle configuration of a such a MOT is shown in Figure 2.2.

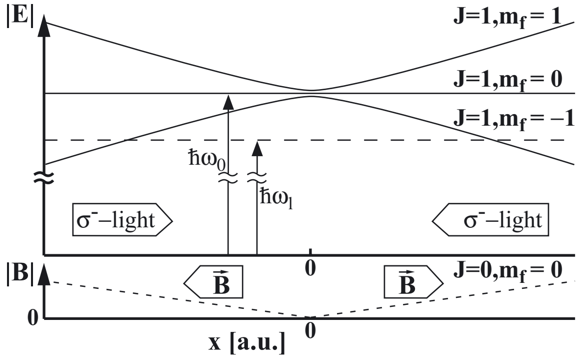

Figure 2.2: Light and magnetic field configuration of a 1D magneto-optical trap. The magnetic field leads to a spatially varying Zeeman shift of the excited state. Two right hand circular polarized counterpropagating light waves, which are slightly red detuned from the atomic resonance, exert opposing scattering forces on the atoms. In the center of the trap, both forces are balanced, whereas for atoms, which are not situated in the center of the trap, the σ^--transition, and thus the force directed towards the center of the trap is dominant.

Level scheme of ^{87}Rb

The ^{87}Rb isotope, which is used in the experiment, is an alkali atom with a nuclear spin I = 3/2. The fine structure splitting due to spin-orbit coupling leads to the D-line doublet $5^2S_{1/2} - 5^2P_{1/2}$ and $5^2S_{1/2} - 5^2P_{3/2}$, with transition wavelengths of 795 nm and 780 nm respectively. Coupling to the nuclear spin then leads to a hyperfine splitting of the ground state of about 6.8 GHz and a splitting of the excited states on the order of hundred MHz. In figure 2.3 the relevant part of the level scheme for ^{87}Rb is shown. For the optical cooling and trapping the $|F = 2\rangle$ to $|F' = 3\rangle$ transition (D2-line at 780 nm) is used. Additional repumper light for the $|F = 1\rangle$ to $|F' = 2\rangle$ is necessary, in order pump atoms, which decayed from the near resonant $|F = 2\rangle$ state into the $|F = 1\rangle$ state, back into the cooling cycle. The optical waveguide and the periodic potential are realized with off-resonant laser light at 1064 nm and 782 nm, respectively. The Bose-Einstein condensate is created in the $|F = 2, m_F = 2\rangle$ state (in the optical dipole trap a small magnetic guiding field conserves the spin polarization).

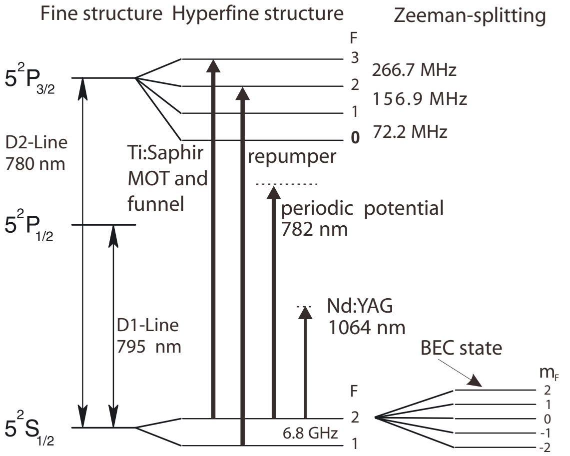

Figure 2.3: Level scheme of ^{87}Rb.

Magneto-optical funnel

In the experiment a 2D magneto-optical funnel is used in the HV chamber in order to realize a slow beam of ^{87}Rb atoms, which is directed through the hole of the differential pumping stage connecting the HV and the UHV chamber (see figure 2.1). It consists of three mutually orthogonal pairs of counterpropagating laser beams and a magnetic axial quadrupole field (see figure 2.4). In the transverse directions, the polarization and intensity of the laser beams is chosen such that a MOT configuration is realized. Thus, atoms are captured and compressed to the symmetry axis of the magnetic field. In the axial direction, due to the vanishing magnetic field gradient, the atoms are only optically cooled. In addition, as the laser beams in the axial direction are slightly unbalanced, the atoms are pushed along the axis in one direction. Such a magneto-optical funnel was first demonstrated in (Riis *et al.*, 1990) and later used in a Bose-Einstein experiment setup (Dieckmann *et al.*, 1998). The laser light for the funnel drives the $|F = 2\rangle$ to $|F' = 3\rangle$ transition (D_2-line) and is detuned by $\delta_l = -2\Gamma$. The slow beam of atoms is captured in the UHV chamber by a 3D MOT with a typical loading rate of 10^7 atoms/s.

Magneto-optical trap

The atomic beam from the funnel is captured in the UHV chamber by a standard 3D MOT (Raab *et al.*, 1987). The schematic setup is shown in figure 2.5. The figure of

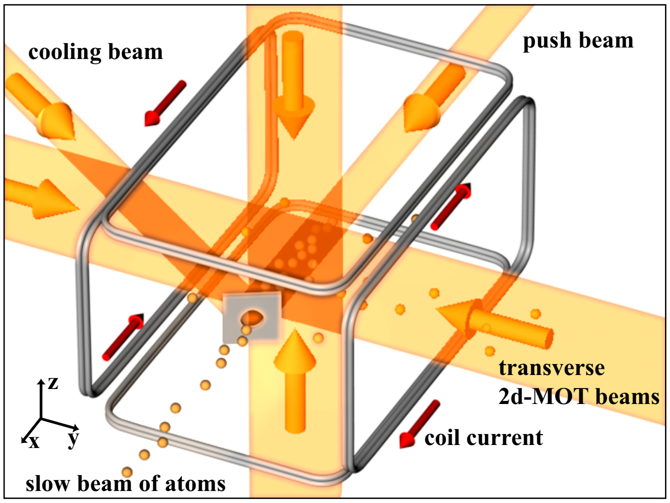

Figure 2.4: Schematic setup of the magneto-optical funnel. Two pairs of elongated rectangular coils in anti-Helmholtz configuration generate an axial quadrupole field. In the transverse direction (y-,z-direction) two orthogonal pairs of counter propagating laser beams realize a 2D MOT configuration, which allows to trap the atoms from the background and compress them onto the symmetry axis of the funnel. In the longitudinal direction a push and a cooling beam are reflected off a mirror inside the HV chamber. A hole in the mirror (which constitutes the differential pumping stage between the HV and the UHV chamber) leads to an unbalanced light force configuration on the axis and generates a beam of slow atoms.

merit for the MOT in this Bose-Einstein experiment is to collect and precool as many atoms as possible. This is achieved by trapping the atoms in a large volume, in order to avoid trap losses due to inelastic, light-induced collisions. In the setup, beam diameters of 18 mm are used to realize a large capture volume of the trap. In addition, the coils for the rotating bias field (see next section on the top trap) are run, in order to reduce the gradient of the magnetic field in the center of the MOT. The laser light for the MOT drives the $|F=2\rangle$ to $|F'=3\rangle$ transition (D_2-line) and is detuned by $\delta_l = -1.4\Gamma$. A number of 10^9 atoms in the MOT were sufficient to reliably create Bose-Einstein condensates.

2.2.3 Magnetic TOP-trap and evaporative cooling

Dissipative optical cooling methods are not sufficient to reach high enough phase-space densities necessary for Bose-Einstein condensation. The final step, in order to realize the Bose-Einstein condensation is realized by a transfer of the atomic sample into a conservative atom trap and subsequent cooling by evaporation (Masuhara *et al.*, 1988).

Evaporative cooling

Evaporative cooling can be implemented for atoms in a conservative atom trap with a variable trap depth. By lowering the trap depth, the high energy tail of the thermal distribution is continuously removed. As each evaporated atom carries away more than

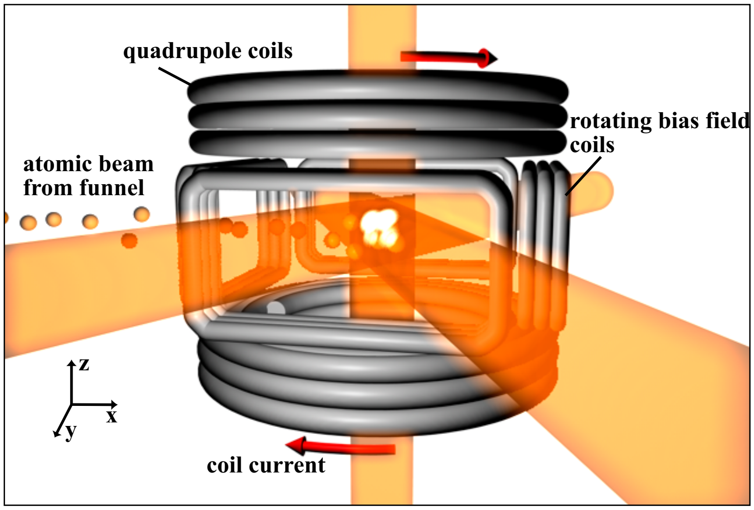

Figure 2.5: Schematic setup of the magneto-optical trap. The magnetic quadrupole field is realized by a pair of coils in anti-Helmholtz configuration. The gradient of the magnetic quadrupole field in the center, and thus the atomic density in the MOT is reduced by two pairs of coils in Helmholtz configuration, which provide a rotating bias field. Three pairs of counterpropagating laser beams are overlapped in the center. The horizontal pair encloses only an angle of 50° for geometrical reasons.

the average kinetic energy, this leads to a very efficient cooling of the atomic gas. This cooling method works best at high atomic densities, as the high energy tail is continuously repopulated by inter-atomic collisions. Bose-Einstein condensation is achieved by the so called *runaway evaporation*, where the decrease in density by the evaporation of atoms is overcompensated by the increase in density, when the atoms with low kinetic energy accumulate in the center of the trap.

TOP trap

In our experiment the precooled atoms are transferred from the MOT into a conservative magnetic trap. Magnetic trapping of atoms relies on the interaction of the atomic magnetic moment with an inhomogeneous magnetic field. An atom in the hyperfine state F with magnetic quantum number m_F is subjected to a potential

$$V(\vec{r}) = g_F \mu_B m_F B(\vec{r}) \tag{2.19}$$

due to the Zeeman energy shift. Here g_F is the Landé g-Factor, μ_B is the Bohr magneton and $B(\vec{r})$ is the magnetic field. Atoms with $g_F \mu_B m_F > 0$ (weak field seeker) can thus be trapped in a local minimum of a magnetic field. In regions of very small or vanishing magnetic fields the magnetic moment of moving atoms cannot follow adiabatically the direction of the magnetic field and thus trap loss due to spin flips into untrapped states is possible. These spin flips are referred to as *Majorana flops* (Majorana, 1932).

In our experiment we trap the atoms in the state $|F = 2, m_F = 2\rangle$ ($g_F = 1/2$) in a time-averaged orbiting potential (TOP) trap (Petrich *et al.*, 1995). It is realized by the sum of a spherical quadrupole field and an additional rotating bias field. These magnetic fields are generated by the coils used for the MOT (see figure 2.5). The top- and bottom-coils, driven in anti-Helmholtz configuration, produce a spherical quadrupole field. The two pairs of bias field coils, which generate the rotating homogeneous bias field, are driven with a sinusoidal current $I(t) = I_0 \sin(\omega_{\text{rot}} t + \varphi)$ in Helmholtz configuration, with a mutual phase difference of $\varphi = 90°$. The rotation frequency ω_{rot} is much larger than the oscillation frequency of the atoms and thus, together with the quadrupole field, a time-averaged harmonic potential

$$U_{\text{TOP}}(\vec{r}) = \mu_B B_0 + \frac{\mu_B B_r^2}{4B_0}\left(r^2 + 8z^2\right), \tag{2.20}$$

is generated, where B_0 is the amplitude of the bias field and B_r is the gradient of the quadrupole field in radial direction. The rotating field moves the zero of the magnetic field around in a circle ("‘the circle of death") of radius $r_D = B_0/B_r$ (see figure 2.6). Due to Majorana flops, this defines the depth of the potential to $U_{\text{TOP}}(r_D) = \mu_B B_0/4$ and is used in the experiment to implement evaporative cooling.

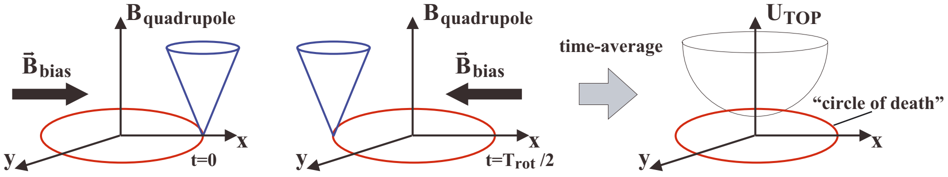

Figure 2.6: Schematic of the TOP trap. By adding a rotating homogeneous bias field to a spherical quadrupole field, a time-averaged harmonic potential with a non-vanishing local minimum is generated. The adjustable circle of death (rotating zero of the magnetic field) allows to vary the depth of the trap and thus evaporative cooling is intrinsically implemented into this trap.

2.2.4 Optical dipole trap

The aim of this work is the investigation of the dynamics of atomic wave packets in one dimension. Therefore an atomic waveguide is used in the experiment, which confines the atoms in the transversal direction and allows the free propagation in the axial or longitudinal direction. The waveguide potential is realized with a focused laser beam, utilizing the reactive light force.

The preparation of the atomic wave packets inside the waveguide is done in the following way. An ultra-cold sample of atoms is transferred from the TOP trap into a 3D optical trap, which consists of the waveguide and an additional crossed laser beam. In this optical trap, the atomic sample is Bose-condensed by evaporative cooling. In this way the generation of the initial wave packets inside the waveguide proved to be very precise and reproducible. The setup allows the preparation of wave packets with a longitudinal width of $5 - 20\mu$m rms and an atom number range from 1500 to 40000. The subsequent propagation along the waveguide is initiated simply by switching off the crossed laser beam.

In the following the optical waveguide potential and the evaporative cooling in the 3D optical trap are described.

Optical dipole potentials

The interaction of atoms with laser modes with a large detuning $\delta_l = \omega_l - \omega_0$ leads, as already pointed out in section 2.2.2, to a dipole (or reactive) force. The underlying process of redistribution of photons between different laser modes is coherent and thus the dipole force allows to implement conservative optical atom traps (Stamper-Kurn *et al.*, 1998). The interaction between the atoms and the light field is due to the coupling of the atomic dipole moment $\vec{d}$ and the electric field $\vec{E}(\vec{r})$ and is described by the Rabi frequency $\Omega_\mathrm{R}(\vec{r}) = \vec{d} \cdot \vec{E}(\vec{r})/\hbar$. For a two-level atom,

$$|\Omega_\mathrm{R}(\vec{r})|^2 = \frac{\Gamma^2 I(\vec{r})}{2I_s}. \tag{2.21}$$

where Γ is the width of the excited state, $I(\vec{r})$ is the local intensity of the light field and $I_s = \hbar\Gamma\omega_0^3/(12\pi c^2)$ is the saturation intensity. The dipole force acts in light fields with spatially varying intensity $I(\vec{r})$ and generates a dipole potential

$$V_\mathrm{dip}(\vec{r}) = \frac{\hbar\Gamma^2 I(\vec{r})}{8I_s}\frac{1}{\delta_l}, \tag{2.22}$$

where a large detuning $|\delta_l| \gg \Omega_\mathrm{R}, \Gamma$ is assumed. Depending on the detuning of the laser light, the potential changes its character. For red detuning the potential minima lie in the regions of maximum field intensity. For blue detuning the atoms are expelled from the regions of high intensity.

Multi-level atoms

In our experiment ^{87}Rb atoms are trapped in the $|F=2, m_F=2\rangle$ state in an optical dipole trap of laser light wavelength 1064 nm (Nd:Yag), with a superimposed optical lattice potential of wavelength 783 nm (Ti:Saphire). In both cases transitions to the states $|F=2, m_F=2\rangle$ (D_1-line), $|F=2, m_F=2\rangle$ and $|F=3, m_F=2\rangle$ (D_2-line) are involved. The resulting optical dipole potential is the sum of the three transitions (Metcalf/Straten, 1999)

$$V_\mathrm{dip}(\vec{r}) = \frac{\hbar\Gamma^2 I(\vec{r})}{8I_s} \cdot \left(\frac{2}{3\delta_2} + \frac{1}{3\delta_1}\right), \tag{2.23}$$

with the relative detuning δ_1 and δ_2 from the D_1-line and the D_2-line, respectively. The factors 2/3 and 1/3 stem from the fact that the strength of the involved transitions is 1/3 of the strongest transition, for which the saturation intensity $I_s = 1.6$ mW/cm^2 is given.

Focused laser beam waveguide and 3D trap

The waveguide for the matter waves is created by a focused linear polarized Gaussian laser light beam with the intensity profile

$$I(\vec{r}) = \frac{I_\mathrm{max}}{1 + (x/x_\mathrm{r})^2} \exp\left(-2\frac{y^2+z^2}{w(x)^2}\right). \tag{2.24}$$

Here $w(x) = w_l\sqrt{1+(x/x_{\mathrm{R}})^2}$ is the beam waist with $w_l \approx 40\mu$m and $x_{\mathrm{R}} = \frac{k_l}{2}w_l^2$ is the Rayleigh length with the norm of the wave vector $k_l = 2\pi/\lambda$. Such a Gaussian beam creates a cylindrically symmetric dipole potential with a weak axial confinement and a strong radial confinement. In the center, the trapping potential can be approximated by

$$V_D(\vec{r}) = V_{min} + \frac{1}{2}m\omega_\parallel^2 x^2 + \frac{1}{2}m\omega_\perp^2(y^2+z^2), \tag{2.25}$$

with the frequencies $\omega_\perp = \sqrt{\frac{4|V_{min}|}{m w_l^2}}$ and $\omega_\parallel = \frac{\sqrt{2}}{k_l w_l}\omega_\perp$, where $V_{min} = \frac{\hbar\Gamma^2 I_{\max}}{8I_s}\cdot\left(\frac{2}{3\delta_2}+\frac{1}{3\delta_1}\right)$ (see eq. 2.23). Typical values of V_{min} used in the experiment lead to transversal frequencies of $\omega_\perp \approx 2\pi\cdot 200$ Hz and corresponding longitudinal frequencies of $\omega_\parallel \approx 2\pi\cdot 1$ Hz. For the time scale of the experiment (100 ms max.) the trapping potential in the longitudinal direction is negligible and thus a quasi free propagation in longitudinal direction can be observed. The maximal spontaneous emission rate of photons

$$\Gamma_{\mathrm{sp}} = \frac{\hbar\Gamma^3 I_{\max}}{8I_s}\cdot\left(\frac{2}{3\delta_2^2}+\frac{1}{3\delta_1^2}\right) \lessapprox 0.5\,\mathrm{Hz} \tag{2.26}$$

is also negligible for the time scale of the experiments. In figure 2.7a the gaussian laser beam focus for this situation together with the cross section of the corresponding waveguide potential is depicted.

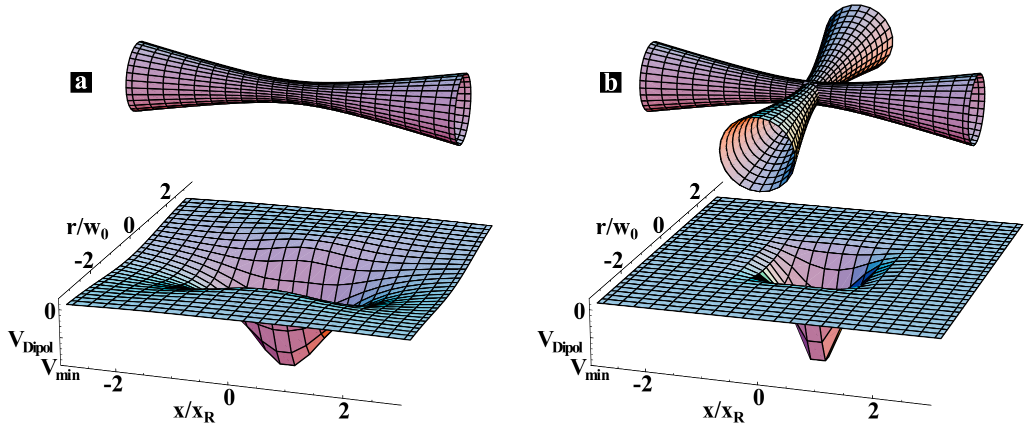

Figure 2.7: (a) A waveguide with tight radial and very shallow axial trapping potential is implemented with a red detuned laser beam focus. (b) A tight 3D trap is realized with two crossed laser beam foci. By varying the light intensity and thus the trap depth, Bose-Einstein condensates are generated by evaporative cooling.

Using two crossed laser beam foci (see figure 2.7b) a tight 3D optical dipole trap can be realized. In the experiment the waveguide, described above, and a crossed focused light beam of the same wavelength and a similar beam waist is used. Such a trap possesses a finite trap depth $U_{\max} \propto I_{\max}$ due to the finite width of the laser beams and the gravitational force. For small light intensities the gravitational force lowers the trap center ("gravitational sag" $\Delta z = g/\omega_z^2$) and the trap depth considerably (see figure 2.8). The dependence of the trap depth on the light intensity is used in the experiment to implement evaporative cooling and thus to generate Bose-Einstein condensates. In our setup, the power in each laser beam is controlled by acousto optical modulators (AOM). In addition the beam power is stabilized with an electronic feedback loop. This proved to be essential for a stable evaporation process. The polarization of the beams is chosen to be perpendicular, in order to avoid interference structures. As it is very difficult to realize a perfect polarization, the AOM's are run with different driving frequencies, so that the residual interference structures cycle on a time scale much faster than the trapping frequencies and are thus averaged to zero.

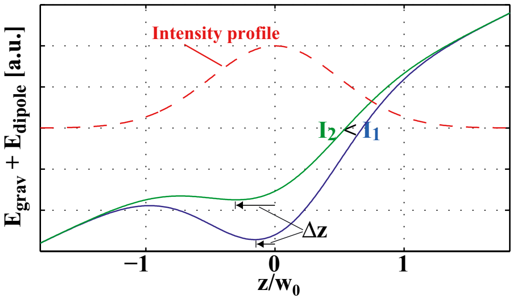

Figure 2.8: Potential energy resulting from the dipole force of a red detuned laser beam with Gaussian intensity profile and the gravitational force. Going from high light intensities (blue line) to low intensities (green line), the center of the corresponding potential is shifted by Δz (gravitational sag) and the depth of the potential is reduced.

2.2.5 Absorption imaging

The dynamics of the atomic wave packets is detected by absorption imaging, where the atomic cloud is illuminated by a resonant laser beam. The atoms absorb photons and cast a shadow on the light beam. Information on the size of the cloud is obtained by imaging the illuminated atomic sample with a single lens onto a CCD camera (see figure 2.9 a). In our experiment the imaging is realized using a single lens with high numerical aperture[2] and focal length 8 cm. The object is magnified by a factor of ∼10 and is recorded on a CCD chip[3] with a single pixel size of $6.4 \times 6.4\,\mu\mathrm{m}^2$ and a total resolution of the setup of $2.8\,\mu$m. In a single experiment run the image $I(x,z)$ of the atomic wave packet is recorded. Thereby the BEC is destroyed due to heating by spontaneous emission. Subsequently the reference intensity $I_{ref}(x,z)$ is taken, with no atoms present. The resulting transmission $T(x,z) = I(x,z)/I_{ref}(x,z)$ and the optical density $OD = -\ln(T)$ serve as the source of information for all subsequent analysis of the wave packet, like the determination of the number of atoms, the size and density, etc. (see an example in figure 2.9b).

A single atom scatters photons from the σ^+-polarized imaging beam, resonant with the $|F=2, m_F=2\rangle$-$|F'=3, m_F=3\rangle$ transition, with a rate (Metcalf/Straten, 1999)

$$\Gamma_{\mathrm{sp}} = \frac{s(y)\Gamma/2}{1+s(y)+(2\delta/\Gamma)^2}, \tag{2.27}$$

---

[2] Zeiss Plan-Apochromat

[3] Theta System SIS s285

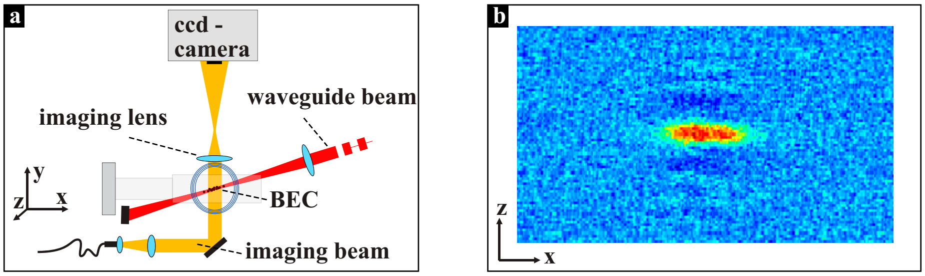

Figure 2.9: a) Absorption imaging setup. The atomic cloud is illuminated with a collimated laser beam. With a single lens a magnified image of the cloud is created and recorded with a CCD-camera. b) Image of the optical density of an elongated wave packet inside the waveguide. In the transversal direction the wave packet width is below the resolution limit and thus diffraction fringes are visible.

where $s(y) = I(y)/I_s$ is the saturation parameter. The light beam is attenuated due to the scattering of photons by

$$dI = -h\nu\,\Gamma_{\rm sp}\,\rho(x,y,z)\,dy, \tag{2.28}$$

where ρ is the density of the atomic cloud and ν is the frequency of the used optical transition. In order to investigate wave packets with a spatial modulation on a μm scale, a resonant light beam ($\delta = 0$) is used. For a detuning $\delta \neq 0$ the cloud gets a large refractive index, which leads to a disturbing lens like effect (see figure 2.10) and thus reduces the resolution. For a good signal-to-noise ratio, an optical density on the order of OD$\sim$1 is set in the experiment, with a saturation parameter $s_0 \equiv s(y=0) \gg 1$. In this case the scattering rate will remain almost constant and can be approximated by $\Gamma_{\rm sp} = s_0\frac{\Gamma}{2(1+s_0)}$. Eq. 2.28 can then be integrated directly to obtain the column density

$$n(x,y) = \int \rho dy = (T-1)\frac{(1+s_0)I_s}{h\nu\,\Gamma/2}, \tag{2.29}$$

from which, e.g. the number of atoms $N_{atoms} = \int n(x,z)\,dxdz$ can be calculated.

In the case of very small atom numbers (< 1000) an optical density of $OD \sim 1$ can only be obtained, when the saturation of the imaging beam is set to $s_0 \sim 1$, in which case the scattering rate is approximated as $\Gamma_{\rm sp} = \frac{s(y)\Gamma}{2(1+s_0)}$. Thus the intensity is attenuated exponentially and the resulting column density

$$n(x,y) = OD(x,z)\frac{(1+s_0)I_s}{h\nu\,\Gamma/2}, \tag{2.30}$$

depends on the optical density $OD(x,z)$.

Possible sources of errors in the optical analysis of the atomic wave packet are an insufficient optical resolution, a defocused system and a detuning $\delta \neq 0$. The effects of these sources of errors on the imaging are investigated numerically by means of Fourier optics. The Matlab© code of the numerical wave propagation is given in the appendix A.2. The results are shown and discussed in figure 2.10.

In the setup of the imaging beam, extreme care had been taken, to avoid all sources that generate fringes in the image $I(x, z)$, like dirt on the optical components or self-interference of the beam with reflections from surfaces. These fringes can easily move due to vibrations of the system between the recording of $I(x, z)$ and $I_{ref}(x, z)$ and thus distort the transmission $T(x, z)$. As fringes can never be completely avoided, the optical system is set up with a good passive mechanical stability.

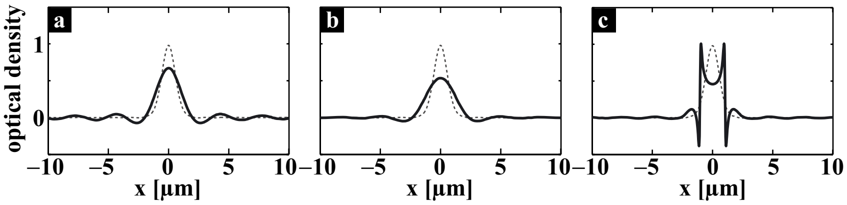

Figure 2.10: Numerical investigation of the distortions in the used imaging setup. a) the original gaussian wave packet profile (grey dotted line) has a width slightly smaller than the resolution limit of the system and thus the image profile (black line) features fringes at the sides which result from the diffraction at the finite size lens. b) in a defocused system the image is blurred and the width of the image profile increases. c) for a detuning $\delta \neq 0$ the large refractive index of the atomic cloud leads to lens like effects, which distort the image profile seriously.

2.2.6 Experiment control

The experimental apparatus is controlled via a computer featuring one digital IO-card "NI PCI-6534" from National Instruments, two 12 bit analog output-cards "NI PCI-6713" from National Instruments, a low-cost analog input card and a GPIB card. With a LabView program experiment sequences are written, where all the digital/analog output channel are programmed with a maximum time resolution of 1ms with a total length of several minutes. Additional "intelligent" devices, as e.g. an arbitrary waveform generator are programmed through the GPIB interface and triggered through a digital channel. The experiment sequences are saved onto the internal memory of the digital and analog output cards, which are time synchronized via an internal clock pulse connection. Therefore our system allows a real-time generation of the experiment sequences. In the appendix A.3 a flow diagram of the control software is given for the next generation.

2.2.7 Experimental sequence

The following steps are used to realize a ^{87}Rb Bose-Einstein condensate in the optical waveguide potential:

- Loading of the MOT via the funnel: both the funnel light and the MOT light are turned on. Within about 15 s the MOT is loaded with up to $2 \cdot 10^8$ ^{87}Rb atoms. The MOT is optimized for high atom numbers with a low density to reduce light induced losses. It is run with a detuning of $\delta = -1.4\,\Gamma$ and a magnetic gradient of 4 G/cm in radial direction. In addition the bias field coils of the TOP trap are run ($B_0 = 3\,$G) to further decrease the magnetic field gradient in the center of the MOT. At the end of the loading phase the funnel light is turned off.

- Compression of the MOT: In contrast to the optical cooling, which works best at low densities, evaporative cooling in the magnetic trap requires high densities. Therefore, at the end of the MOT phase, the sample of cold atoms is compressed by turning off the rotating bias field and by linearly increasing the magnetic field gradient up to $10\,\mathrm{G/cm}$ in $50\,\mathrm{ms}$. In addition the detuning is increased to $\delta = -5\,\Gamma$, which leads to a further compression and cooling of the MOT (Petrich *et al.*, 1994).

- Molasses cooling: The last optical cooling step is polarization gradient (or molasses) cooling (Dalibard *et al.*, 1989). The magnetic quadrupole field is turned off and the laser light detuning is increased to $\delta = -8\,\Gamma$. The molasses phase takes $7\,\mathrm{ms}$, during which the light intensity is ramped from 65% (larger cooling power) to 20 % (smaller final temperature) of the intensity used in the MOT phase. A residual magnetic field during the molasses phase leads to an acceleration of the atoms, as they are cooled into a "moving rest frame". Thus the earth's magnetic field and any stray magnetic fields are compensated by three pairs of compensation coils in Helmholtz configuration. The compensation is accomplished by minimizing the center of mass motion of the atomic cloud during the molasses phase. The efficiency of the subsequent transfer of the atoms into the magnetic trap depends very critically on the final center of mass velocity and temperature of the cloud. Therefore the final adjustment of the magnet field compensation and also the beam balance is done, optimizing the transfer of the atoms into the magnetic trap. Molasses cooling reduces the temperature of the atoms to $40 - 50\,\mu\mathrm{K}$.

- Optical pumping: Before the magnetic trap is turned on, the atoms are optically pumped to the $|F=2, m_F=2\rangle$ state. For this purpose a small rotating bias field $B_0 = 3\,\mathrm{G}$ is turned on, which defines the magnetic quantization axis. 4 pulses of the imaging light beam, synchronized with the rotating bias field, drive the σ^+-transition and thus leads to an accumulation of the atoms in the $|F=2, m_F=2\rangle$ state. The length of the pumping pulses is electronically controlled such that the total energy of the light pulse is constant. In this way fluctuations in the beam intensity are compensated, which increases the stability of the pumping process and leads to a more reproducible final atom number in the Bose-Einstein condensate.

- Transfer into the magnetic trap: After the optical pumping $\sim 10^8$ atoms are captured in the magnetic trap by simply ramping up the currents in the quadrupole and bias field coils of the TOP trap very quickly ($t \lesssim 1\,\mathrm{ms}$). In order not to loose phase space density, the magnetic trap must be "mode matched", or in other words, must be adjusted such that the atomic distribution after the molasses cooling is in thermal equilibrium in the magnetic trap. For a TOP trap with different trapping frequencies in the axial and radial direction, the "mode match" condition can only be met in one direction for the isotropic atomic density distribution after the molasses cooling. In the experiment a maximum phase space density is obtained with a magnetic field gradient of $B_r = 80\,\mathrm{G/cm}$ and a bias field of $B_0 = 23\,\mathrm{G}$ and a corresponding circle of death radius $r_D = 2.9\,\mathrm{mm}$.

- Adiabatic compression: In order to increase the efficiency of the evaporative cooling, the atomic sample is adiabatically compressed, by ramping up the trap frequencies to $\omega_r = 2\pi \cdot 30\,\mathrm{Hz}$ and $\omega_z = 2\pi \cdot 80\,\mathrm{Hz}$. This is accomplished by linearly increasing the magnetic field gradient to $B_r = 220\,\mathrm{G/cm}$ and the bias field to $B_0 = 45\,\mathrm{G}$ within 3 s.

- Circle-of-death evaporation cooling: The first precooling by evaporation is done in the TOP trap by circle-of-death cooling. Within 30 s the bias field is decreased linearly from $B_0 = 45\,\mathrm{G}$ to $B_0 \sim 4\,\mathrm{G}$, while the magnetic field gradient is kept constant. During this time the circle-of-death radius is decreased to $r_D = 200\,\mu\mathrm{m}$. At the end of the cooling $\sim 10^6$ atoms are left with a temperature of $\sim 5\,\mu\mathrm{K}$.

- Transfer into the optical dipole trap: With the TOP trap still on, both the waveguide beam intensity and the crossed focused laser beam intensity are ramped up within $\approx 900\,\mathrm{ms}$. The precise overlap of the center of the optical crossed dipole trap with the center of the atomic distribution in the TOP trap is very critical. The intensities of the laser beams are chosen such that all the atoms from the TOP trap can be held in the dipole trap. In our case these are $\approx 600\,\mathrm{mW}$ and $\approx 200\,\mathrm{mW}$ for the waveguide beam and the crossed laser beam, respectively. The intensities are held at these values for 300 ms, while the magnetic fields of the TOP trap are ramped down to zero. At the end of this phase a small homogeneous magnetic field (1 G) in the vertical direction is turned on, such that the spin polarization of the atoms is still preserved, even in the absence of the TOP trap.

- Condensation in the dipole trap: The final evaporative cooling to obtain a condensate is done in the dipole trap. In this way pure condensates can be realized directly in the waveguide. The intensities of the beams is reduces linearly in about 5 s. In this way the trap depth is reduced and the forced evaporation of the atoms leads to the condensation of the remaining atoms. The success of the condensation process is probed by looking at the absorption image after a time-of-flight (TOF) of 7 ms. The final values of the laser beam intensities are adjusted such ($100 - 200\,\mathrm{mW}$ below the initial value) that the TOF image shows the expected asymmetric expansion of the bose-condensed cloud, without the halo of the fast expanding thermal atoms.

- Preparation of the initial experiment wave packet: By varying the final beam intensity, the number of atoms of the condensates can be set. In our experiment pure condensate with 10^3 to 10^5 atoms can be realized. After the condensate with the desired atom number is generated, the intensities of the waveguide and the crossed laser beam are adiabatically changed to the final values within 1 s. The waveguide intensity defines the transversal frequency of the waveguide and the crossed laser beam intensity allows to determine the initial longitudinal width of the wave packet. The experimental investigation of the wave packet dynamics is started by abruptly switching off the crossed laser beam.

3 Nonlinear matter wave dynamics in shallow 1D lattice potentials

When mentioning lattice potentials, most physicists think of the periodically arranged atoms that form crystals, i.e. condensed matter physics. The corresponding dynamics of the crystal electrons is very complex, since the crystal dispersion relation can differ greatly from that of free electrons, featuring a band structure, band gaps, normal and anomalous dispersion, etc. With the additional strong electron-electron interaction the dynamics is rendered even more complex.

With the availability of coherent matter wave sources and the possibility to realize periodic potentials with the help of laser light interference structures, it is now possible to build tailored model systems to investigate nonlinear particle dynamics in periodic potentials. These atom optics model systems offer crucial advantages over atomic crystal systems, that led to the observation of theoretically predicted quantum effects, e.g. Bloch oscillations (Dahan *et al.*, 1996), the Quantum phase transition from a superfluid to a Mott insulator (Greiner *et al.*, 2002), etc. In the first place these atom optics systems offer the ability to tune the period and the depth of the periodic potential, even during evolution. In addition, the particle interaction can be tuned. An experimental advantage is the fact that the matter wave dynamics can be observed directly, without interference with the periodic potential – in contrast to the situation of electrons in atomic crystals.

In the experiments described in this chapter we investigated the dynamics of coherent atomic wave packets in a 1D waveguide with a superimposed 1D lattice potential. The lattice depth and period is chosen such that the resulting space and time scale of the wave dynamics is on the order of μm and ms, respectively. In this way we directly observed the effects of anomalous dispersion, negative effective mass and diverging effective mass. In addition we explored the possibility to tune the dispersion during the wave evolution. We demonstrated the technique of dispersion management for matter waves (Eiermann *et al.*, 2003; Anker *et al.*, 2003), a technique, originally developed in the field of nonlinear fiber optics, which allows to prevent the spreading of a wave packet. The corresponding experiments are described in section 3.3 and 3.4.

The intrinsic nonlinearity of our system, the atom-atom interaction, allows to prepare a very special wave packet dynamics: nonspreading localized wave packets, so called "bright solitons". They form if the nonlinear dynamics compensates the wave packet spreading due to linear dispersion. In our system the nonlinearity is governed by the atomic density and the linear dispersion can be adjusted by the wave packet width and the dispersion relation due to the periodic potential. In section 3.5 the experimental realization of bright atomic solitons is described. Our system is very similar to the nonlinear system of bright optical solitons, i.e. nonspreading laser light pulses in optical fibers.

Inspired by the optical system, a nonlinear equation for the wave packet envelope can be derived (Steel/Zhang, 1998). This equation does not contain the periodic potential explicitly. The effect of the lattice is included by using an effective mass in the kinetic term. This reduced equation allows a deeper understanding of the underlying soliton physics.

In the first part of this chapter the theoretical description of the linear lattice dynamics in terms of the Bloch function formalism is given. In addition the derivation of the dynamical envelope equation for the system is explained.

In the second part the relevant experimental setup, namely the realization of the optical lattice potential and the wave packet preparation are described.

In the last part of this chapter the corresponding experiments are presented. Since the demonstration of dispersion management and the realization of atomic gap solitons are described in detail in (Eiermann, PhD thesis 2004), only a summary and the publications are given. The experiments on continuous dispersion management and their numerical analysis are presented in more detail.

3.1 Theoretical description of the dynamics in 1D lattice potentials

In this section the theoretical basis for the understanding of the experiments is described. The linear wave dynamics in a 1D lattice potential is investigated in terms of the Bloch function description. In this context, the group velocity and the concept of the effective mass is defined and their influence on the dynamics is explained. In the second part the nonlinear dynamics is investigated by looking at the corresponding equation, which governs the dynamics of the wave packet envelope.

3.1.1 Bloch function description

The dynamics of particles in a shallow periodic potential $V(x)$ is most conveniently described with the Bloch function formalism, which is commonly used in solid state physics. In this section the energy spectrum, i.e. the dispersion relation for a single particle in a periodic potential is calculated. The dynamics of the particle is then discussed by looking at the properties of the dispersion relation, namely the group velocity and the effective mass.

The Bloch-Theorem (see e.g. Ashcroft/Mermin, 1976) states that the eigenfunctions $\Phi(x)$ of a single particle system with a periodic potential $U(x)$, described by the Schrödinger equation

$$\hat{H}\Phi(x) \equiv \left[-\frac{\hbar^2}{2m}\frac{\partial^2}{\partial x^2} + U(x)\right]\Phi(x) = E\Phi(x), \tag{3.1}$$

can be written as a product

$$\Phi_q^{(n)}(x) = e^{iqx}u_q^{(n)}(x) \tag{3.2}$$

of a plane wave and a function $u_q^{(n)}(x) = u_q^{(n)}(x+R)$ of the same periodicity R as the periodic potential $U(x)$. In our case a sinusoidal potential $U(x) = -V_0\cos^2(k_l x)$ is employed and therefore eq.(3.1) reduces to the Mathieu-equation.

The energy spectrum $E_n(q)$ shows a band structure with band index (n) and depends on the quasi-momentum q. It can be obtained numerically writing eq.(3.1) in matrix form. Since both $U(x)$ and $u_q^{(n)}$ are periodic functions, they can be expanded in a discrete Fourier series:

$$U(x) = \sum_m U_m e^{imQx} = -\frac{V_0}{4} e^{iQx} - \frac{V_0}{4} e^{-iQx} + const \quad \text{and} \quad u_q^{(n)} = \sum_m c_l^{(n)} e^{imQx}, \qquad (3.3)$$

where $Q = 2k_l$ is the reciprocal lattice vector and $m = 0, \pm1, \pm2, ...$ is an integer. This expansion is inserted into eq.(3.1). Multiplication with $e^{-iqx}e^{-imQx}$ from the left and subsequent integration allows to write the Schrödinger equation in matrix form

$$\sum_{m'} H_{m,m'} \cdot c_{m',q}^{(n)} = E_n(q) c_{m,q}^{(n)} \quad \text{with} \quad H_{m,m'} = \begin{cases} \frac{\hbar^2}{2m}(q - mQ)^2 & \text{if } m = m' \\ -1/4 \cdot V_0 & \text{if } |m - m'| = 1 \\ 0 & \text{else} \end{cases} \qquad (3.4)$$

The dispersion relation $E_n(q)$ and the eigen-states or Bloch-functions $\Phi_q^{(n)}(x)$ can now be obtained by numerically calculating the eigen-values $E_n(q)$ and the coefficients $c_l^{(n)}$ of the eigen-vectors of the truncated Hamiltonian matrix $H_{m,m'}$ (for $V_0 \lesssim 30\,E_\mathrm{r}$, $|m| = 15$ is sufficient). In appendix A.4 an example Matlab© code for the numerical calculation of $E_n(q)$ and $\Phi_q^{(n)}(x)$ is given.

The dispersion relation $E_n(q)$ is shown in figure 3.1 for various potential depth V_0. For vanishing potential depth, $E_n(q)$ shows the free particle vacuum dispersion relation. By increasing the potential depth, $E_n(q)$ splits into separated bands.

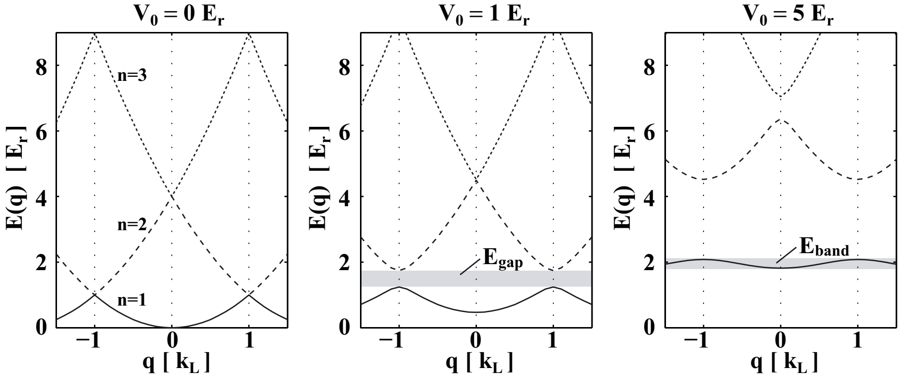

Figure 3.1: Band structure of a lattice potential: The energy of the Bloch state versus the quasi momentum q is shown for a potential depth of 0, 1 and 5 E_r. With increasing potential depth V_0 the inter-band gaps increase, while the band width decreases exponentially. In the experiments described in this thesis the dynamics of atomic wave packets, which only populate the first band n=1, is investigated.

In the following we will look more closely at the properties of the first Bloch band. Their understanding provides an intuitive picture of the dynamics of wave packets in a shallow lattice potential. The first thing to notice is that for a shallow potential ($V_0 \sim E_\mathrm{r}$) in the center of the first Brillouin zone ($|q| \ll k_l$) the dispersion relation does not differ much from that of a free particle (see figure 3.2a). Close to the Brillouin zone boundary (band edge) in contrast, due to the emergence of a band gap, the dynamics is expected to be very different from the free particle case. For more insight, the dispersion relation is written in a Taylor expansion

$$E(q) = E(q_0) + (q - q_0)\frac{\partial E(q)}{\partial q}\bigg|_{q_0} + \frac{1}{2}(q - q_0)^2\frac{\partial^2 E(q)}{\partial q^2}\bigg|_{q_0} + \ldots \tag{3.5}$$

around $q = q_0$. The first and the second order term are connected with the group velocity and the effective mass

$$v_g(q_0) = \frac{1}{\hbar}\frac{\partial E(q)}{\partial q}\bigg|_{q_0} \quad \text{and} \quad m_{eff}(q_0) = \hbar^2\left(\frac{\partial^2 E(q)}{\partial q^2}\bigg|_{q_0}\right)^{-1}, \tag{3.6}$$

respectively. For the first Bloch band $v_g(q)$ and $m_{eff}(q)$ are plotted in figure 3.2b,c). Their influence on the dynamics can be seen by looking at a wave packet with a small width in quasi momentum space ($\Delta q \ll 2k_l$ as depicted in figure 3.2a) centered at $q = q_0$.

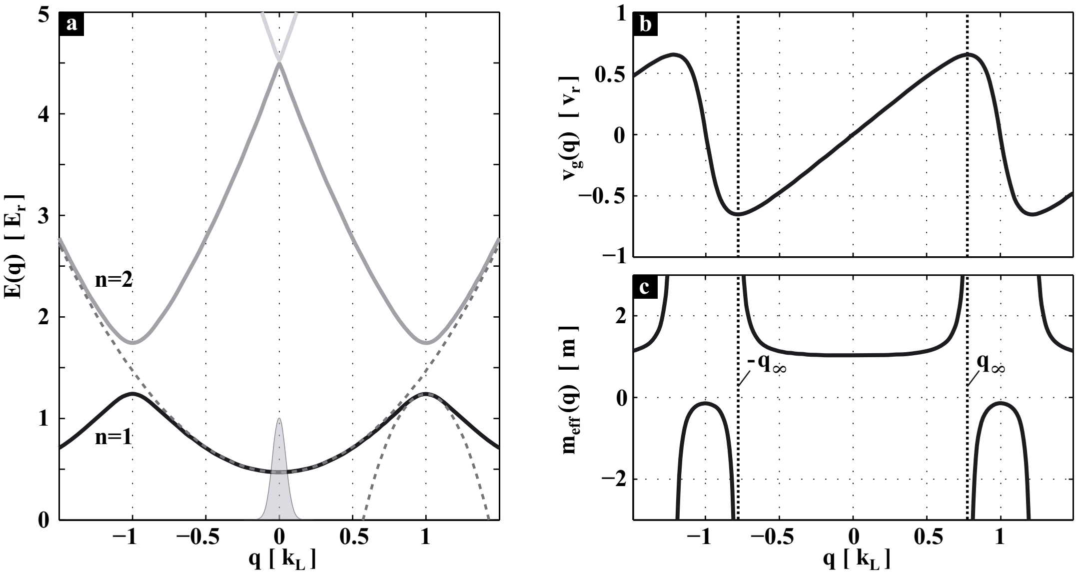

Figure 3.2: Properties of the first Bloch band. a) The energy of the Bloch state versus the quasi momentum q is shown for a potential depth of 1 E_r. In a large region around the center and in a small region around the edge of the Brillouin zone, $E_1(q)$ can be approximated by a parabolic dispersion relation (dashed curve). b) Group velocity $v_g(q)$ in units of the photon recoil velocity $v_r = \hbar k_l/m$. c) Effective mass $m_{eff}(q)$. The two regions with $m_{eff} > 0$ and $m_{eff} < 0$ correspond to the region with normal and anomalous dispersion, respectively. At the critical points $q = \pm q_\infty$ m_{eff} diverges and v_g is extremal.

The group velocity $v_g(q)$ gives the relative velocity of the wave packet with respect to the lattice potential. Thus, if a constant force is exerted onto the wave packet, which is initially prepared at $q = 0$, its central quasi momentum q_0 will be shifted and the relative velocity will increase, until it reaches a maximum at $q = q_\infty$. Subsequently the velocity will decrease again and will even change its direction and so on. This oscillatory behavior is called Bloch oscillation (Anderson *et al.*, 1998).

The role of the effective mass $m_{eff}(q)$ is twofold. It acts both on the center of mass movement as well as on the dispersion, i.e. the expansion (and also compression) of the wave packet. As can be seen in figure 3.2c), the Brillouin zone is split into two parts. In the center $m_{eff} \sim m > 0$, which corresponds to normal dispersion. Around the band edge, in contrast, $m_{eff} < 0$, which corresponds to anomalous dispersion. It is important to note that around the center and around the edge of the Brillouin zone, the dispersion relation $E(q)$ shows an approximately parabolic shape (see figure 3.2). Thus the dispersion is described by a constant effective mass in these region, as is the case for the free particle dispersion. In a lattice potential, in addition, the strength of the dispersion, i.e. the modulus of the effective mass $|m_{eff}(q_0, V_0)|$ can be tuned via the depth of the lattice potential V_0 !

The effective mass can also be understood in term of the reaction of the wave packet upon an external force: in the region of $m_{eff} < 0$ the wave packet accelerates in the opposite direction of the driving force, or "the wave packet runs up the hill" !

At the critical points $q = \pm q_\infty$, the effective mass $|m_{eff}| \to \infty$ diverges, and therefore the dispersion close to these points is strongly suppressed. This effect has a strong influence on the dynamics of a wave packet (see section 3.3).

In figure 3.3 the real part and the probability distribution in real space is shown for the Bloch function in the center and at the edge of the Brillouin zone. In the center the Bloch function has very small contribution from lattice momenta e^{imQx} in a shallow potential and is thus a constant function with a small modulation. At the band edge there are mainly two contributing momenta, namely $m = 0$ and $m = 1$, and therefore $\Phi^{(1)}_{q=k_l}(x) \approx e^{-ik_l x} + e^{ik_l x}$ is the sum of two counterpropagating plane waves.

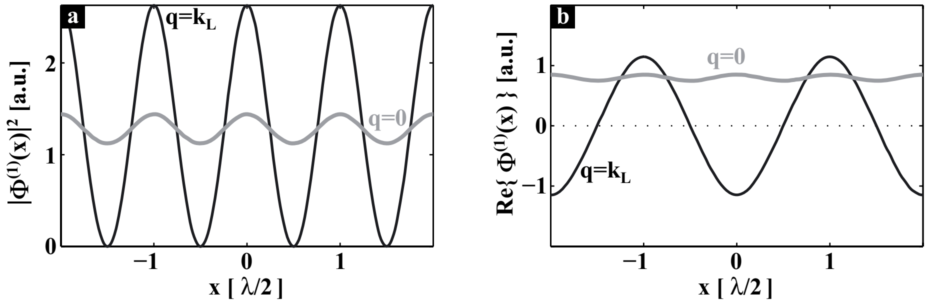

Figure 3.3: Probability density a) and real part b) of the Bloch function $\Phi^{(1)}_q(x)$ of the first band for $q = 0$ (gray line) and $q = k_l$ (black line) for a potential depth of $0.5\,E_\mathrm{r}$. In a shallow periodic potential $\Phi^{(1)}_{q=0}(x)$ can be described by the free particle wave function which is slightly modulated in density and phase. At the band edge, in contrast, $|\Phi^{(1)}_{q=k_l}(x)|^2$ is strongly modulated in density and vanishes at the potential maxima. The phase jumps by $\Delta\varphi = \pi$ from site to site (staggered mode).

3.1.2 Dispersive dynamics of matter wave packets

The dynamics of a wave packet is given by the temporal behavior of the center of mass and by the temporal behavior of the shape. In the experiments described in this chapter mainly the dynamics of the shape is investigated. When looking at the free expansion of an atomic wave packet in a shallow lattice potential, the shape dynamics is mainly governed by the free particle dispersion, the modification of the free particle dispersion relation by the lattice potential and by the nonlinear atom-atom interaction. In the first part of this section we will review the free particle dispersion, which is governed by the initial size of the wave packet, or in other words, by the Heisenberg Uncertainty relation. In the second part of this section a dynamical nonlinear equation, based on the Gross-Pitaevskii equation, is described, where the effect of the lattice potential is included in the kinetic energy term by means of a momentum dependent effective mass. In this way the influence of the lattice potential onto the dispersion is conveniently described by an effective mass concept in the context of the Bloch function description.

Free particle dispersion of matter wave packets

Dispersion is a wave phenomenon and leads to the expansion of, e.g. light wave packets (pulses) in a medium, where, in contrast to the vacuum, the group velocity $v_G(k) = \partial E(k)/\hbar\partial k$ depends on the k-vector. In Quantum mechanics, particles obey the Schrödinger wave equation, where even in the vacuum the group velocity $v_G(k) = \hbar k/m$, with the dispersion relation $E(k) = \hbar^2 k^2/2m$, has a linear dependence on the k-vector. A wave packet is generally generated by interference of many plane waves with different k-vectors. In a very simple picture one could think of the different plane waves as of atoms, that travel with different velocities - a process that then leads to an expansion of the wave packet. Being more quantitative and consistent, it is necessary to consider the phase evolution of the plane waves. The time evolution of a Gaussian wave packet $\Psi(x) = \exp(-x^2/\sigma_0^2)$, a standard example, which can be found in every quantum mechanics textbook, is given by

$$|\Psi(x,t)|^2 \propto \exp\left(\frac{2x^2}{\sigma(t)^2}\right), \tag{3.7}$$

where $\sigma(t) = \sigma_0\sqrt{1 + 4t^2/T_d^2}$. The dispersion time $T_d = m\sigma_0^2/\hbar$ depends on the initial size of the wave packet and reflects directly the Heisenberg uncertainty relation. The above result is obtained by considering that in k-space the time evolution of a free particle wave packet is given by $\tilde{\Psi}(k,t) = \tilde{\Psi}(k,0)\exp(-iE(k)t/\hbar)$, which is a quadratic phase evolution, determined by the free particle dispersion relation $E(k) = \hbar^2 k^2/2m$.

Nonlinear dynamical envelope equation

The influence of the lattice potential on the wave packet dynamics in general is very complex. In the limit, where only wave packets in the ground state, i.e. the first band of the lattice are considered, the influence can be described by a modified dispersion relation $E(q)$ (see section 3.1.1). The free evolution of a wave packet in the first Bloch band is given by

$$\Psi(x,t) = \int_{-k_l}^{k_l} f(q,t)\Phi_q(x)\, e^{-\frac{i}{\hbar}E(q)t}\, dq, \tag{3.8}$$

where $\Psi(x,0)$ is expanded in terms of Bloch functions $\Phi_q(x)$ with the expansion coefficients $f(q,t)$. The description of the dynamics can be further simplified for wave packets with a small width $\Delta q \ll |k_l|$ in q-space, i.e. $f(q) \neq 0$ for a small region Δq around a central quasi-momentum q_0. Considering the uncertainty relation, this is true for wave packets that are extended over many lattice periods in real space. In this limit the wave packet can be approximated by

$$\Psi(x,t) = A(x,t)\Phi_{q_0}(x)\, e^{-\frac{i}{\hbar}E(q_0)t}. \tag{3.9}$$

Here the Bloch functions $\Phi_q(x)$, which vary little on a scale of Δq, are replaced by the central Bloch function $\Phi_{q_0}(x)$. The wave packet shape is given by the envelope function $A(x,t)$, which varies only slowly on the scale of the lattice potential. With the ansatz 3.9 in the GPE (2.7) the dynamical nonlinear equation

$$i\hbar\frac{\partial}{\partial t}A(x,t) = \left[-\frac{\hbar^2}{2m_{eff}(q_0)}\frac{\partial^2}{\partial x^2} + \alpha_{\mathrm{nl}}(q_0,V_0)NG(|A(x,t)|^2)\right]A(x,t) \tag{3.10}$$

can be obtained. The derivation relies on the effective mass formalism and can be found in (Steel/Zhang, 1998) and (Pu *et al.*, 2003). The equation is given in the center of mass frame of the wave packet, which moves with the group velocity $v_g(q_0)$ of the central quasi momentum with respect to the lattice potential. The dynamical equation does not contain the lattice potential explicitly. The effect of the lattice potential is included in the linear dispersion relation $\tilde{E}(q,q_0)$, which is the Taylor expansion of the complete dispersion relation $E(q)$ up to second order (constant effective mass).

The above equation is only valid for small nonlinear energies, such that the atom-atom interaction does not couple states from the first band to the second. This means that the maximum mean-field energy $\alpha_{\mathrm{nl}}(q_0,V_0)NG(|A(x,t)|^2)$ must not exceed the energy width of the band gap at the edge of the Brillouin zone (see section 3.1.1). The nonlinearity factor

$$\alpha_{\mathrm{nl}}(q_0,V_0) = L\int_{-L/2}^{L/2}|u_{q_0}^{(1)}(x)|^4\,dx \tag{3.11}$$

accounts for the change of the nonlinear energy due to the lattice potential. In a lattice potential the atomic density is increased in the center of the potential wells and thus leads to an increased nonlinear energy. For shallow lattice potentials with a potential depth on the order of $V_0 \sim E_{\mathrm{r}}$, the nonlinearity factor increases, when going from the center to the Brillouin zone boundary with values on the order of $\alpha \sim 2$. In a pure 1D case, the nonlinearity function is given by $G(|A(x,t)|^2) = g_{1\mathrm{D}}N|\Psi(x,t)|^2$ (see eq. (2.10)). In an effective one dimensional situation the nonlinearity takes the form given in eq. (2.13).

Equation (3.10) describes a very rich physical system, where the phase evolution due to both the dispersion and the nonlinear interaction are under control. In the following sections experiments are described, which implement this system. The experimental results together with the results of the numerical analysis of eq. (3.10) show a synergy effect and lead to a deep intuitive understanding of the system.

3.2 Experimental realization and calibration of the lattice potential

In the experiments described in this chapter, the dynamics of wave packets inside a 1D waveguide with a superimposed shallow 1D lattice potential is investigated. In the first part of this section the experimental realization of the lattice potential and the preparation of the wave packets in quasi momentum space is described. In the second part, the calibration of the lattice potential depth is described. A novel "kick calibration" is implemented in this work, where a sinusoidal phase is imprinted onto the wave packet. The depth of the potential is then obtained by analyzing the resulting momentum distribution. In the last part of this section a numerical investigation of the effect of the nonlinear atomic interaction on the calibration process is presented.

3.2.1 Optical 1D lattice potentials

A very convenient way to realize periodic potentials is to use the optical potential resulting from the interference pattern of counterpropagating laser beams. They provide an exact sinusoidal periodicity, which can be adjusted by changing the laser wavelength or by changing the geometry of the system. The depth of the potential can be easily controlled by tuning the intensity of the laser beams and they can be superimposed on other potentials, like the waveguide potential in our experiment. In addition the velocity of the periodic potential can be controlled by introducing a small detuning between the two counter propagating beams.

In our experiment the simplest possible realization, a 1D optical lattice made of two counter propagating laser beams is used. The beams have a Rayleigh length $x_{\mathrm{R}} \gg 100\,\mu\mathrm{m}$ and a waist $w_D \gg 1\,\mu\mathrm{m}$ and therefore the variation of the intensity at the location of the atoms can be neglected. The interference of the two beams leads to the time-dependent intensity

$$I(x,t) = 4\sqrt{I_a I_b}\cos^2\left(k_l x - \frac{\Delta\omega}{2}t\right), \tag{3.12}$$

with the wave vector $k_l = 2\pi/\lambda$ and the difference in frequency between the two beams $\Delta\omega = \omega_b - \omega_a$. With eq. (2.23) the corresponding dipole potential becomes

$$V_D(x,t) = V_0\cos^2\left(k_l x - \frac{\Delta\omega}{2}t\right), \quad \text{with} \quad V_0 = \frac{\hbar\Gamma^2\sqrt{I_a I_b}}{2I_s}\cdot\left(\frac{2}{3\delta_2} + \frac{1}{3\delta_1}\right). \tag{3.13}$$

The depth of the potential is conveniently given in units of the recoil energy $V_0 = s \cdot E_{\mathrm{r}}$, where $E_{\mathrm{r}} = \hbar^2 k_l^2/2m$ is the change in kinetic energy due to the momentum transfer, when a photon of wave vector k_l is absorbed or emitted by an atom of mass m.

The velocity of the periodic potential in the laboratory frame is controlled through the frequency difference $\Delta\omega$. For $\Delta\omega \neq 0$ the lattice moves with a velocity $v = \Delta\omega/2k_l$.

3.2.2 Wave packet preparation in the lattice potential

The atomic wave packets are produced from Bose-Einstein condensates, which are realized inside a 3D optical dipole trap, as described in section 2.2. Subsequently the periodic lattice potential is ramped up adiabatically to prepare the wave packet in quasi momentum space (see figure 3.4b). The general adiabaticity criterium can be found in (Messiah, 1990). For shallow lattice potentials, neglecting the nonlinearity, the adiabaticity criterium demands a ramp up time $t_{\mathrm{ru}} \gg 1\mu\mathrm{s}$ for our system (Dahan *et al.*, 1996).

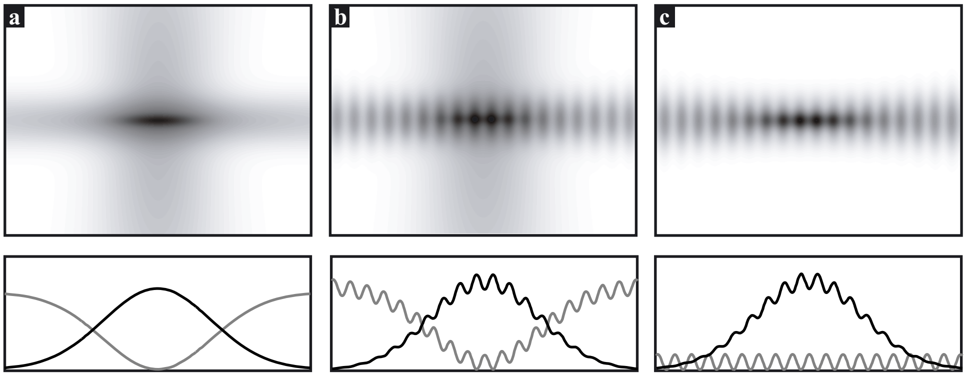

Figure 3.4: Schematic of the preparation of wave packets in a 1D waveguide with a superimposed periodic potential. a) a wave packet in a 3D optical trap of two crossed laser beams is created by Bose-Einstein condensation trough evaporative cooling. b) a periodic potential realized by the dipole force of a standing light wave along the waveguide is adiabatically ramped up. c) the crossed laser beam of the 3D dipole trap is turned off and the experiment sequence starts.

The periodic potential is generated from two counter propagating laser beams, which are collinear with the waveguide in the experiments on the dispersion management and the soliton formation (see section 3.3 and 3.5). In the experiment on continuous dispersion management (see section 3.4) the lattice beams enclose an angle of 21° with the waveguide. The laser beams are chosen to be slightly red detuned from the D_1-line. The light is obtained from a Ti:Sa laser and the intensity of the individual laser beams is controlled through acousto-optical modulators (AOM). The detuning between the two laser beams and thus the velocity of the periodic potential is controlled by adjusting the driving frequencies of the individual AOMs. The driving frequencies are generated by a two-channel arbitrary wave form generator (Tektronix AWG 420). In a single experiment run, where the main sampling frequency of the AWG is held fixed, the frequency difference can be changed in steps of $\Delta f \sim 100\,\mathrm{Hz}$, which in turn allows to adjust the velocity with a resolution of $\Delta v \sim v_\mathrm{r}/100$, where $v_\mathrm{r} = \hbar k_l/m = 5.9\mathrm{mm/s}$ is the recoil velocity. More technical details on the use of the AWG can be found in (Treutlein, Diploma Thesis, 2002).

Finally the crossed laser beam of the 3D dipole trap is turned off and the experiment sequence starts. Typical experiment sequences can be divided into preparation sequences and free propagation sequences.

During the preparation sequences the lattice potential is accelerated to a defined velocity, such that the wave packet is prepared to a defined central quasi momentum $\hbar q_\mathrm{c}$. The change of the quasi momentum by a force $F(t) = \hbar\partial q/\partial t$ is realized in this case by using the moment of inertia $\hbar\partial q/\partial t = ma(t)$. Experimentally the lattice potential is accelerated by changing the frequency difference between the two beams $\delta\nu$ in a linear ramp to prepare the wave packet at the quasi momentum $\hbar q_\mathrm{c} = m\delta\nu\lambda_{sw}/2$. This process needs to be adiabatic, in order not to populate higher bands. The adiabaticity criterium is most restrictive when preparing wave packets to the band edge, where the distance from the first to the second band is minimal (band gap). For very shallow lattice potentials on the order of $V_0 = 0.2 \cdot E_\mathrm{r}$, which are employed to generate solitons (see section 3.5), the minimum acceleration time can be on the order of $t_a \simeq 1$ms (Dahan *et al.*, 1996).

During the free propagation sequences the lattice potential moves with a constant velocity and the wave packet is allowed to propagate freely in the longitudinal direction of the waveguide (the longitudinal trapping potential of the waveguide can be neglected on the time scale of the experiments $t_{\mathrm{exp}} \ll 1/\nu_{\|}$).

3.2.3 Lattice potential calibration

The calibration of the optical periodic potential can be accomplished in many ways. In the first experiments in this work the depth of the periodic potential was calibrated by measuring the width of the band gap at the edge of the Brillouin zone (see section 3.1.1) by Landau-Zener tunneling (Jona-Lasinio *et al.*, 2003) and Bragg-oscillations (Kozuma *et al.*, 1999). Details of the implementation of these methods can be found in (Eiermann, PhD thesis 2004).

The calibration of the periodic potential by imprinting a sinusoidal phase or, in other words, by diffraction of the wave packet at a thin phase grating proved to be accurate, stable and very easy to implement. After a condensate is created in the 3D optical trap, the crossed laser beam is turned off. About 1 ms later the periodic potential is abruptly turned on for $T_p = 5\,\mu$s. Since the pulse length T_p is very short, the evolution of the atomic wave packet during the interaction is negligible and we are in the Raman-Nath regime of a thin grating (during the interaction the atoms move only a distance $s_m \ll \lambda/2$). The sinusoidal phase imprint

$$\exp\left(i\frac{V_0}{2}\sin(Qx)\right) = \sum_{n=0,\pm1,\pm2,\ldots} (-i)^n J_n(\phi_D)\exp(inQx) \tag{3.14}$$

leads to a diffraction with momenta $\hbar k_n = \hbar k_0 + n\hbar Q$, where k_0 is the initial momentum and $\hbar Q$ is the lattice momentum. The amplitude of the n^{th} diffraction order is given by $(-i)^n J_n(\phi_D)$, where J_n is the Bessel function of the first kind and $\phi_D = \frac{V_0 T_p}{2\hbar}$ is the depth of the phase modulation.

After the phase imprint, the condensate is released from the waveguide and after a time-of-flight of ~ 7 ms, when the diffraction orders are separated in space, the density profile is recorded on the camera (see figure 3.5) by absorption imaging. Summing up along the vertical axis, a density profile along the lattice direction is obtained and used as fit-data. The fit function was chosen to be a sum of 7 Gaussian distributions, where the main fitting variable was the depth of the phase modulation ϕ_D, which determines the height of the individual diffraction momenta (see eq. (3.14)). From the fit, the potential depth V_0 is obtained with an error of ~ 10 %.

Nonlinear effects on the calibration

The phase imprint adds additional momentum orders to the initial momentum distribution of the wave packet, which is determined only by the initial shape of the packet. After the release of the wave packet from the waveguide, the nonlinear interaction energy is converted into kinetic energy, which leads to a broadening in momentum space. For single Bose-condensed wave packets in the Thomas-Fermi regime, this leads, during time-of-flight, to a self-similar broadening in real space (Castin/Dum, 1996). In the

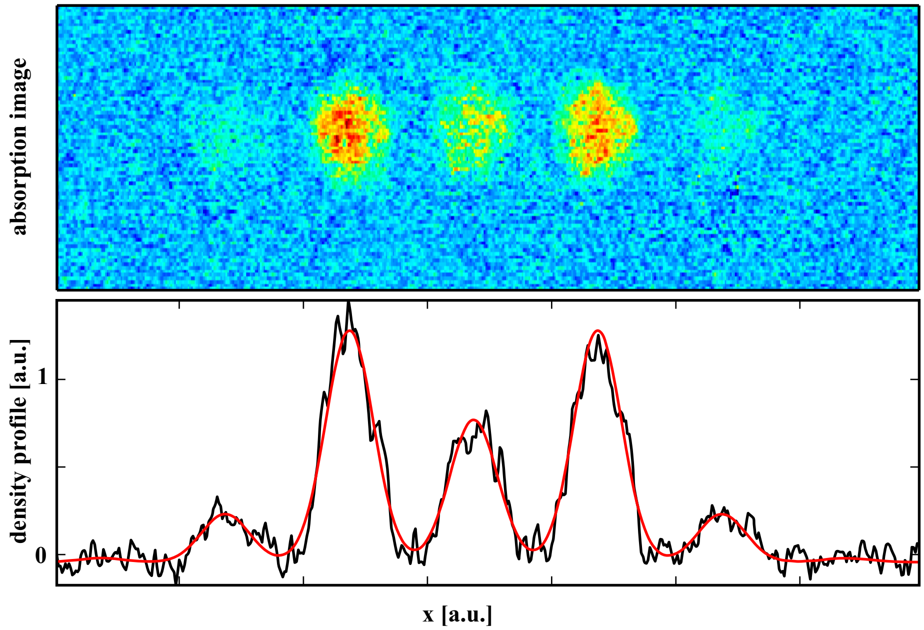

Figure 3.5: Calibration of the lattice potential. After a short sinusoidal phase imprint of 5 μs and a subsequent time-of-flight of $\approx$ 7ms the initial condensate wave packet separates into single wave packets, which correspond to the different momentum orders (top). The relative atom number in the individual wave packets, which corresponds to the strength of the different momentum orders, is obtained by integrating the absorption image transversally and fitting a sum of Gaussian distributions to the longitudinal density profile (bottom). The strength of the lattice potential is calculated from eq. (3.14).

calibration process in contrast, during the time, when the different momentum orders separate but are still partially overlapped in space, the nonlinear dynamics leads to a distortion of the wave packet shape (see figure 3.6).

To obtain an estimate of this nonlinear effect on the calibration process, the phase imprint and the subsequent time-of-flight was simulated numerically in 1D with the help of the non-polynomial nonlinear Schrödinger equation NPSE (see section 2.1.4). In figure 3.6 a calibration experiment and the corresponding simulation are compared. For both the experiment and the simulation a wave packet of $\sim$ 5000 atoms with an initial longitudinal width of 10 μm in a waveguide of 230 Hz transversal frequency is used. The phase imprint duration is 5 μs with a lattice potential depth $s = 29$.

After the phase imprint, the condensate is released from the waveguide and is allowed to expand freely. The asymmetric initial shape of the condensate with a longitudinal width of 10 μm and a transversal width of $\sim$ 1μm leads to an asymmetric expansion, where the interaction energy is mainly converted into transversal kinetic energy on a timescale of $1/(230\,\mathrm{Hz}) \approx$ 4ms. To model this 3 dimensional dynamics with the 1D NPSE, the following method is used. After the phase imprint, the NPSE is propagated for 0.5 ms, which corresponds to the time between the experimental phase imprint and the subsequent turn-off of the waveguide. In the following the reduction of the atomic density due to the transverse expansion is modeled by exponentially reducing the atom number in the simulation on a timescale of 2 ms.

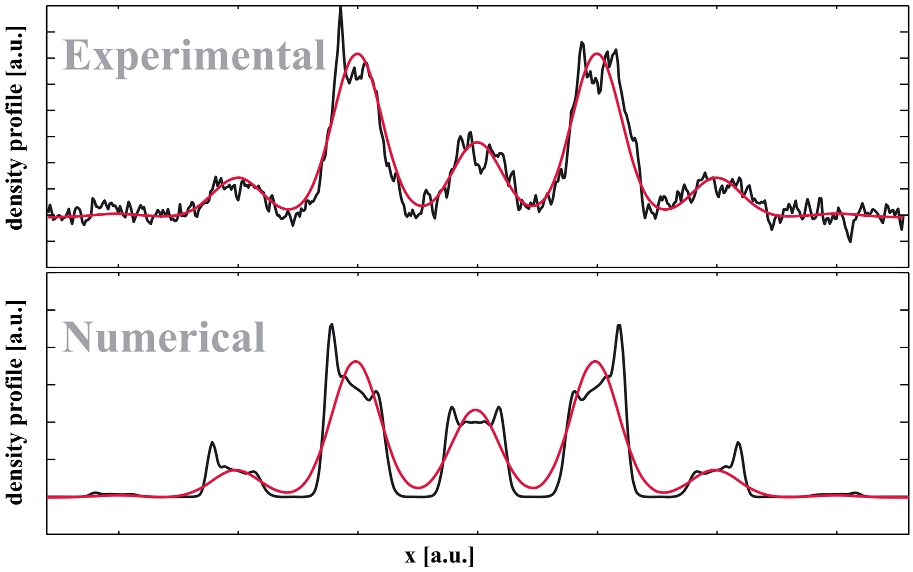

Figure 3.6: Numerical simulation of the calibration experiment. A numerical propagation of the NPSE allows to reproduce the distortion of the density profile (strong side peaks of the individual wave packets) due to the nonlinear interaction. Applying the same fit procedure to the simulated data shows that the error of the calibration procedure due to nonlinear interaction is on the order of 3% and can thus be neglected.

Figure 3.6 shows that the numerical simulation qualitatively reproduces the distortion of the density profile due to the nonlinear interaction. The experimentally observed strong side peaks of the individual wave packets can be explained by the change of the longitudinal momentum distribution due to the nonlinear interaction. Applying the same fit procedure to the simulation data yields a lattice strength, which differs only by $\approx 3\%$ from the value used in the simulation. Therefore this simulation shows that the influence of the nonlinear interaction onto the calibration process can be neglected.

3.3 Dispersion management

In the first series of experiments done in this thesis, the active modification of the dynamics of interacting matter waves in a 1D waveguide by applying a shallow lattice potential is investigated in terms of the concept of the effective mass. The experiments explore the new technical possibilities due to the following theoretical and experimental facts.

The dispersion relation $E(q)$ of a lattice potential shows regions with a positive, a negative and a diverging effective mass in the first Bloch band (see section 3.1.1). These regions correspond to a normal, an anomalous and a suppressed dispersion. In addition, both in the center and at the edge of the Brillouin zone, the dispersion relation can be approximated by a parabola, i.e. in a small region around these two points the effective mass is approximately constant.

Experimentally, our setup allows to prepare atomic wave packets in the first Bloch band with a very small width in quasi momentum space. The experimental control of the longitudinal velocity of the lattice potential allows to prepare the wave packets at arbitrary quasi momenta. The free evolution of the matter wave packet along the waveguide can be observed in real space for very long observation times.

3.3.1 Publication: Dispersion Management for Atomic Matter Waves

The above given prerequisites make it possible to realize "dispersion management" for matter waves, to study the "effective mass approximation" and to directly measure the maximum group velocity of the first Bloch band. These experiments are published in (Eiermann *et al.*, 2003) and are summarized in the following.

Dispersion management The first experiments investigate the active change of the dispersion from normal to anomalous dispersion during the evolution of the wave packet - a technique known as "dispersion management" in the field of nonlinear optics (Agrawal, 2001), where the broadening of light pulses in optical fibers is suppressed by spatially modulating the index of refraction. The experiments presented here show that this technique can also be implemented in the field of matter wave optics. In the presented experiments, the technique of dispersion management allows to reverse an initial expansion of a wave packet in the normal dispersion regime by subsequently placing it in the regime of anomalous dispersion, where it compresses until it regains its initial size.

Constant effective mass approximation The dispersion relation $E(q)$ in a lattice potential shows an approximately parabolic shape around the center and around the edge of the Brillouin zone. In these regions a wave packets experiences a quasi free particle dispersion, i.e. a quadratic phase evolution in q-space. In contrast to the free particle dispersion, here the nature and the strength of the dispersion can be tuned experimentally. In the experiment,e.g. a wave packet is prepared at the edge of the Brillouin zone, where it experiences an anomalous dispersion ($m_{eff} < 0$). Using a shallow potential, the dispersion is enhanced ($|m_{eff}| < 1$) compared to the free particle case - an important prerequisite for the generation of solitons (see section 3.5). In this experiment, the limits and the applicability of the constant effective mass approximation are explored.

Direct measurement of the maximum group velocity The experimental setup allows to observe the influence of the modified dispersion in real space. In the experiments presented below wave packets are prepared in the Brillouin zone such that they populate the particular regions around $q = q_{\pm\infty}$, where the effective mass diverges. As a result the dispersion around these regions is strongly suppressed and the atoms remain localized for a long time. This in turn allows to directly measure their relative velocity $v_g(q_{\pm\infty})$, which is the maximum group velocity in the first Bloch band.

Dispersion management for atomic matter waves

B. Eiermann[1], P. Treutlein[1,2], Th. Anker[1], M. Albiez[1], M. Taglieber[1], K.-P. Marzlin[1], and M.K. Oberthaler[1]
[1]*Fachbereich Physik, Universität Konstanz, Fach M696, 78457 Konstanz, Germany*
[2]*Max-Plank-Institut für Quantenoptik und Sektion Physik der*
Ludwig-Maximilians-Universität, Schellingstr.4, 80799 München, Germany
(Dated: March 17, 2003)

We demonstrate the control of the dispersion of matter wave packets utilizing periodic potentials. This is analogous to the technique of dispersion management known in photon optics. Matter wave packets are realized by Bose-Einstein condensates of ^{87}Rb in an optical dipole potential acting as a one-dimensional waveguide. A weak optical lattice is used to control the dispersion relation of the matter waves during the propagation of the wave packets. The dynamics are observed in position space and interpreted using the concept of effective mass. By switching from positive to negative effective mass, the dynamics can be reversed. The breakdown of the approximation of constant, as well as experimental signatures of an infinite effective mass are studied.

PACS numbers: 03.75.Be, 03.75.-b, 32.80.Pj, 03.75.Lm
Keywords:

The broadening of particle wave packets due to the free space dispersion is one of the most prominent quantum phenomena cited in almost every textbook of quantum mechanics. The realization of Bose-Einstein condensates of dilute gases allows for the direct observation of wave packet dynamics in real space on a macroscopic scale [1]. Using periodic potentials it becomes feasible to experimentally study to what extent the matter wave dispersion relation can be engineered. This approach is similar to dispersion management for light pulses in spatially periodic refractive index structures [2].

First experiments in this direction have already been undertaken in the context of Bloch oscillations of thermal atoms [3] and condensates [4]. The modification of the dipole mode oscillation frequency of a condensate due to the changed dispersion relation in the presence of a periodic potential has been studied in detail [5, 6]. In contrast to these experiments where the center of mass motion was studied, we are investigating the evolution of the spatial distribution of the atomic cloud in a quasi one-dimensional situation. For the wave packet dynamics many new effects are expected due to the interplay between nonlinearity resulting from atom-atom interaction and dispersion. In particular, non-spreading wave packets such as gap solitons [7] and self trapped states [8] are predicted. Our experiments show that even propagation in the linear regime with modified dispersion can change the shape of an initially Gaussian wave packet significantly.

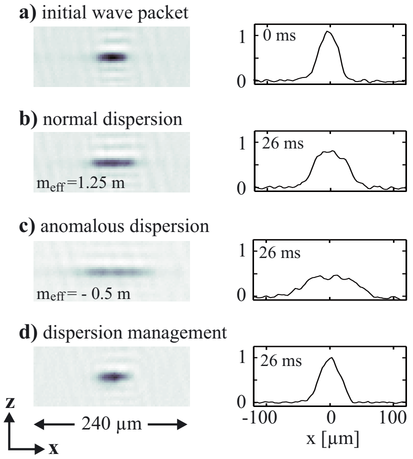

FIG. 1: Controlling the dispersion of an atomic wave packet in a waveguide using a periodic potential. Shown are absorption images of the wave packet averaged over four realizations (left) and the corresponding density distributions $n(x, t)$ along the waveguide (right). (a) Initial wave packet. (b,c) Images taken after an overall propagation time of $t = 26\,\mathrm{ms}$ for different dispersion regimes with different effective masses as indicated. (d) Wave packet subjected to dispersion management: an initial stage of expansion for $t = 17\,\mathrm{ms}$ with normal dispersion is followed by propagation with anomalous dispersion for $t = 9\,\mathrm{ms}$. The broadening in the normal dispersion regime has been reversed by anomalous dispersion.

For atomic matter waves inside a one-dimensional optical waveguide, we have achieved dispersion management by applying a weak periodic potential with adjustable velocity. Fig. 1 shows the results of an experiment in which the propagation of an atomic wave packet is studied in the normal (Fig. 1b) and anomalous (Fig. 1c) dispersion regime corresponding to positive and negative effective mass, respectively. A broadening of the wave packet is observed in both cases. The faster spreading in the case of anomalous dispersion is a consequence of the smaller absolute value of the negative effective mass. However, if we switch from one regime to the other during the propagation by changing the velocity of the periodic potential, the effects of normal and anomalous dispersion cancel. The wave packet, which has initially broadened under the influence of normal dispersion, reverses its expansion and compresses until it regains its initial shape (Fig. 1d). This is a direct proof of the realization of negative effective mass.

The concept of effective mass m_{eff} [9] allows to describe the dynamics of matter wave packets inside a periodic potential in a simple way via a modified dispersion relation. The periodic potential in our experiments is well described by

$$V(x) = \frac{V_0}{2}\cos(Gx)$$

with a modulation depth V_0 on the order of the grating recoil energy $E_G = \hbar^2 G^2/8m$, with $G = 2\pi/d$ where $d = 417\,\text{nm}$ represents the spatial period. The energy spectrum of atoms inside the periodic potential exhibits a band structure $E_n(q)$ which is a periodic function of quasimomentum q with periodicity G corresponding to the width of the first Brillouin zone (Fig. 2a). In our experiment, we prepare condensates in the lowest energy band ($n = 0$) with a quasimomentum distribution $w(q)$ centered at $q = q_c$ with an rms width $\Delta q \ll G$ [10].

It has been shown by Steel et al. [11] that in this case the condensate wave function in a quasi one-dimensional situation can be described by $\Psi(x,t) = A(x,t)\ \phi_{q_c}(x)\ exp(-iE_0(q_c)t/\hbar)$, where ϕ_{q_c} represents the Bloch function in the lowest energy band corresponding to the central quasimomentum. The evolution of the envelope function $A(x,t)$, normalized to the total number of atoms N_0, is described by

$$i\hbar\left(\frac{\partial}{\partial t} + v_g\frac{\partial}{\partial x}\right)A = -\frac{\hbar^2}{2m_{\text{eff}}}\frac{\partial^2}{\partial x^2}A + \tilde{g}|A|^2 A. \qquad (1)$$

The strength of the atom-atom interaction is given by $\tilde{g} = \alpha_{nl}2\hbar\omega_\perp a$, with the transverse trapping frequency of the waveguide $\omega_\perp$, the s-wave scattering length a, and a renormalization factor $\alpha_{nl} = 1/d\int_0^d dx|\phi_{q_c}|^4$. Besides the modification of the nonlinear term the periodic potential leads to a group velocity of the envelope $A(x,t)$ determined by the energy band via $v_g(q_c) = \hbar^{-1}(\partial E_0(q)/\partial q)|_{q_c}$ (Fig. 2b). In addition, the kinetic energy term describing the dispersion of the wave packet is modified by the effective mass (Fig. 2c)

$$m_{\text{eff}}(q_c) = \hbar^2\left(\left.\frac{\partial^2 E_0(q)}{\partial q^2}\right|_{q_c}\right)^{-1}.$$

It is important to note that group velocity and effective mass are assumed to be constant during the propagation. Since the approximation of constant effective mass corresponds to a parabolic approximation of the energy band, it is only valid for sufficiently small Δq as can be seen in Fig. 2.

The general solution of Eq. (1) is a difficult task, but simple analytic expressions can be found in the special cases of negligible and dominating atom-atom interaction. Omitting the last term in Eq. (1) it is straightforward to see that $|m_{\text{eff}}|$ controls the magnitude of the dispersion term and thus the timescale of the wave packet broadening. A change in sign of m_{eff} corresponds to time reversal of the dynamics in a frame moving with velocity v_g. In the regime where the atom-atom interaction is dominating, e.g. during the initial expansion of a condensate, the evolution of the envelope function can be found in standard nonlinear optics textbooks [12] and in form of scaling solutions in the context of Bose-Einstein condensates [13]. Note that in this regime the kinetic energy term is still relevant and thus a change of the sign of the effective mass will reverse the dynamics.

In the following we will analyze the obtained experimental results in more detail. The initial wave packet shown in Fig. 1a) is characterized by $\Delta x_0 = 14.8(6)\,\mu\text{m}$ (Δx is the r.m.s width of a Gaussian fit) and shows the density distribution of a Bose-Einstein condensate of $2\cdot 10^4$ atoms in a three-dimensional dipole trap. Before releasing the atomic cloud into the one dimensional waveguide, a weak periodic potential along the waveguide is adiabatically ramped up to $V_0 = 2.8(2)\,E_G$ within 6 ms. This turns the initial Gaussian momentum distribution of the atoms into a Gaussian distribution of quasimomenta $w(q)$ centered at $q_c = 0$ in the lowest energy band of the lattice with a corresponding effective mass $m_{\text{eff}} = 1.25\,m$. The density distribution shown in Fig. 1b) is a result of propagation within the stationary periodic potential for $t = 26\,\text{ms}$ and exhibits a spread of $\delta x := \sqrt{\Delta x(t)^2 - \Delta x_0^2} = 18.4(12)\mu\text{m}$ in contrast to $\delta x_f = 20.2(14)\,\mu\text{m}$ for expansion without periodic potential. The resulting ratio $\delta x_f/\delta x = 1.10(15)$ indicates that the evolution is dominated by the nonlinearity, in which case one expects $\delta x_f/\delta x \approx \sqrt{m_{\text{eff}}/m} = 1.11$ [14]. In the case of linear propagation one expects $\delta x_f/\delta x = m_{\text{eff}}/m = 1.25$.

The dynamics in the anomalous dispersion regime are investigated by initially accelerating the periodic potential within 3 ms to a velocity $v = v_G := \hbar G/2m$, thus preparing the atomic wave packet at the edge of the Brillouin zone, where $m_{\text{eff}} = -0.5\,m$. The velocity is kept constant during the subsequent expansion. In the regime of negative mass a condensate exhibits collapse dynamics similar to condensates with attractive atom-atom interaction. Two-dimensional calculations for our experimental situation reveal that this collapse happens within the initial 3-6 ms of propagation. This leads to a fast reduction of the density and therefore of the nonlinearity due to excitation of transverse states. An indication of the population of transverse states is the observed increase of the transverse spatial extension of the wave packets for anomalous dispersion by almost a factor of two. The optical resolution of our setup does not allow for a quantitative analysis of the transverse broadening. The measured spread of $\delta x = 38.5(15)\,\mu\text{m}$ after 23 ms of

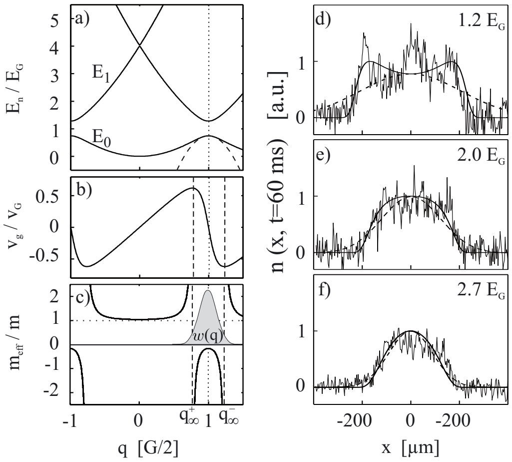

FIG. 2: (a) Band structure in the first Brillouin zone for atoms in an optical lattice with $V_0 = 1.2\,E_G$ (solid), parabolic approximation to the lowest energy band at $q = G/2$ (dashed), corresponding group velocity (b) and effective mass (c) in the lowest energy band. The vertical dashed lines at $q = q_\infty^\pm$ indicate where $|m_{\text{eff}}| = \infty$. (d-f) Spatial densities of the wave packet after $t = 60\,\text{ms}$ of propagation with $q_c = G/2$ for different V_0. The position x along the waveguide is measured in the moving frame of the optical lattice. The solid lines represent the theoretical predictions using linear propagation with the exact band structure and the quasimomentum distribution given in graph (c). The dashed lines in Graph (d-f) represent the prediction of the constant effective mass approximation.

expansion leads to a ratio $\delta x_f/\delta x = 0.46(5)$. This ratio represents an upper limit due to the initial collapse, indicating that a coherent nonlinear evolution in one dimension cannot describe the experimental results.

In the case of dispersion management Fig. 1d) the wave packet was first subjected to normal dispersion for 17 ms at $q_c = 0$. The time of subsequent propagation with anomalous dispersion at $q_c = G/2$ was adjusted to achieve the minimal wave packet size of $\Delta x = 15.4(2)\,\mu$m. The minimum was achieved for times ranging from 7 ms to 9 ms which is in rough agreement with the expected time resulting from effective mass considerations $\sqrt{0.5/1.25} \times 17\,\text{ms} = 10.7\,\text{ms}$. The experimental results exhibit a rapid increase of the wave packet width for overall propagation times longer than 27 ms also indicating collapse dynamics.

Before presenting the detailed experimental studies of the applicability of the constant effective mass approximation and evidence of infinite masses, we turn to a brief description of our setup.

The wave packets have been realized with a ^{87}Rb Bose-Einstein condensate. The atoms are collected in a magneto-optical trap and subsequently loaded into a magnetic time-orbiting potential trap. By evaporative cooling we produce a cold atomic cloud which is then transferred into an optical dipole trap realized by two focused Nd:YAG laser beams with $60\,\mu$m waist crossing at the center of the magnetic trap. Further evaporative cooling is achieved by lowering the optical potential leading to pure Bose-Einstein condensates with up to $3 \cdot 10^4$ atoms in the $|F = 2, m_F = +2\rangle$ state. By switching off one dipole trap beam the atomic matter wave is released into a trap acting as a one-dimensional waveguide with radial trapping frequency $\omega_\perp = 2\pi \cdot 80\,\text{Hz}$ and longitudinal trapping frequency $\omega_\parallel = 2\pi \cdot 1.5\,\text{Hz}$.

The periodic potential is realized by a far off-resonant standing light wave with a single beam peak intensity of up to $5\,\text{W/cm}^2$. The chosen detuning of 2 nm to the blue off the D2 line leads to a spontaneous emission rate below 1 Hz. The frequency and phase of the individual laser beams are controlled by acousto-optic modulators driven by a two channel arbitrary waveform generator allowing for full control of the velocity and amplitude of the periodic potential. The light intensity and thus the absolute value of the potential depth was calibrated independently by analyzing results on Bragg scattering [15] and Landau Zener tunneling [4].

The wave packet evolution inside the combined potential of the waveguide and the lattice is studied by taking absorption images of the atomic density distribution after a variable time delay. The density profiles along the waveguide, $n(x,t)$, are obtained by integrating the absorption images over the transverse dimension z.

Since the assumption of a constant effective mass used so far is only an approximation, it is important to check its applicability in experiments. Therefore we investigate the dynamics of wave packets prepared at the Brillouin zone edge ($q_c = G/2$) for different potential depths. The observed density profiles after 60 ms of propagation are shown in Fig. 2d-f). While both the initial wave packet shape $n(x,0)$ and the quasimomentum distribution $w(q)$ are measured to be approximately Gaussian, the wave packet changes its shape during evolution. We attribute this distortion to the invalidity of the constant effective mass approximation, which assumes that the populated quasimomenta experience the same negative curvature of $E_0(q)$. Since the range of quasimomenta fulfilling this criterion becomes smaller with decreasing modulation depth, a more pronounced distortion of the wave packet shape for weak potentials is expected (see Fig. 2d).

This explanation is confirmed more quantitatively by comparing the observed wave packets with the results of an integration of Eq. (1) neglecting the nonlinear term. Since the initial collapse of the condensate cannot be described by a linear theory, we take a Gaussian function fitted to the density distribution measured at 20 ms as the initial wave packet for the numerical propagation. Due to the fact that this is not a minimum uncertainty wave packet we add a quadratic phase in real space such that the Fourier transform of the wave packet is consistent with the measured momentum distribution. In first approximation this takes into account the initial expansion including the repulsive atom-atom interaction. For the subsequent propagation of 40 ms we use the full expression for $E_0(q)$ which is obtained numerically. Finally we convolute the obtained density distribution with the optical resolution of our setup. In Fig. 2d-f) we compare the data with the linear theory described above (solid line) and with the constant effective mass approximation (dashed line). Clearly the effective mass approximation cannot explain the observed distortion and it strongly overestimates the expansion velocity for weak potentials. Additionally, for small potential modulation depths new features appear in the central part of the wave packet which cannot be explained using the linear theory. We are currently investigating these features in more detail.

The observed distortion is mainly a consequence of another very interesting feature of the band structure: the existence of $|m_{\text{eff}}| = \infty$ for certain quasimomenta $q = q_\infty^\pm$ (see Fig. 2c). A diverging mass implies that the group velocity is extremal and the dispersion vanishes as can be seen from Eq. (1). As a consequence an atomic ensemble whose quasimomentum distribution is overlapping $q = q_\infty^\pm$ will develop steep edges as can be seen in Fig. 2d). These edges propagate with the maximum group velocity of the lowest band.

The systematic investigation of the velocities of the edges is shown in Fig. 3 for different values of V_0. In order to get a significant overlap of $w(q)$ with $q = q_\infty^\pm$, we prepare atomic ensembles with $\Delta q = 0.17\,G/2$ at $q_c = G/2$ realized by Bose-Einstein condensates of $2 \cdot 10^4$ atoms with a spatial extension of $\Delta x = 15\,\mu$m. The velocities of the edges are derived from two images taken at 20 ms and 60 ms, respectively. In each image the position of the edge is evaluated at the levels indicated by the arrows in the insets of Fig. 3 (50% and 25% of the maximum density). Since the momentum spread is too small to populate the infinite mass points for potentials deeper than $2E_G$ the atomic ensemble was then prepared at $q_c = G/4$ by accelerating the periodic potential to the corresponding velocity $v = v_G/2$. The resulting wave packet shapes are asymmetric exhibiting a steep edge on one side which becomes less pronounced for potentials deeper than $5\,E_G$. The obtained experimental results in Fig. 3 are in excellent agreement with the numerically calculated band structure predictions. In contrast to the good agreement of the maximum velocity for all potential depths we find that for $V_0 > 5\,E_G$ the group velocity of the center of mass is only 10% of the expected velocity deduced from the dispersion relation at $q_c = G/4$. This could be an indication of entering the tight binding regime where the nonlinear effect of self trapping, i.e. stopping and non-spreading wave packets, has been predicted by Trombettoni et al. [8]. We are currently investigating the transport properties in this regime in more detail.

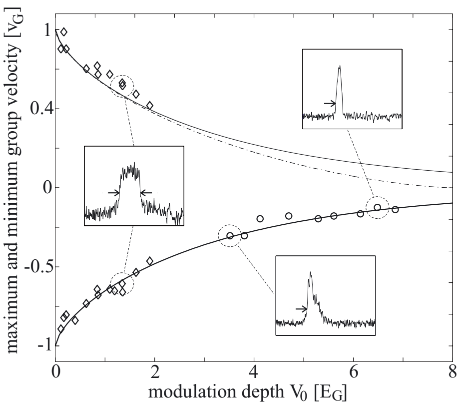

FIG. 3: Group velocities of steep edges emerging from an initial wave packet with significant overlap with $q_\infty^\pm$ in quasimomentum space. The measured velocities of the indicated positions (arrows in insets) agree very well with the expected maximum and minimum velocity in the lowest band (solid line) corresponding to the infinite masses. The dashed line represents the prediction of the weak potential approximation [9]. For potentials smaller than 2 E_G (diamonds) data are obtained by preparing the initial wave packet at $q = G/2$ leading to two steep edges (see inset). For higher potentials (circles) the wave packet is prepared at $q = G/4$ to ensure population of the quasimomentum corresponding to infinite mass.

In conclusion, we have demonstrated experimentally that the dispersion of atomic matter waves in a waveguide can be controlled using a weak periodic potential. Matter wave packets with positive, negative and infinite effective masses are studied in the regime of weak and intermediate potential heights. The preparation of matter waves with engineered dispersion ($m_{\text{eff}} < 0$) is an important prerequisite for the experimental investigation of atomic gap solitons and other effects arising from the coherent interplay of nonlinearity and dispersion in periodic potentials.

We wish to thank J. Mlynek for his generous support, A. Sizmann and B. Brezger for many stimulating discussions, and J. Bellanca, and K. Forberich for their help in building up the experiment. This work was supported by Deutsche Forschungsgemeinschaft, Emmy Noether Program, and by the European Union, Contract No. HPRN-CT-2000-00125.

[1] *Bose-Einstein condensation in atomic gases*, ed. by M. Inguscio, S. Stringari,and C. Wieman, (IOS Press, Amsterdam 1999)

[2] G.P. Agrawal, *Applications of Nonlinear Fiber Optics*

(Academic Press, San Diego, 2001).

[3] M. Ben Dahan, E. Peik, J. Reichel, Y. Castin, and C. Salomon, Phys.Rev.Lett. **76** 4508 (1996).

[4] O. Morsch, J. Müller, M. Cristiani, D. Ciampini, and E. Arimondo, Phys. Rev. Lett. **87**, 140402 (2001).

[5] S. Burger, F.S. Cataliotti, C. Fort, F. Minardi, M. Inguscio, M.L. Chiofalo, and M.P. Tosi, Phys. Rev. Lett. **86**, 4447 (2001).

[6] M. Krämer, L. Pitaevskii, and S. Stringari, Phys. Rev. Lett **88**, 180404 (2002).

[7] P. Meystre, *Atom Optics* (Springer Verlag, New York, 2001) p 205, and references therein.

[8] A. Trombettoni and A. Smerzi, Phys. Rev. Lett. **86**, 2353 (2001).

[9] N. Ashcroft and N. Mermin, *Solid State Physics* (Saunders, Philadelphia, 1976).

[10] J. Hecker-Denschlag, J.E. Simsarian , H. Häffner, C. McKenzie, A. Browaeys, D. Cho, K. Helmerson, S.L. Rolston and W.D. Phillips, J. Phys. B **35**, 3095 (2002), and references therein.

[11] M. Steel and W. Zhang, cond-mat/9810284 (1998).

[12] G. Agrawal, *Nonlinear Fiber Optics* (Academic Press, San Diego, 1995).

[13] Y. Castin, and R. Dum, Phys.Rev.Lett. **77**, 5315 (1996); Y. Kagan, E.L. Surkov, and G.V. Shlyapnikov, Phys.Rev. A **54** R1753 (1996)

[14] M.J. Potasek, G.P. Agrawal, S.C. Pinault, J.Opt.Soc.Am. B **3**, 205 (1986).

[15] M. Kozuma, L. Deng, E.W. Hagley, J. Wen, R. Lutwak, K. Helmerson, S.L. Rolston, and W.D. Phillips, Phys.Rev.Lett. **82** 871 (1999).

3.4 Continuous Dispersion management

As a natural continuation of the experiments on dispersion management and the linear dynamics in lattice potentials, a series of experiments is presented in this section, where the technique of continuous dispersion management is investigated. With this technique the broadening of a wave packet in real space is suppressed by continuously altering the dispersion from normal to anomalous dispersion and vice versa. The experimental results together with a numerical investigation reveal the nature of the influence of the nonlinear atom-atom interaction in the different dispersion regimes.

In a modified setup, where the waveguide encloses an angle of 21° with the counter propagating beams of the lattice potential, a coupling between the longitudinal and the transverse motion of the wave packet by the lattice potential is realized. In this setup a transverse oscillation in real space leads to an oscillation in quasi momentum space of the lattice potential and thus allows to implement a continuous dispersion management scheme.

In addition the complex 3D wave packet dynamics is investigated numerically. For this purpose first the semiclassical equations of motion of a single particle are solved. From the results the complicated trajectory in longitudinal momentum space is extracted and reinserted as a pseudo force in a numerical propagation of the 1D NPSE. This approximation allows to circumvent tedious 3D calculations and is able to reproduce all the observed features of the complex wave dynamics. A detailed derivation of the equations of motion used in the numerical analysis of the experiments is given in section 3.4.2.

The numerical results allow an insight into the dynamics in momentum space. It is therefore possible to understand the complex nonlinear wave dynamics identifying processes known from nonlinear optics, such as self phase modulation (Agrawal, 1995) and the transient formation of higher order solitons (Agrawal, 2001).

3.4.1 Publication: Linear and nonlinear dynamics of matter wave packets in periodic potentials

The experiments on the continuous dispersion management are published in (Anker *et al.*, 2003) and are summarized in the following.

Continuous dispersion management In the first experiment the atomic wave packet is accelerated with a tight binding lattice potential across the edge of the Brillouin zone. The hereby exited transverse oscillation results in a forced oscillation in quasi momentum space around the Brillouin zone boundary, such that the dispersion is altered from normal to anomalous dispersion. Initially a radiation of atoms is observed, a process induced by the strong initial nonlinear atom-atom interaction. A remaining wave packet with reduced atomic density is then observed, which shows suppressed dispersion - continuous dispersion management.

Nonlinear dynamics The initial nonlinear dynamics is investigated more closely in a second experiment, where the wave packet is prepared initially at the Brillouin zone boundary. By comparison with the numerical results, the typical process of compression in real space combined with a broadening in momentum space and vice versa can be attributed to a transient formation of higher order solitons.

Linear and nonlinear dynamics of matter wave packets in periodic potentials

Th. Anker, M. Albiez, B. Eiermann, M. Taglieber and M. K. Oberthaler

Kirchhoff Institut für Physik, Universität Heidelberg, Im Neuenheimer Feld 227, 69120 Heidelberg

thomas.anker@kip.uni-heidelberg.de

http://www.kip.uni-heidelberg.de/matterwaveoptics

Abstract: We investigate experimentally and theoretically the nonlinear propagation of ^{87}Rb Bose Einstein condensates in a trap with cylindrical symmetry. An additional weak periodic potential which encloses an angle with the symmetry axis of the waveguide is applied. The observed complex wave packet dynamics results from the coupling of transverse and longitudinal motion. We show that the experimental observations can be understood applying the concept of effective mass, which also allows to model numerically the three dimensional problem with a one dimensional equation. Within this framework the observed slowly spreading wave packets are a consequence of the continuous change of dispersion. The observed splitting of wave packets is very well described by the developed model and results from the nonlinear effect of transient solitonic propagation.

OCIS codes: (270.5530) Pulse propagation and solitons; (020.0020) Atomic and molecular physics; (350.4990) Particles

---

References and links

1. "Bose-Einstein condensation in atomic gases," ed. by M. Inguscio, S. Stringari, and C. Wieman, (IOS Press, Amsterdam 1999)
2. F.S. Cataliotti, S. Burger, S. C. Fort, P. Maddaloni, F. Minardi, A. Trombettoni, A. Smerzi, and M. Ingusio, "Josephson Junction Arrays with Bose-Einstein Condensates", Science **293** 843 (2001).
3. A. Trombettoni and A. Smerzi, "Discrete Solitons and Breathers with Dilute Bose-Einstein Condensates," Phys. Rev. Lett. **86** 2353 (2001).
4. M. Steel and W. Zhang, "Bloch function description of a Bose-Einstein condensate in a finite optical lattice," cond-mat/9810284 (1998).
5. P. Meystre, *Atom Optics* (Springer Verlag, New York, 2001) p 205, and references therein.
6. The experimental realization in our group will be published elsewhere.
7. V.V. Konotop, M. Salerno, "Modulational instability in Bose-Einstein condensates in optical lattices," Phys. Rev. A **65** 021602 (2002).
8. N. Ashcroft and N. Mermin, *Solid State Physics* (Saunders, Philadelphia, 1976).
9. A.A. Sukhorukov, D. Neshev, W. Krolikowski, and Y.S. Kivshar, "Nonlinear Bloch-wave interaction and Bragg scattering in optically-induced lattices," nlin.PS/0309075.
10. B. Eiermann, P. Treutlein, Th. Anker, M. Albiez, M. Taglieber, K.-P. Marzlin, and M.K. Oberthaler, "Dispersion Management for Atomic Matter Waves," Phys. Rev. Lett. **91** 060402 (2003).
11. M. Kozuma, L. Deng, E.W. Hagley, J. Wen, R. Lutwak, K. Helmerson, S.L. Rolston, and W.D. Phillips, "Coherent Splitting of Bose-Einstein Condensed Atoms with Optically Induced Bragg Diffraction," Phys. Rev. Lett. **82** 871 (1999).

12. B.P. Anderson, and M.A. Kasevich, “Macroscopic Quantum Interference from Atomic Tunnel Arrays,” Science **282** 1686 (1998);
13. O. Morsch, J. Müller, M. Cristiani, D. Ciampini, and E. Arimondo, “Bloch Oscillations and Mean-Field Effects of Bose-Einstein Condensates in 1D Optical Lattices,” Phys. Rev. Lett. **87** 140402 (2001).
14. C.F. Bharucha, K.W. Madison, P.R. Morrow, S.R. Wilkinson, Bala Sundaram, and M.G. Raizen, “Observation of atomic tunneling from an accelerating optical potential,” Phys. Rev. A **55** R857 (1997)
15. L. Salasnich, A. Parola, and L. Reatto, “Effective wave equations for the dynamics of cigar-shaped and disk-shaped Bose condensates,” Phys. Rev. A **65** 043614 (2002).
16. G.P. Agrawal, *Applications of Nonlinear Fiber Optics* (Academic Press, San Diego, 2001).
17. G.P. Agrawal, *Nonlinear Fiber Optics* (Academic Press, San Diego, 1995).
18. R.G. Scott, A.M. Martin, T.M. Fromholz,S. Bujkiewicz, F.W. Sheard, and M. Leadbeater, “Creation of Solitons and Vortices by Bragg Reflection of Bose-Einstein Condensates in an Optical Lattice,” Phys. Rev. Lett. **90** 110404 (2003).

---

1. Introduction

The experimental investigation of nonlinear matter wave dynamics is feasible since the realization of Bose-Einstein-condensation of dilute gases [1]. The combination of this new matter wave source with periodic potentials allows for the realization of many nonlinear propagation phenomena. The dynamics depends critically on the modulation depth of the potential. For deep periodic potentials the physics is described locally taking into account mean field effects and tunneling between adjacent potential wells. In this context wave packet dynamics in Josephson junction arrays have been demonstrated experimentally [2] and nonlinear self trapping has been predicted theoretically [3]. In the limit of weak periodic potentials and moderate nonlinearity rich wave packet dynamics result due to the modification of dispersion which can be described applying band structure theory [4]. Especially matter wave packets subjected to anomalous dispersion (negative effective mass) or vanishing dispersion (diverging mass) are of great interest. In the negative mass regime gap solitons have been predicted theoretically [5] and have been observed recently [6]. Also modulation instabilities can occur [7].

The experiments described in this work reveal wave dynamics in the linear and nonlinear regime for weak periodic potentials. The observed behavior is a consequence of the special preparation of the wave packet leading to a continuous change of the effective mass and thus the dispersion during the propagation. The initial propagation is dominated by the atom-atom interaction leading to complex wave dynamics. After a certain time of propagation slowly spreading atomic wave packets are formed which are well described by linear theory. In this work we focus on the mechanisms governing the initial stage of propagation.

The paper is organized as follows: in section 2 we describe the effective mass and dispersion concept. In section 3 we present our experimental setup and in section 4 the employed wave packet preparation schemes are discussed in detail. In section 5 the experimental results are compared with numerical simulations. We show that some features of the complex dynamics can be identified with well known nonlinear mechanisms. We conclude in section 6.

2. Effective mass and dispersion concept

In our experiments we employ a weak periodic potential which leads to a dispersion relation $E_n(q)$ shown in Fig. 1(a). This relation is well known in the context of electrons in crystals [8] and exhibits a band structure. It shows the eigenenergies of the Bloch states as a function of the quasi-momentum q. The modified dispersion relation leads to a change of wavepacket dynamics due to the change in group velocity $v_g(q) = 1/\hbar\, \partial E/\partial q$ (see Fig. 1(b)), and the group velocity dispersion described by the effective mass $m_{eff} = \hbar^2(\partial^2 E/\partial q^2)^{-1}$ (see Fig. 1(c)), which is equivalent to the effective diffraction introduced in the context of light beam propagation in optically-induced photonic lattices [9]. In our experiment only the lowest band is populated, which is characterized by two dispersion regimes, normal and anomalous dispersion, corresponding to positive and negative effective mass. A pathological situation arises at the quasimomentum $q^{\pm}_{\infty}$, where the group velocity $v_g(q)$ is extremal, $|m_{\text{eff}}|$ diverges and thus the dispersion vanishes.

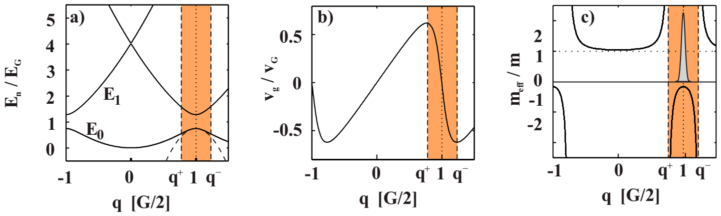

Fig. 1. (a) Band structure for atoms in an optical lattice with $V_0 = 1.2\,E_{\text{rec}}$ (solid), parabolic approximation to the lowest energy band at $q = \pi/d = G/2$ (dashed), corresponding group velocity (b) and effective mass (c) in the lowest energy band. The vertical dashed lines at $q = q^{\pm}_{\infty}$ indicate where $|m_{\text{eff}}| = \infty$. The shaded region shows the range of quasimomenta where the effective mass is negative.

In the following we will show that the two preparation schemes employed in the experiment lead to a continuous change of the quasimomentum distribution, and thus to a continuous change of dispersion. One of the preparation schemes allows to switch periodically from positive to negative mass values and thus a slowly spreading wave packet is formed. This is an extension of the experiment reporting on dispersion management [10]. The second preparation gives further insight into the ongoing nonlinear dynamics for the initial propagation.

3. Experimental setup

The wave packets in our experiments have been realized with a ^{87}Rb Bose-Einstein condensate (BEC). The atoms are collected in a magneto-optical trap and subsequently loaded into a magnetic time-orbiting potential trap. By evaporative cooling we produce a cold atomic cloud which is then transferred into an optical dipole trap realized by two focused Nd:YAG laser beams with $60\,\mu$m waist crossing at the center of the magnetic trap (see Fig.2(a)). Further evaporative cooling is achieved by lowering the optical potential leading to pure Bose-Einstein condensates with $1 \cdot 10^4$ atoms in the $|F = 2, m_F = +2\rangle$ state. By switching off one dipole trap beam the atomic matter wave is released into a trap acting as a one-dimensional waveguide with radial trapping frequency $\omega_{\text{r}} = 2\pi \cdot 100\,\text{Hz}$ and longitudinal trapping frequency $\omega_{\|} = 2\pi \cdot 1.5\,\text{Hz}$. It is important to note that the dipole trap allows to release the BEC in a very controlled way leading to an initial mean velocity uncertainty smaller than 1/10 of the photon recoil velocity.

The periodic potential is realized by a far off-resonant standing light wave with a single beam peak intensity of up to $1\,\text{W}/\,\text{cm}^2$. The chosen detuning of 2 nm to the blue off the D2 line leads to a spontaneous emission rate below 1 Hz. The standing light wave and the waveguide enclose an angle of $\theta = 21^\circ$ (see Fig. 2(b)). The frequency and phase of the individual laser beams are controlled by acousto-optic modulators driven by a two channel arbitrary waveform generator allowing for full control of the velocity and amplitude of the periodic potential. The light intensity and thus the absolute value of the potential depth was calibrated independently by analyzing results on Bragg scattering [11] and Landau Zener tunneling [12, 13, 14].

The wave packet evolution inside the combined potential of the waveguide and the lattice is studied by taking absorption images of the atomic density distribution after a variable time delay. The density profiles along the waveguide, $n(x,t)$, are obtained by integrating the absorption images over the transverse dimension.

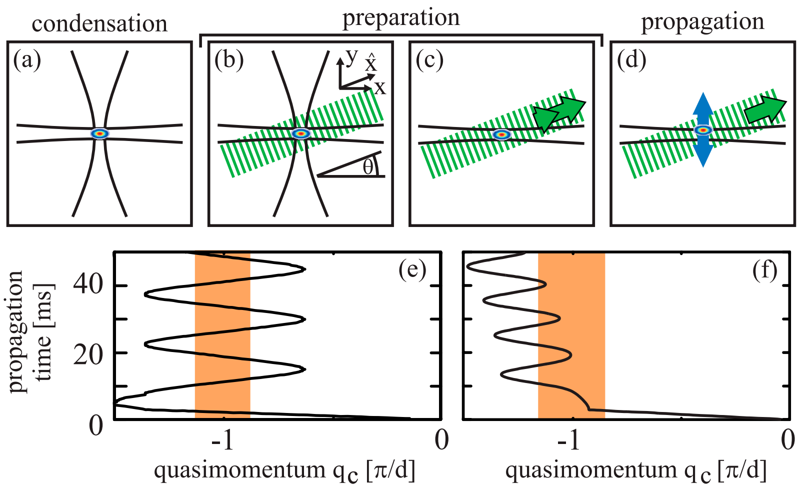

Fig. 2. Scheme for wave packet preparation (a-d). (a) initial wave packet is obtained by condensation in a crossed dipole trap. (b) A stationary periodic potential is ramped up adiabatically preparing the atoms at quasimomentum $q_c = 0$ in the lowest band. (c),(d) The periodic potential is accelerated to a constant velocity. (e) shows the numerically deduced quasimomentum shift for the preparation method I described in the text. (f) The motion of the center quasimomentum for the preparation method II described in the text. The additional shift to higher quasimomenta for long times results from the residual trap in the direction of the waveguide. The shaded area represents the quasimomenta corresponding to negative effective mass.

4. Dynamics in reciprocal space

In our experimental situation an acceleration of the periodic potential to a constant velocity leads to a collective transverse excitation as indicated in Fig. 2(d). Since the transverse motion in the waveguide has a non vanishing component in the direction of the periodic potential due to the angle θ, a change of the transverse velocity leads to a shift of the central quasimomentum of the wave packet. The coupling between the transverse motion in the waveguide and the motion along the standing light wave gives rise to a nontrivial motion in reciprocal (see Fig. 2(e,f)) and real space.

The appropriate theoretical description of the presented experimental situation requires the solution of the three dimensional nonlinear Schrödinger equation (NLSE) and thus requires long computation times. In order to understand the basic physics we follow a simple approach which solves the problem approximately and explains all the features observed in the experiment. For that purpose we first solve the semiclassical equations of motion of a particle which obeys the equation $\vec{F} = M^{*}\ddot{\vec{x}}$ where M^{*} is a mass tensor describing the directionality of the effective mass. We deduce the time dependent quasimomentum $q_c(t)$ in the direction of the periodic potential by identifying $\hbar\dot{q}_c = F_{\hat{x}}$ and $\dot{\hat{x}} = v_g(q_c)$ (definition of $\hat{x}$ see Fig. 2(b)). Subsequently we can solve the one dimensional NPSE (non-polynomial nonlinear Schrödinger equation)[15] where the momentum distribution is shifted in each integration step according to the calculated $q_c(t)$. Thus the transverse motion is taken into account properly for *narrow* momentum distributions. We use a split step Fourier method to integrate the NPSE where the kinetic energy contribution is described by the numerically obtained energy dispersion relation of the lowest band $E_0(q)$. It is important to note, that this description includes all higher derivatives of $E_0(q)$, and thus goes beyond the effective mass approximation.

In the following we discuss in detail the employed preparation schemes:

Acceleration scheme I: After the periodic potential is adiabatically ramped up to $V_0 = 6E_{rec}$ it is accelerated within 3 ms to a velocity $v_{pot} = \cos^2(\theta)1.5v_{rec}$. Then the potential depth is lowered to $V_0 = 0.52E_{rec}$ within 1.5 ms and the periodic potential is decelerated within 3 ms to $v_{pot} = \cos^2(\theta)v_{rec}$ subsequently. V_0 and v_{pot} are kept constant during the following propagation. The calculated motion in reciprocal space $q_c(t)$ is shown in Fig. 2(e).

Acceleration scheme II: The periodic potential is ramped up adiabatically to $V_0 = 0.37\,E_{rec}$ and is subsequently accelerated within 3 ms to a final velocity $v_{pot} = \cos^2(\theta) \times 1.05\,v_{rec}$. The potential depth is kept constant throughout the whole experiment. Fig. 2(f) reveals that in contrast to the former acceleration scheme the quasimomentum for the initial propagation is mainly in the negative effective mass regime.

5. Experimental and numerical results

In this section we compare the experimental results with the predictions of our simple theoretical model discussed above. The numerical simulation reveal all the experimentally observed features of the dynamics such as linear slowly spreading oscillating wave packets, nonlinear wave packet compression and splitting of wave packets. The observed nonlinear phenomena can be understood by realizing that in the negative effective mass regime the repulsive atom-atom interaction leads to compression of the wave packet in real space and to a broadening of the momentum distribution. An equivalent picture borrowed from nonlinear photon optics [16, 17] is the transient formation of higher order solitons, which show periodic compression in real space with an increase in momentum width and vice versa.

5.1. Preparation I

The experimental results for the first acceleration scheme discussed in section 4 are shown in Fig. 3. Clearly we observe that a wave packet with reduced density is formed which spreads out slowly and reveals oscillations in real space. This wave packet results from the initial dynamics characterized by two stages of compression which lead to radiation of atoms [18]. The observed behavior is well described by our numerical simulation which allows further insight into the ongoing physics.

In Fig. 3(c,d) we show the calculated momentum and real space distribution for the first 14ms of propagation. As can be seen the acceleration of the standing light wave leads to a oscillatory behavior in momentum space. For the chosen parameters the wave packet is initially dragged with a tight binding potential ($V_0 = 6E_{rec}$) over the critical negative mass regime. While the real space distribution does not change during this process, the momentum distribution broadens due to self phase modulation [16, 17]. The subsequent propagation in the positive mass regime leads to a further broadening in momentum space and real space (t=4-9ms).

The dynamics changes drastically as soon as a significant part of the momentum distribution populates quasimomenta in the negative mass regime (t=10ms). There the real space distribution reveals nonlinear compression as known from the initial dynamics of higher order solitons. This compression leads to a significant further broadening in momentum space and thus to population of quasimomenta corresponding to positive mass. This results in a spreading in real space due to the different group velocities involved and leads to the observed background. The change of the quasimomentum due to the transverse motion prohibits a further significant increase in momentum width, since the whole momentum distribution is shifted out of the critical negative mass regime at t=14ms.

The long time dynamics of the slowly spreading wave packet is mainly given by the momentum distribution marked with the shaded area for t=14ms in Fig. 3(c). The subsequent motion is dominated by the change of the quasimomentum due to the transverse motion. This leads to a periodic change from normal to anomalous dispersion and thus the linear spreading is sup-

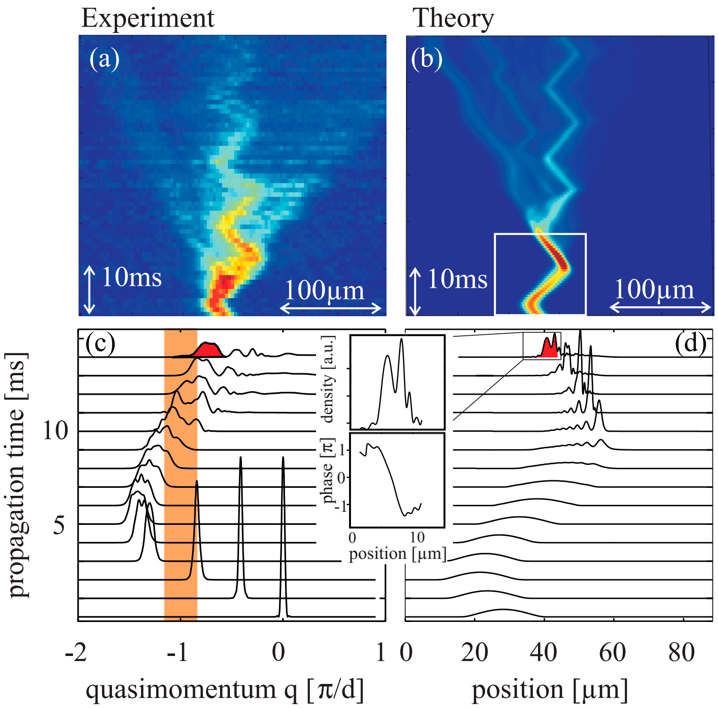

Fig. 3. Wave packet dynamics for preparation I. (a) Experimental observation of wave packet propagation. (b) Result of the numerical simulation as discussed in the text. The data is convoluted with the optical resolution of the experiment. The obtained results are in good agreement with the experimental observations. The theoretically obtained (c) quasimomentum distribution and (d) real space distribution are given for the initial 14ms of propagation. The inset reveals the phase of the observed slowly spreading wave packet.

pressed. This is an extension of our previous work on dispersion management for matter waves - continuous dispersion management.

5.2. Preparation II

This preparation scheme reveals in more detail the transient solitonic propagation leading to the significant spreading in momentum space. This results in a splitting of the wave packet which cannot be understood within a linear theory. The results are shown in Fig. 4 and the observed splitting is confirmed by our numerical simulations.

In contrast to the former preparation scheme the momentum distribution is prepared as a whole in the critical negative mass regime. Our numerical simulations reveal that the wave packet compresses quickly in real space after t=4ms which is accompanied by an expansion in momentum space. The momentum distribution which stays localized in the negative mass regime reveals further solitonic propagation characterized by an expansion in real space and narrowing of the momentum distribution (t=5-10ms). The transverse motion shifts this momentum distribution into the normal dispersion regime after 11ms of propagation resulting in a wave packet moving with positive group velocity (i.e. moving to the right in fig. 4(b)). The initial compression at t=4ms even produces a significant population of atoms in the normal mass regime which subsequently move with negative group velocity showing up as a wave packet moving to the left in Fig. 4(b). Thus the splitting in real space is a consequence of the significant nonlinear broadening in momentum space.

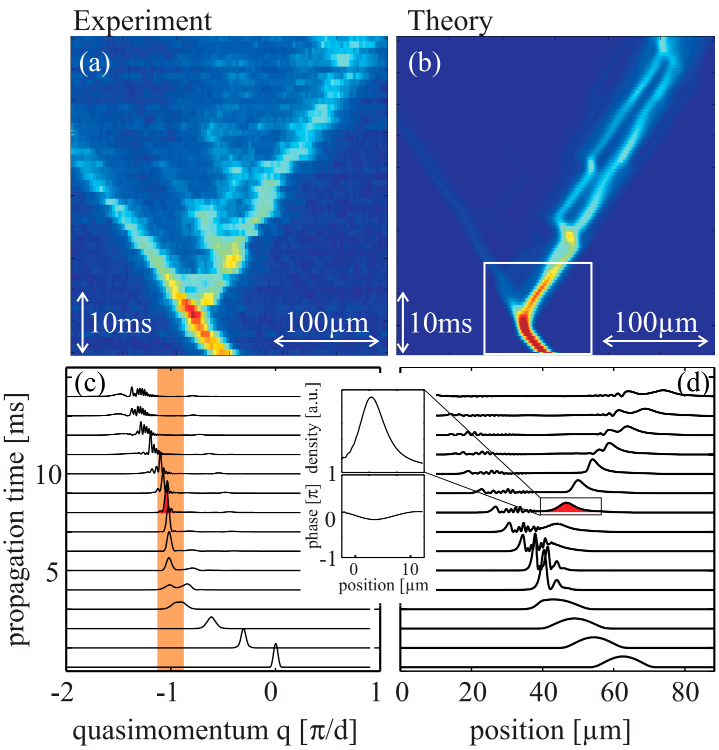

Fig. 4. Wave packet dynamics for preparation II. (a) Experimental results on wave packet propagation. (b) Result of the numerical simulation as discussed in the text. The simulation reproduces the observed wave packet splitting. The theoretically obtained (c) quasimomentum distribution and (d) real space distribution are given for the initial 14ms of propagation. The inset reveals that the transient formed wave packet has a flat phase indicating solitonic propagation.

6. Conclusion

In this paper we report on experimental observations of nonlinear wave packet dynamics in the regime of positive and negative effective mass. Our experimental setup realizing a BEC in a quasi-one dimensional situation allows the observation of wave dynamics for short times, where the nonlinearity due to the atom-atom interaction dominates and also for long times, where linear wave propagation is revealed.

We have shown that a slowly spreading wave packet can be realized by changing the quasimomentum periodically from the normal to anomalous dispersion regime. This can be viewed as an implementation of continuous dispersion management. We further investigate in detail the formation process of these packets, which are a result of the initial spreading in momentum space due to nonlinear compression. A second experiment investigates in more detail the nonlinear dynamics in the negative mass regime where the solitonic propagation leads to a significant broadening in momentum space. This shows up in the experiment as splitting of the condensate into two wave packets which propagate in opposite directions.

The developed theoretical description utilizing the effective mass tensor models the experimental system in one dimension and can explain all main features observed in the experiment.

3.4.2 Derivation of the effective 1D dynamics

The experiments on the continuous dispersion management are realized in a special setup, where the waveguide encloses an angle Θ with the counter propagating beams of the lattice potential. Thus an acceleration of the lattice potential also excites a dynamics which is transverse to the waveguide, due to the non-vanishing transverse component of the group velocity. The restoring forces of the waveguide potential, on the other hand, also induce an acceleration in the direction of the lattice potential and consequently cause a change of the quasi momentum. In the experiment continuous dispersion management is implemented by exciting a transverse oscillation, which results in an oscillation in quasi momentum space with a corresponding change of the dispersion from normal to anomalous dispersion and vice versa.

To investigate the resulting complex 3D dynamics numerically, the system is approximated by an effective 1D system. First the equation of motion of a quasi classical particle, $\vec{F} = m^* \ddot{\vec{r}}$ is studied, where the effect of the lattice potential is included by means of the effective mass tensor m^*. The force

$$\begin{pmatrix} F_{\hat{x}} \\ F_{\hat{y}} \end{pmatrix} = \begin{pmatrix} -\,m\omega_\perp^2 y \sin(\Theta) - m\, a_{\mathrm{latt}} \\ -\,m\omega_\perp^2 y \cos(\Theta) \end{pmatrix} \tag{3.15}$$

depends on the transverse trapping frequency $\omega_\perp = 2\pi \cdot 100$ Hz and the acceleration of the lattice potential a_{latt}, which is determined by the experiment sequence. The coordinate system (x, y) is given by the longitudinal and the transverse direction of the waveguide potential (see publication in the previous section) and transforms into the coordinate system $(\hat{x}, \hat{y})$ of the lattice potential according to

$$\begin{aligned} \dot{x} &= (\dot{\hat{x}} + v_{\mathrm{latt}}) \cos(\Theta) - \dot{\hat{y}} \sin(\Theta) \\ \dot{y} &= (\dot{\hat{x}} + v_{\mathrm{latt}}) \sin(\Theta) + \dot{\hat{y}} \cos(\Theta) \end{aligned} \tag{3.16}$$

where v_{latt} is the velocity of the lattice potential in the laboratory frame. Keeping in mind that along the lattice potential $F_{\hat{x}} = \hbar\dot{q}$ and $\dot{\hat{x}} = v_g(q)$, where q is the quasi momentum and $v_g(q)$ the group velocity, we can write down the first order differential equations for the quantities $q, y, v_{\hat{y}}$ and v_{latt}:

$$\begin{aligned} \dot{q} &= -\,m\omega_\perp^2 y \sin\Theta - m\, a_{\mathrm{latt}} \\ \dot{y} &= (v_g(q) + v_{\mathrm{latt}}) \sin\Theta + v_{\hat{y}} \cos\Theta \\ \dot{v}_{\hat{y}} &= m\omega_\perp^2 y \cos\Theta \\ \dot{v}_{\mathrm{latt}} &= a_{\mathrm{latt}}. \end{aligned} \tag{3.17}$$

The trajectory of the quasi momentum $q(t)$ can now be easily obtained solving the above equations numerically with a Runge-Kutta-Method.

The dynamics of the complete wave packet inside the waveguide is obtained by solving numerically the 1D NPSE. The influence of the transverse motion is taken into account by introducing a pseudo force: in each integration step the wave packet is shifted in quasi momentum space according to the above calculated quasi momentum $q(t)$.

3.5 Bright atomic gap solitons

In nature, many dynamical systems can be found, that can be described by nonlinear wave equations. In these systems basic excitations (waves), which are periodic in space and/or time can be found, which, by superposition, exhibit interference effects (wave nature). A dependence of the propagation velocity of the waves on the periodicity leads to the effect of dispersion, which makes these systems already quite complex (see section 3.3 on the dispersion management). In addition, wave dynamical systems in nature typically show a nonlinear coupling, i.e. the dynamics depends on the amplitude of the excitation. This makes the dynamics of these systems very complex (see section 3.4 on the continuous dispersion management).

Nevertheless most of the governing nonlinear wave equations were found to support a special class of stable solutions, so called solitary waves or solitons. These are single localized waves (or more precisely wave packets) with a time-independent or time-periodic shape, where the latter are called “higher order solitons”. They result from the fact that for their special wave form the effect of dispersion is exactly canceled by the nonlinear interaction. They were first discovered in nature as a single traveling wave in a channel of shallow water (Russel, 1844). Technically very important systems are solitons in optical fibers. These are short intense light pulses from lasers injected into optical fibers that maintain their shape and intensity while traveling through the fiber and thus allow a enormous increase in data bandwidth in optical communication (Mollenauer *et al.*, 1980; Agrawal, 1995). In these systems the broadening of the light pulses due to dispersion in the fiber is canceled by the nonlinear Kerr effect, i.e. the intensity dependent index of refraction. The dynamics of the envelope function $A(x,t)$ of light pulses in optical fibers is governed by the nonlinear wave equation

$$i\frac{\partial A(x,t)}{\partial x} = \left[\frac{\beta_2}{2}\frac{\partial^2}{\partial t^2} + \gamma|A(x,t)|^2\right] A(x,t), \tag{3.18}$$

well known in the field of nonlinear fiber optics (Agrawal, 1995). The equation is determined by the group velocity dispersion β_2 and the nonlinearity γ, where both depend on the fiber material and the central frequency of the laser pulse.

The knowledge from the well understood optical system can be transferred directly to the corresponding atom optical system – Bose-Einstein condensates in 1D waveguides described by the 1D Gross-Pitaevskii equation (see section 2.10)

$$i\hbar\frac{\partial}{\partial t}\Psi(x,t) = \left[-\frac{\hbar^2}{2m}\frac{\partial^2}{\partial x^2} + g_{1\mathrm{D}}N|\Psi(x,t)|^2\right] \Psi(x,t). \tag{3.19}$$

The correspondence between the optical and the atom optical system becomes clear when space x and time t are exchanged in the 1D GPE, which then becomes formally identical with eq. (3.18).

The above nonlinear equations support “bright solitons” - single wave packets with a constant or time-periodic shape - as solutions, if both the dispersion and the nonlinearity term have the same sign. In the field of atom optics bright solitons have been realized for Bose-Einstein condensates with attractive interaction, i.e. $g_{1\mathrm{D}} < 0$ (Strecker *et al.*, 2002; Khaykovich *et al.*, 2002).

In the case of opposite signs, the above equations support “dark solitons” as solutions. These are intensity/density minima in a homogeneous background. They could also be realized experimentally for Bose-Einstein condensates with repulsive interaction (Burger *et al.*, 1999).

Gap solitons In the experiments presented in this work a new class of solitons is realized, which exists only in a periodic potential - so called "gap solitons". The dynamics of the envelope $A(x,t)$ of an atomic wave packet prepared in a shallow periodic potential is described by the nonlinear wave equation

$$i\hbar\frac{\partial}{\partial t}A(x,t) = \left[-\frac{\hbar^2}{2m_{eff}(q_0)}\frac{\partial^2}{\partial x^2} + \alpha_{\mathrm{nl}}(q_0,V_0)NG(|A(x,t)|^2)\right]A(x,t) \tag{3.20}$$

(see section 3.1.2). By preparing the atomic wave packets at the Brillouin zone edge, i.e. in the regime of a negative effective mass, the realization of bright atomic solitons is possible for atoms with repulsive atom-atom interaction. The nonlinear energy of such wave packets moves the atoms energetically into the gap between the first and the second Bloch band – hence the name "gap solitons".

The experimental realization of bright atomic gap solitons in this work distinguishes itself from other works on atomic solitons by the fact that in our setup both the dispersion and the nonlinear interaction of the system are under full experimental control. In addition our setup allows the reproducible generation of single solitons. Therefore a detailed investigation of the formation process, the longtime behavior and the dependence on the system parameters is possible.

3.5.1 Publication: Bright Bose-Einstein Gap Solitons of Atoms with Repulsive Interaction

The experiments on bright atomic gap solitons are published in (Eiermann *et al.*, 2004) and are summarized in the following.

Realization The successful realization of bright atomic gap solitons is critically connected with the successful realization of coherent wave packets with a very small atom number. In order for the dispersion to be canceled by the nonlinear interaction, the kinetic energy of the wave packet must be comparable with the nonlinear energy. Given the strong interaction in ^{87}Rb the atom number for the soliton is around 200 atoms. The initial condensate atom number of around 3000 atoms, realized by evaporation, is further reduced by a Bragg pulse to around 900 - small enough to form a soliton. In a time series of absorption images the impressive formation process of the soliton is shown. Within around 45 ms excessive atoms are radiated with a single peak of constant atom number and width remaining.

Dynamical Properties The basic dynamical properties of bright first order solitons - a constant width and atom number - are confirmed experimentally. Gap solitons prepared directly at the Brillouin zone edge do not move with respect to the lattice potential. Here the experimental confirmation reveals the critical role of extern potentials - small misalignments of the optical table with respect to the gravitational acceleration result in an acceleration of the solitons in the direction opposite to the gravitational force revealing their negative mass characteristics.

Systematic Properties The very basic nature of a soliton, the balanced interplay between nonlinear interaction and dispersion determines a relation between the soliton width x_0 and the atom number N_0, and the system parameters, the transverse trapping frequency $\omega_\perp$ and the depth V_0 of the lattice potential. By varying the system parameters, this relation is verified experimentally.

Bright gap solitons of atoms with repulsive interaction

B. Eiermann[1], Th. Anker[1], M. Albiez[1], M. Taglieber[2], P. Treutlein[2], K.-P. Marzlin[3], and M.K. Oberthaler[1]
[1] *Kirchhoff Institut für Physik, Universität Heidelberg,*
Im Neuenheimer Feld 227, 69120 Heidelberg, Germany
[2] *Max-Planck-Institut für Quantenoptik und Sektion Physik der*
Ludwig-Maximilians-Universität, Schellingstr.4, 80799 München, Germany
[3] *Quantum Information Science Group Department of Physics and*
Astronomy 2500 University Drive NW Calgary, Alberta T2N 1N4 Canada
(Dated: March 3, 2004)

We report on the first experimental observation of bright matter-wave solitons for ^{87}Rb atoms with repulsive atom-atom interaction. This counter intuitive situation arises inside a weak periodic potential, where anomalous dispersion can be realized at the Brillouin zone boundary. If the coherent atomic wave packet is prepared at the corresponding band edge a bright soliton is formed inside the gap. The strength of our system is the precise control of preparation and real time manipulation, allowing the systematic investigation of gap solitons.

PACS numbers: 03.75.Be, 03.75.Lm, 05.45.Yv, 05.45.a
Keywords:

Non-spreading localized wave packets [1] - bright solitons - are a paradigm of nonlinear wave dynamics and are encountered in many different fields, such as physics, biology, oceanography, and telecommunication. Solitons form if the nonlinear dynamics compensates the spreading due to linear dispersion. For atomic matter waves, bright solitons have been demonstrated for which the linear spreading due to vacuum dispersion is compensated by the attractive interaction between atoms [2]. For repulsive atom-atom interaction dark solitons have also been observed experimentally [3].

In this letter we report on the experimental observation of a different type of solitons, which only exist in periodic potentials - bright gap solitons. For weak periodic potentials the formation of gap solitons has been predicted [4] while discrete solitons [5] should be observable in the case of deep periodic potentials. These phenomena are well known in the field of nonlinear photon optics where the nonlinear propagation properties in periodic refractive index structures have been studied [6]. In our experiments with interacting atoms a new level of experimental control can be achieved allowing for the realization of gap solitons for repulsive atom-atom interaction corresponding to a self-defocussing medium. It also opens up the way to study solitons in two- and three dimensional atomic systems [7].

In our experiment we investigate the evolution of a Bose-Einstein condensate in a quasi one-dimensional waveguide with a weak periodic potential superimposed in the direction of the waveguide. In the limit of weak atom-atom interaction the presence of the periodic potential leads to a modification of the linear propagation i.e. dispersion [8]. It has been demonstrated that with this system anomalous dispersion can be realized [9], which is the prerequisite for the realization of gap solitons for repulsive atom-atom interaction.

Our experimental observations are shown in figure 1 and clearly reveal that after a propagation time of 25ms a non-spreading wave packet is formed. The observed behavior exhibits the qualitative features of gap soliton formation such as: (a) during soliton formation excessive atoms are radiated and spread out over time, (b) solitons do not change their shape and atom number during propagation, (c) gap solitons do not move.

The coherent matter-wave packets are generated with ^{87}Rb Bose-Einstein condensates (figure 2a). The atoms

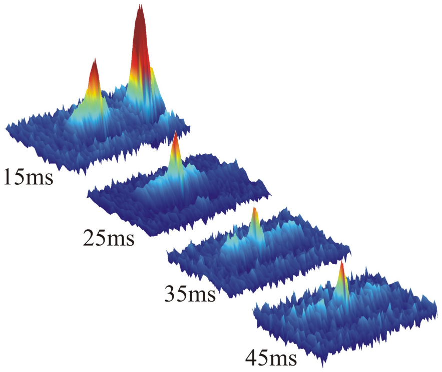

FIG. 1: Observation of bright gap solitons. The atomic density in the negative mass regime deduced from absorption images ($430\,\mu$m $\times$ $125\,\mu$m) averaged over 4 realizations is shown for different propagation times. After approximately 25 ms a small peak is formed which does neither change in shape nor in amplitude. Excessive atoms are radiated and disperse over time. After 45ms only the soliton with ~250 atoms has sufficient density to be clearly observable. The second peak at 15 ms shows the atoms which have been removed by Bragg scattering to generate an initial coherent wave packet consisting of ~900 atoms. For longer observation times those atoms move out of the imaged region.

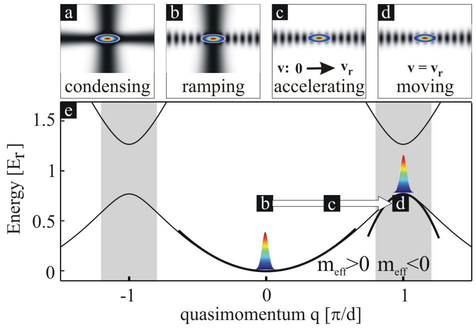

FIG. 2: Realization of coherent atomic wave packets with negative effective mass utilizing periodic potentials. (a) top view of the crossed dipole trap geometry used for Bose-Einstein condensation. (b) a periodic potential is ramped up while the atoms are still trapped in the crossed dipole trap realizing the atomic ensemble at $q_c = 0$. (c,d) the atoms are released into the one-dimensional waveguide and subsequently the periodic potential is accelerated to the recoil velocity $v_r = h/\lambda m$. This prepares the atomic wave packet at the band edge of the lowest band. (e) normal and anomalous (shaded area) dispersion regime in a periodic potential. The single preparation steps are indicated. The shown band structure is calculated for a modulation depth of $V_0 = 1\,\mathrm{E_r}$.

are initially precooled in a magnetic TOP trap using the standard technique of forced evaporation leading to a phase space density of ~ 0.03. The atomic ensemble is subsequently adiabatically transferred into a crossed light beam dipole trap (λ=1064 nm, $1/e^2$ waist 60 μm, 500 mW per beam) where further forced evaporation is achieved by lowering the light intensity in the trapping light beams. With this approach we can generate pure condensates with typically 3×10^4 atoms. By further lowering the light intensity we can reliably produce coherent wave packets of 3000 atoms. For this atom number no gap solitons have been observed. Therefore we remove atoms by Bragg scattering [10]. This method splits the condensate coherently leaving an inital wave packet with 900(300) atoms at rest. The periodic potential $V = V_0 \sin^2(\frac{2\pi}{\lambda}x)$ of periodicity $d = \lambda/2$ is realized by a far off-resonant standing light wave of wavelength $\lambda = 783\,\mathrm{nm}$. The absolute value of the potential depth was calibrated independently by analyzing results on Bragg scattering and Landau Zener tunneling [11].

After the creation of the coherent wave packet, we ramp up the periodic potential adiabatically, which prepares the atomic ensemble in the normal dispersion regime at quasimomentum $q = 0$ as indicated in figure 2. The dispersion relation for an atom moving in a weak periodic potential exhibits a band structure as a function of quasimomentum q known from the dispersion relation of electrons in crystals [12] (see figure 2e). Anomalous dispersion, characterized by a negative effective mass $m_{\mathrm{eff}} < 0$, can be achieved if the mean quasimomentum of the atomic ensemble is shifted to the Brillouin zone boundary corresponding to $q = \pi/d$. This is accomplished by switching off one dipole trap beam, releasing the atomic cloud into the one-dimensional horizontal waveguide (Fig. 2c) with transverse and longitudinal trapping frequencies $\omega_\perp = 2\pi \times 85\,\mathrm{Hz}$ and $w_{||} = 2\pi \times 0.5\,\mathrm{Hz}$. Subsequently the atomic ensemble is prepared at quasimomentum $q = \pi/d$ by accelerating the periodic potential to the recoil velocity $v_r = h/m\lambda$. This is done by introducing an increasing frequency difference between the two laser beams, creating the optical lattice. The acceleration within 1.3 ms is adiabatic, hence excitations to the upper bands by Landau-Zener transitions are negligible [11]. It is important to note that the strength of the dispersion is under full experimental control. The absolute value of $m_{\mathrm{eff}}(\mathrm{q} = \pi/\mathrm{d}) = \frac{V_0}{V_0 - 8\,\mathrm{E_r}} m$ (weak potential approximation [12]) scales with the modulation depth of the periodic potential, where $E_r = \frac{\hbar^2}{2m}\frac{\pi^2}{d^2}$ is the recoil energy.

For weak periodic potentials the full wavefunction of the condensate is well described by $\Psi(x,t) = A(x,t)u_0^{q_c}(x)\exp(iq_c x)$, where $u_0^{q_c}(x)\exp(iq_c x)$ represents the Bloch state in the lowest band $n = 0$ at the corresponding central quasimomentum q_c. Within the approximation of constant effective mass, the dynamics of the envelope $A(x,t)$ is governed, by a one-dimensional nonlinear Schrödinger equation [13]

$$i\hbar\frac{\partial}{\partial t}A(x,t) = \left(-\frac{\hbar^2}{2m_{\mathrm{eff}}}\frac{\partial^2}{\partial x^2} + g_{1d}|A(x,t)|^2\right)A(x,t)$$

with $g_{1d} = 2\hbar a\omega_\perp\alpha_{nl}$ where α_{nl} is a renormalization factor due to the presence of the periodic potential (α_{nl} =1.5 for $q = \pi/d$ in the limit of weak periodic potentials [13]), and a is the scattering length. The stationary solution for $q_c = \pi/d$ is given by

$$A(x,t) = \sqrt{N/2x_0}\,\mathrm{sech}(x/x_0)\,e^{i\hbar t/2m_{\mathrm{eff}}x_0^2},$$

where x_0 is the soliton width and m_{eff} is the effective mass at the band edge. The total number of atoms constituting the soliton is given by

$$N = \frac{\hbar}{\alpha_{nl}\omega_\perp m_{\mathrm{eff}}x_0 a}. \tag{1}$$

This quantitative feature of bright solitons can also be deduced by equating the characteristic energies for dispersion $E_D = \hbar^2/m_{\mathrm{eff}}x_0^2$ and atom-atom interaction $E_{nl} = g_{1d}|A(x=0,t)|^2$.

A characteristic time scale of solitonic propagation due to the phase evolution can also be identified. In analogy to light optics the soliton period is given by $T_S = \pi m_{\mathrm{eff}}x_0^2/2\hbar$. Solitonic propagation can be confirmed experimentally if the wave packet does not broaden over time periods much longer than T_S.

Our experimental results in figure 1 show the evolution of a gap soliton in the negative mass regime for different propagation times. The reproducible formation of a single soliton is observed if the initial wave packet is close to the soliton condition, i.e. a well defined atom number for a given spatial width. The preparation scheme utilizing the Bragg pulse leads to a wave packet containing 900 atoms with a spatial size of $\sim 2.5\,\mu$m (rms). The periodic potential depth was adjusted to $V_0 = 0.70(5)\,\mathrm{E_r}$ leading to $m_{\rm eff}/m \simeq -0.1$ at the band edge. The soliton can clearly be distinguished from the background after 25 ms, corresponding to 3 soliton periods. This is consistent with the typical formation time scale of few soliton periods given in nonlinear optics text books [14]. After 45 ms of propagation, the density of the radiated atoms drops below the level of detection and thus a pure soliton remains, which has been observed for up to 65 ms. It has been shown that for gap solitons a finite lifetime is expected due to resonant coupling to transversally excited states [15]. In order to understand the background we numerically integrated the nonpolynomial nonlinear Schrödinger equation [16]. The calculation reveals that the non-quadratic dispersion relation in a periodic potential leads to an initial radiation of atoms. However the absolute number of atoms in the observed background ($\sim$ 600 atoms) is higher than the prediction of the employed effective one-dimensional model ($\sim$ 250 atoms). Therefore we conclude that transverse excitations have to be taken into account to get quantitative agreement. This fact still has to be investigated in more detail.

In the following we will discuss the experimental facts confirming the successful realization of gap solitons. In figure 3a we compare the spreading of wave packets in the normal and anomalous dispersion regime which reveals the expected dramatic difference in wave packet dynamics. The solid circles represent the width of the gap soliton for $m_{\rm eff}/m = -0.1$, which does not change significantly over time. We deduce a soliton width of $x_0 = 6.0(9)\,\mu$m ($x_{rms} = 4.5\,\mu$m) from the absorption images where the measured rms width shown in figure 3a is deconvolved with the optical resolution of $3.8\,\mu$m (rms). In this regime, the wave packet does not spread for more than 8 soliton periods ($T_S = 7.7(23)$ ms). Since our experimental setup allows to switch from solitonic to dispersive behavior by turning the periodic potential on and off, we can directly compare the solitonic evolution to the expected spreading in the normal dispersion regime. The open circles represent the expansion of a coherent matter wave packet with 300(100) atoms in the normal mass regime $m_{\rm eff}/m = 1$.

The preparation at the band edge implies that the group velocity of the soliton vanishes. This is confirmed in figure 3b, where the relative position of the soliton with respect to the standing light wave is shown. The maximum group velocity of the lowest band is indicated by the dotted lines. In the experiment care has to be taken to align the optical dipole trap perpendicular to the gravitational acceleration within $200\,\mu$rads. Otherwise the solitons are accelerated in the direction opposite to the gravitational force revealing their negative mass characteristic.

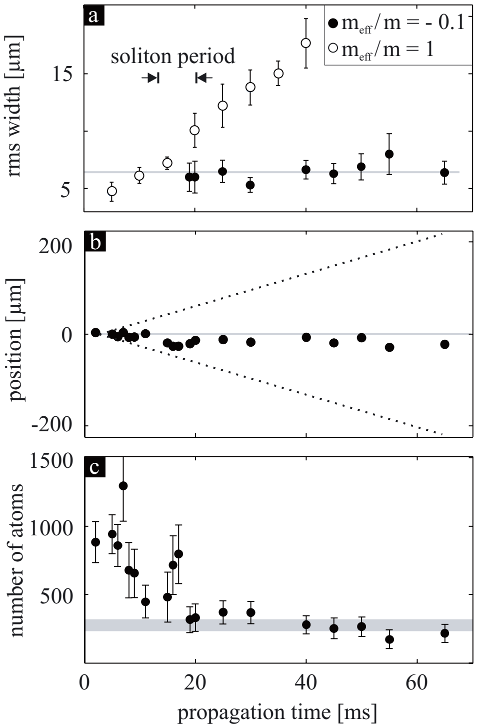

FIG. 3: Characteristic features of the observed gap soliton. (a) Comparison of expansion in the positive and negative effective mass regime for 300 atoms. While the soliton does not disperse at all over a time of 65ms, corresponding to more than 8 soliton periods (solid circles), a wave packet in the normal mass regime expands significantly (open circles). Each point represents the result of a single realization. The solid line marks the average measured r.m.s. width of gaussian fits to the solitons. (b) shows the position of the soliton in the frame of the periodic potential and reveals that a standing gap soliton has been realized. The dotted lines indicate the positions that correspond to maximum and minimum group velocity in the lowest band. (c) number of atoms in the central peak. The initial atom numbers exhibit large shot to shot fluctuations, which are reduced during the soliton formation. The predicted relation between the number of atoms and the soliton width (eq. 1) is indicated by the horizontal bar in graph c using the width deduced as shown in graph (a). Note that this comparison has been done without free parameter since all contributing parameters are measured independently.

The calculated number of atoms (eq.1) is indicated by the horizontal bar in figure 3c. The width of the bar represents the expectation within our measurement uncertainties. The observed relation between atom number and width, characteristic for a bright soliton, is in excellent agreement with the simple theoretical prediction without any free parameter.

As an additional check for soliton formation, we determine the product of atom number and soliton width as a function of the effective mass which is varied by adjusting the modulation depth of the periodic potential. Figure 4 shows the range of effective masses, for which solitons have been observed. For smaller values of $|m_{\text{eff}}|$, corresponding to smaller potential depths, Landau-Zener Tunneling does not allow a clean preparation in the negative mass regime, while for larger values the initial number of atoms differs too much from the soliton condition. The observed product of atom number and wave packet width after 40ms of propagation are shown in figure 4 and confirm the behaviour expected from eq.1. Additionally, our experimental findings reveal that the change of the scaling parameter Nx_0 in figure 4 is dominated by the change in the atom number, while the soliton width only exhibits a weak dependence on the effective mass.

The demonstration of gap solitons confirms that Bose condensed atoms combined with a periodic potential allow the precise control of dispersion and nonlinearity. Thus our setup serves as a versatile new model system for nonlinear wave dynamics. Our experiments show that gap solitons can be created in a reproducible manner. This is an essential prerequisite for the study of soliton collisions. The experiment can be realized by preparing two spatially separated wave packets at the band edge and applying an expulsive potential. Ultimately, atom number squeezed states can be engineered with atomic solitons by implementing schemes analog to those developed for photon number squeezing in light optics [17]. This is interesting from a fundamental point of view and may also have impact on precision atom interferometry experiments.

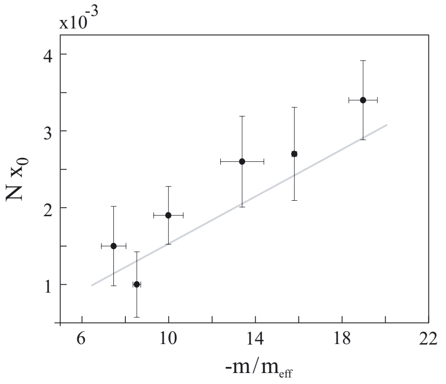

FIG. 4: Scaling properties of an gap soliton. The effective mass was varied experimentally by changing the periodic potential depth. The scaling predicted by (eq.1) is represented by the solid line and is in good agreement with our experimental observations. The errorbars represent the variation of the scaling parameter for different realizations.

We wish to thank J. Mlynek for his generous support, Y. Kivshar, E. Ostrovskaya, A. Sizmann and B. Brezger for many stimulating discussions. We thank O. Vogelsang and D. Weise for their donation of Ti:Sapphire light. This work was supported by the Deutsche Forschungsgemeinschaft, the Emmy Noether Program, and by the European Union, Contract No. HPRN-CT-2000-00125.

[1] J.S. Russel , Report of the 14th meeting of the British Association for the Advancement of Science, 311-390, Plates XLVII-LVII (1845).

[2] L. Khaykovich, et al., Science **296**, 1290-93 (2002). K.E. Strecker, G.B. Partridge, A.G. Truscott and R.G. Hulet, Nature **417**, 150-153 (2002).

[3] S. Burger, K. Bongs, S. Dettmer, W. Ertmer, K. Sengstock, Phys. Rev. Lett. **83**, 5198-5201 (1999). J. Denschlag et al., Science **287**, 97-100 (2000).

[4] P. Meystre, *Atom Optics* (Springer Verlag, New York, 2001) p 205, and references therein.

[5] A. Trombettoni and A. Smerzi, Phys. Rev. Lett. **86**, 2353 (2001).

[6] B.J. Eggleton, R.E. Slusher, C.M. deSterke, P.A. Krug, and J.E. Sipe, Phys. Rev. Lett. **76**, 1627 (1996). C.M. de Sterke, and J.E. Sipe, Progress in Optics, **33** 203 (1994). D. Neshev, A.A. Sukhorukov, B. Hanna, W. Krolikowski, and Y. Kivshar nlin.PS/0311059 (2003).

[7] H. Saito, and M. Ueda, Phys. Rev. Lett. **90**, 040403 (2003). F.Kh. Abdullaev, B.B. Baizakov and M. Salerno, Phys. Rev. E **68**, 066605 (2003). E. A. Ostrovskaya and Yu. S. Kivshar, Phys. Rev. Lett. **90**, 160407 (2003). V. Ahufinger, A. Sanpera, P. Pedri, L. Santos, M. Lewenstein cond-mat/0310042 (2003).

[8] S. Burger, F.S. Cataliotti, C. Fort, F. Minardi, M. Inguscio, M.L. Chiofalo, and M.P. Tosi, Phys. Rev. Lett. **86**, 4447 (2001).

[9] B. Eiermann, P. Treutlein, Th. Anker, M. Albiez, M. Taglieber, K.-P. Marzlin, and M.K. Oberthaler, Phys.Rev.Lett. **91**, 060402 (2003).

[10] M. Kozuma, L. Deng, E.W. Hagley, J. Wen, R. Lutwak, K. Helmerson, S.L. Rolston, and W.D. Phillips, Phys.Rev.Lett. **82** 871 (1999).

[11] B.P. Anderson, and M.A. Kasevich, Science **282** 1686 (1998); O. Morsch, J. Müller, M. Cristiani, D. Ciampini, and E. Arimondo, Phys. Rev. Lett. **87**, 140402 (2001).

[12] N. Ashcroft and N. Mermin, *Solid State Physics* (Saunders, Philadelphia, 1976).

[13] M. Steel and W. Zhang, cond-mat/9810284 (1998).

[14] G.P. Agrawal, *Applications of Nonlinear Fiber Optics* (Academic Press, San Diego, 2001). G.P. Agrawal, *Nonlinear Fiber Optics* (Academic Press, San Diego, 1995).

[15] K.M. Hilligsøe, M.K Oberthaler and K.-P. Marzlin, Phys. Rev. A **66**, 063605 (2002).

[16] L. Salasnich, A. Parola, and L. Reatto, Phys. Rev. A **65**, 043614 (2002).

[17] S.R. Friberg, S. Machida, M.J. Werner, A. Levanon, and T. Mukai, Phys. Rev. Lett. **77**, 3775 (1996).

4 Tunneling dynamics of matter waves in deep 1D lattice potentials

The tunneling dynamics of superfluids through a potential barrier is a fascinating field of research in quantum mechanics. Bose-Einstein condensates in a deep one-dimensional optical lattice potential constitute a model system for a superfluid in an array of Josephson junctions (Burger *et al.*, 2001; Cataliotti *et al.*, 2001). This system is described theoretically by a discrete nonlinear Schrödinger equation (Trombettoni, 2001). For the quantum transport in such systems intrinsically localized excitations, such as discrete solitons, breathers, nonlinear self-trapping (Trombettoni, 2001; Ahufinger *et al.*, 2004) and discrete fronts (Darmanyan *et al.*, 1999) are important.

In this chapter I report on the first experimental observation of nonlinear self-trapping for matter waves (Anker *et al.*, 2005). This effect is closely related to the effect of macroscopic self-trapping for BEC in a double well potential (Smerzi *et al.*, 1997; Albiez *et al.*, 2005). In the first part the necessary theoretical concepts, namely the tunneling modes for a BEC in a double-well potential and the discrete nonlinear Schrödinger equation are described. In the second part a detailed numerical investigation of the effect of nonlinear self-trapping is presented. In the last part the experimental results are shown and discussed together with the results of the numerical investigation.

4.1 Theory of nonlinear wave dynamics in a double well potential

Tunneling is a fundamental process in quantum dynamics. It describes the decay of the probability amplitude of localized states in a potential well of finite height. A conceptually simple and very instructive example is the tunneling dynamics in a double well potential (see figure 4.1). In such a system wave packets prepared in the left well tunnel to the right well and return, such that the maximum of the probability amplitude oscillates between both wells. The tunneling rate, in this context called Josephson-Junction, is determined by the width and the height of the barrier.

The dynamics of interacting bosons in a double well system features additional complex tunneling modes. In (Smerzi *et al.*, 1997) the tunneling dynamics of trapped Bose-Einstein condensates through a single barrier, called Boson-Josephson-Junction (BJJ), is investigated. From the Gross-Pitaevskii equation the nonlinear tunneling modes are derived in the two-mode approximation. The most intriguing are the macroscopic self-trapping modes[1], where tunneling is strongly suppressed due to the particle interaction. Following the lines of this work, in this section the basic tunneling modes of interacting

---

[1] Recently the effect of macroscopic self-trapping for BEC is observed experimentally in our group (Albiez *et al.*, 2005).

bosons are explained. The understanding of the BJJ tunneling modes is necessary for the theoretical analysis of the experiments on nonlinear self-trapping of matter waves in deep periodic potentials.

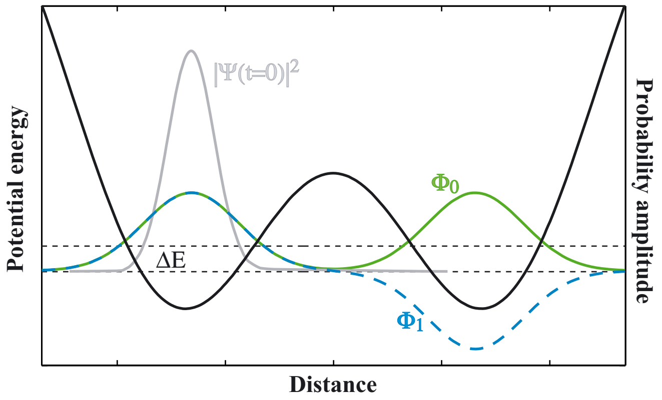

Figure 4.1: Wave dynamics in a double well potential. In a symmetric double well potential the ground state Φ_0 (green) is a symmetric and the first excited state Φ_1 (blue) is an antisymmetric state with the energy difference $E_1 - E_0 = \Delta E$. Placing initially the particle in the left well ($\Psi(t=0) = \Phi_0 + \Phi_1$, gray line) results in a sinusoidal oscillation $\Psi(t) = \Phi_0 + e^{-i\omega_T t}\Phi_1$ of the probability amplitude from the left to the right well with the tunneling frequency $\omega_T = \Delta E/\hbar$. This dynamics is called tunneling since it seems that a particle in the "quasi stationary" state $\Psi(t=0)$ tunnels through the barrier into the neighboring well.

4.1.1 Boson-Josephson junction

The dynamics of a Bose-Einstein condensate of interacting atoms in a double well potential is described by the Gross-Pitaevskii equation

$$i\hbar\frac{\partial}{\partial t}\Psi(\vec{r},t) = \left[-\frac{\hbar^2}{2m}\nabla^2 + V_{\text{ext}}(\vec{r}) + g_0|\Psi(\vec{r},t)|^2\right]\Psi(\vec{r},t), \tag{4.1}$$

where the external potential

$$V_{\text{ext}}(\vec{r}) = \frac{m}{2}\omega_\perp^2(y^2+z^2) + V_{DW}(x) \tag{4.2}$$

is realized by the sum of a 1D waveguide potential and a double well potential in longitudinal direction, as depicted in figure 4.1. In the two-mode or tight-binding approximation the ansatz for the wave function is a sum of two single condensates localized in the two wells (Milburn *et al.*, 1997; Smerzi *et al.*, 1997)

$$\Psi(\vec{r},t) = \psi_1(t)\Phi_1(\vec{r}) + \psi_2(t)\Phi_2(\vec{r}). \tag{4.3}$$

The condensates are described by the time-dependent complex amplitudes $\psi_{1,2}(t) = \sqrt{N_{1,2}(t)}e^{i\theta_{1,2}(t)}$, with the total number of atoms $N_{\text{T}} = N_1 + N_2$ and the fixed spatial wave forms $\Phi_{1,2}(\vec{r})$. By integrating eq. (4.1) with ansatz (4.3) along the spatial degrees of freedom the nonlinear two-mode equations for the amplitudes $\psi_{1,2}(t)$

$$\begin{aligned} i\hbar\frac{\partial\psi_1}{\partial t} &= U_1N_1\psi_1 - K\psi_2 && (4.4)\\ i\hbar\frac{\partial\psi_2}{\partial t} &= U_2N_2\psi_2 - K\psi_1, && (4.5)\end{aligned}$$

are obtained. These equations are governed by the nonlinear self-interaction energy $U_{1,2} = g_0 \int d\vec{r}\,|\Phi_{1,2}|^4$ and the tunneling energy

$$K = -\int d\vec{r}\left[\frac{\hbar^2}{2m}\vec{\nabla}\Phi_1\cdot\vec{\nabla}\Phi_2 + \Phi_1 V_{\mathrm{ext}}\Phi_2\right]. \tag{4.6}$$

The spatial wave functions $\Phi_{1,2}(\vec{r}) = (\Phi_+ \pm \Phi_-)/2$ can be expressed by the symmetric and antisymmetric eigenstates Φ_+ and Φ_- of the GPE (4.1) with $\int d\vec{r}\,\Phi_1\Phi_2 = 0$ and $\int d\vec{r}\,|\Phi_{1,2}|^2 = 1$. For a detailed description and a discussion of the approximation of time-indipendent spatial wave functions see (Raghavan *et al.*, 1998).

The system can be completely described by the fractional population difference $z(t) = [N_1(t) - N_2(t)]/N_{\mathrm{T}}$ and the relative phase $\phi(t) = \theta_2(t) - \theta_1(t)$. In a symmetric double well system they obey the differential equations

$$\begin{aligned} \dot{z}(\tau) &= -\sqrt{1-z^2(\tau)}\sin\Big(\phi(\tau)\Big)\\ \dot{\phi}(\tau) &= \Lambda z(\tau) + \frac{z(\tau)}{\sqrt{1-z^2(\tau)}}\cos\Big(\phi(\tau)\Big), \end{aligned} \tag{4.7}$$

with the dimensionless time $\tau = t\cdot 2K/\hbar$ and the nonlinear parameter

$$\Lambda = UN_{\mathrm{T}}/(2K), \tag{4.8}$$

which describes the ratio between the nonlinear particle interaction and the tunneling energy (for a symmetric double well $U_1 = U_2 \equiv U$).

The total energy of the above system is given by

$$H_0 = \Lambda z_0^2/2 - \sqrt{1-z_0^2}\cos(\phi_0), \tag{4.9}$$

where $H_0 \equiv H(z_0,\phi_0)$, $z_0 \equiv z(0)$ and $\phi_0 \equiv \phi(0)$. The first stationary state Ψ_+ is symmetric with $z_+ = 0$, $\phi_+ = 2n\pi$ and the energy $E_+ = -1$. The second stationary state Ψ_- is antisymmetric with $z_- = 0$, $\phi_- = (2n+1)\pi$ and $E_- = 1$.

In the case of significant particle interaction $|\Lambda| > 1$ the above system also supports stationary z-symmetry breaking states Ψ_{sb} with

$$z_{\mathrm{sb}} = \pm\sqrt{1-\frac{1}{\Lambda^2}}\,, \qquad \phi_{\mathrm{sb}} = (2n+1)\pi \tag{4.10}$$

and the corresponding energy $E_{\mathrm{sb}} = (\Lambda + 1/\Lambda)/2$.

4.1.2 Macroscopic quantum self-trapping (MQST)

In this section the tunneling modes, which are supported by the set of equations (4.7) are discussed. The character of the tunneling modes is determined by the nonlinear parameter Λ and the initial conditions z_0 and ϕ_0.

Zero-phase modes

These modes are characterized by a zero time average of the relative phase $\langle\phi(\tau)\rangle = 0$ and a zero time average of the fractional population difference $\langle z(\tau)\rangle = 0$. Two examples are shown in figure 4.2 (a) and (b). For the noninteracting case $\Lambda = 0$ the particles exhibit a sinusoidal Rabi-oscillation with frequency $\omega_{\mathrm{R}} = 2K/\hbar$. Increasing the nonlinearity Λ, initially the oscillation frequency also increases. When the nonlinearity comes close to the critical value Λ_{c}, the oscillations become more and more anharmonic with a decreasing oscillation frequency, until for $\Lambda = \Lambda_{\mathrm{c}}$ the oscillation stops (see figure 4.2 (c)).

The critical value for the nonlinearity is given by the condition

$$H_0 = \frac{\Lambda}{2} z_0^2 - \sqrt{1 - z_0^2} \cos(\phi_0) = 1, \tag{4.11}$$

i.e. the total energy must equal the energy of the second stationary state Ψ_-. For a fixed initial condition z_0 and ϕ_0 this translates into

$$\Lambda_{\mathrm{c}} = \frac{2}{z_0^2}\Big(1 + \sqrt{1 - z_0^2} \cos(\phi_0)\Big). \tag{4.12}$$

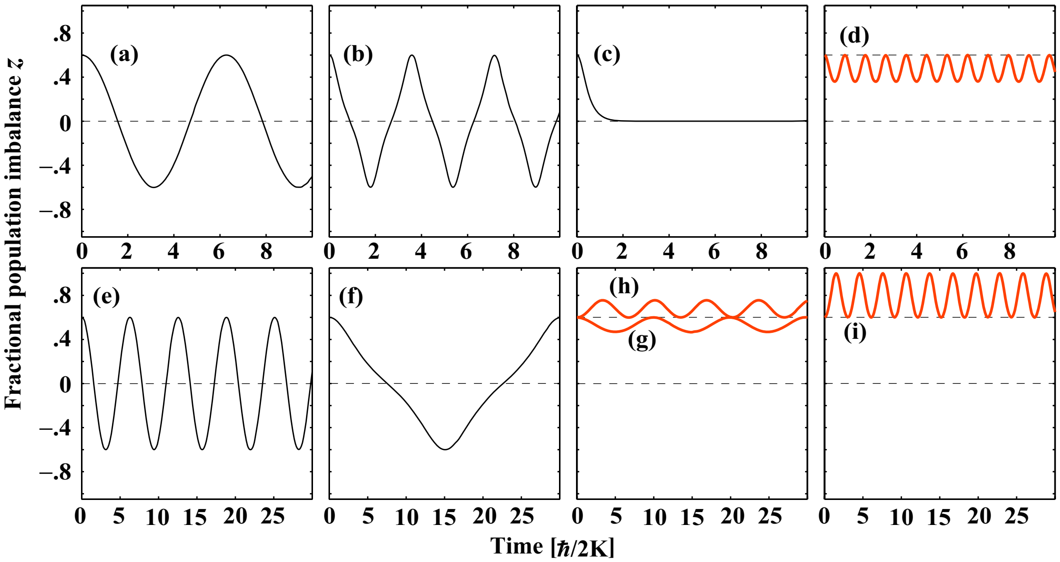

Figure 4.2: The temporal behavior of the fractional population difference $z(\tau)$ for the different tunneling modes. For initial condition $z_0 = 0.6$ and $\phi_0 = 0$: **(a, b)** $\Lambda = 0$; $0.91\times\Lambda_{\mathrm{c}}$ "zero-phase modes" **(c)** $\Lambda = \Lambda_{\mathrm{c}}$ "critical behavior" **(d)** $\Lambda = 1.5\times\Lambda_{\mathrm{c}}$ "running-phase MQST mode".
For initial condition $z_0 = 0.6$ and $\phi_0 = \pi$: **(e, f)** $\Lambda = 0$; $0.99\times\Lambda_{\mathrm{c}}$ "π-phase modes" **(g, h)** $\Lambda = 0.95\times\Lambda_{\mathrm{s}}$; $1.1\times\Lambda_{\mathrm{s}}$ first and second type of "π-phase MQST mode" **(i)** $\Lambda = 2.1\times\Lambda_{\mathrm{s}}$ "running-phase MQST mode". For a better understanding of the tunneling modes, the corresponding trajectories in the phase-plane portrait are shown in figure 4.3.

Running-phase modes: macroscopic quantum self-trapping

Increasing the nonlinearity above the critical value Λ_{c} results in a new class of tunneling modes, where the phase $\phi(\tau)$ is running freely without bound and the time average of the population imbalance $\langle z(\tau)\rangle \neq 0$ does not vanish (see figure 4.2 (d) and (i)). The population imbalance exhibits an oscillation around a fixed value $z_{\mathrm{st}} \neq z_0$ and $|z_{\mathrm{st}}| < z_0$, where the oscillation frequency increases and the amplitude decreases with increasing nonlinearity. Note that this imbalance is self-sustained, without any external potential and only due to the nonlinear particle interaction.

π-phase modes

These tunneling modes are characterized by a time average of the relative phase $\langle\phi(\tau)\rangle = \pi$. In figure 4.2 (e) and (f) these modes are shown for the initial condition $z_0 = 0.6$, $\phi_0 = \pi$, with $\Lambda = 0$ and $\Lambda = 0.99 \times \Lambda_{\mathrm{c}}$. As in the case for zero-phase modes, a harmonic oscillation can be observed for the noninteracting case. The oscillations become strongly anharmonic and the frequency goes to zero when Λ gets close to Λ_{c}. For $\Lambda < \Lambda_{\mathrm{c}}$ the time average of the population imbalance $\langle z(\tau)\rangle = 0$ vanishes.

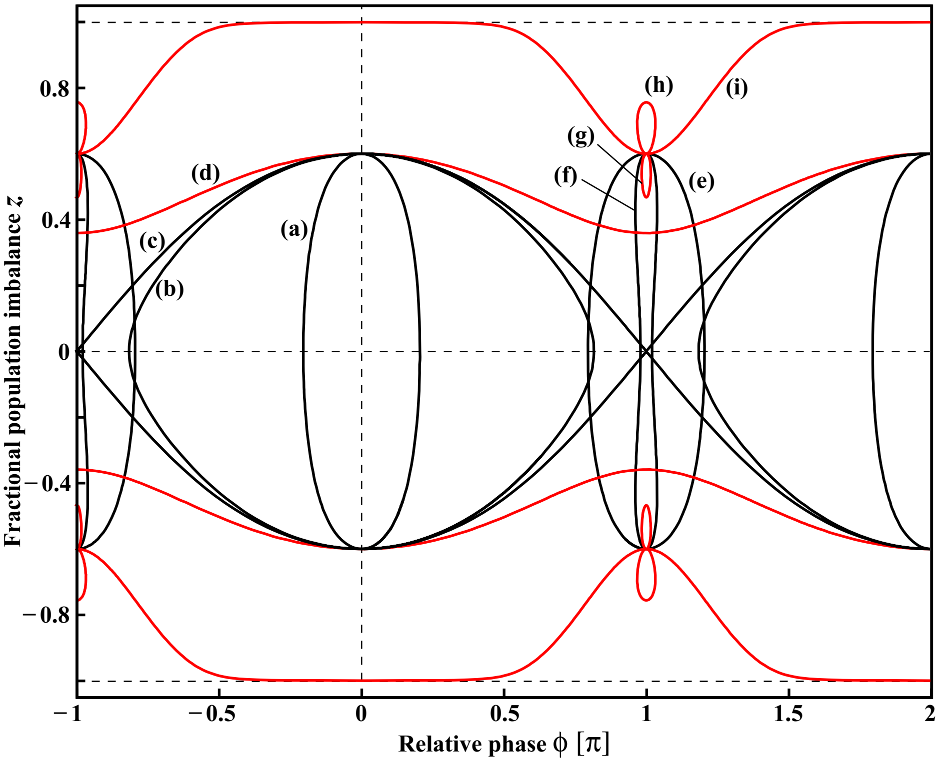

Figure 4.3: Phase-plane portrait of the dynamical variables $z(\tau)$ and $\phi(\tau)$. Initial condition $z_0 = 0.6$ and $\phi_0 = 0$ **(a, b)** $\Lambda = 0$; $0.91\times\Lambda_{\mathrm{c}}$ "zero-phase modes" **(c)** $\Lambda = \Lambda_{\mathrm{c}}$ "critical behavior" **(d)** $\Lambda = 1.5\times\Lambda_{\mathrm{c}}$ "running-phase MQST mode".
Initial condition $z_0 = 0.6$ and $\phi_0 = \pi$ **(e, f)** $\Lambda = 0$; $0.99\times\Lambda_{\mathrm{c}}$ "π-phase modes" **(g, h)** $\Lambda = 0.95\times\Lambda_{\mathrm{s}}$; $1.1\times\Lambda_{\mathrm{s}}$ first and second type of "π-phase MQST mode" **(i)** $\Lambda = 2.1\times\Lambda_{\mathrm{s}}$ "running-phase MQST mode". For details see text.

π-phase modes: macroscopic quantum self-trapping

Increasing the nonlinearity above the critical value Λ_c results in a tunneling mode, which is characterized by an oscillation of $z(\tau)$ around a fixed value $z_\mathrm{st} \neq 0$, with $|z_\mathrm{st}| < z_0$. When the nonlinearity is further increased, the self-trapping dynamics changes its character at the value $\Lambda_\mathrm{s} = 1/\sqrt{1-z_0^2}$, i.e. the value of Λ for which the initial condition resembles a z-symmetry breaking stationary state Ψ_sb (see equation (4.10)). Figure 4.2 (g) and (h) show the temporal behavior of $z(\tau)$ for both the first and the second type of π-phase modes with self-trapping.

A further increase of the nonlinearity results in a change of the self-trapping dynamics at $\Lambda = 2 \cdot \Lambda_\mathrm{s}$ from the π-phase MQST mode back to the running-phase MQST mode, where the phase $\phi(\tau)$ is running freely without bound and the time average population imbalance $\langle z(\tau)\rangle \neq 0$ vanishes. In figure 4.2 (i) this dynamics is shown for $z_0 = 0.6, \phi_0 = \pi$ and $\Lambda = 2.1 \cdot \Lambda_\mathrm{s}$.

4.2 Theory of nonlinear wave dynamics in deep lattice potentials

For Bose-Einstein condensates trapped in a deep lattice potential, the dynamics depends strongly on the ratio $\gamma = \epsilon_\mathrm{int}/\epsilon_\mathrm{kin}$ between the interaction energy between two atoms ϵ_int and the kinetic energy ϵ_kin, which is determined by the nearest neighbor tunneling.

For a lattice potential depth $V_0 \gg E_\mathrm{r}$ the tunneling is strongly suppressed and the effective value of γ can become very large. In this strong coupling regime, the system is described by the Bose-Hubbard model, where single bosons, hopping from site to site with hopping amplitude J, interact with an on-site repulsion U (Fisher *et al.*, 1989). In this regime fascinating nontrivial many body effects, such as the superfluid to Mott-insulator transition (Jaksch *et al.*, 1998; Greiner *et al.*, 2002) have been observed.

The experiments on nonlinear self-trapping are situated in the weak interaction limit $\gamma \ll 1$, where the tunneling energy is large compared to the interaction energy between two atoms. The dynamics can therefore be described by a macroscopic wave function and the Gross-Pitaevskii equation (Zwerger, 2003). If in addition the chemical potential is small compared to the trap depth of a single well, a tight binding picture can be used to describe the system. In this regime the condensate effectively consists of tiny BEC's in each well, which are described by a localized macroscopic wave function and are coupled due to tunneling between the lattice wells.

If the chemical potential in a lattice site is much smaller than the vibrational level spacing, the localized wave function can be well approximated by the noninteracting ground state wave function. For matter waves trapped in a 1D waveguide with a superimposed lattice potential, the localized wave function is given by a Gaussian ground state in transverse direction and a localized Wannier function in longitudinal direction. With this ansatz, the 3D Gross-Pitaevskii equation can be reduced to a 1D discrete nonlinear Schrödinger equation (DNLS) (Trombettoni, 2001). The system is then described by a local wave function at each lattice site, where only the local number of atoms and the local macroscopic phase vary in time. The properties of the Wannier functions and the derivation of the DNLS are described in section 4.2.1 and 4.2.2, respectively.

If the chemical potential is slightly larger than the transverse vibrational level spacing, the broadening of the ground state wave function due to the repulsive interaction has to be taken into account. Therefore the local wave functions become implicitly time-dependent through the local number of atoms. In this case the dynamics can be described approximately by an effective 1D discrete nonlinear equation (DNL) (Smerzi, 2003). The derivation of the DNL is described in section 4.2.3.

The numerical implementation of the DNLS and the DNL are shown in section 4.2.4.

4.2.1 Localized Wannier function

Bloch states are completely delocalized energy eigenstates of a periodic potential (see section 3.1.1). In contrast to this, Wannier functions constitute an orthogonal and normalized set of wave functions that are maximally localized to individual lattice sites. The Wannier function in the n^{th} Bloch band of the lattice potential is given by (see e.g. Ashcroft/Mermin, 1976)

$$w_n(x - x_i) = \mathrm{N}^{1/2} \sum_{q \in BZ} e^{(-iqx_i)} \cdot \phi_q^{(n)}(x), \tag{4.13}$$

where x_i is the position of the i^{th} lattice site, $\phi_q^{(n)}(x)$ are the Bloch states and N is a normalization constant. The sum is carried out over one Brillouin zone.

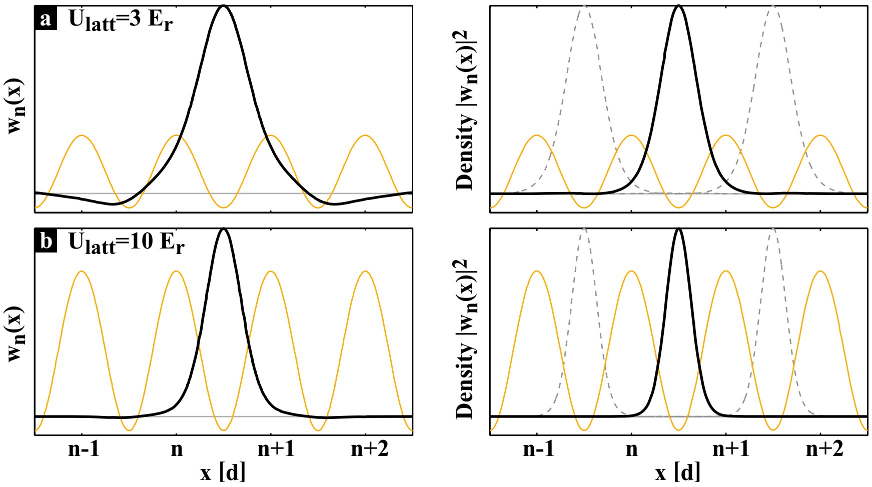

Figure 4.4: Wannier function and probability density for a lattice potential depth of a) $3\,E_\mathrm{r}$ and b) $10\,E_\mathrm{r}$. With increasing lattice potential depth the side lobes of the Wannier function vanish. This corresponds to a decreasing tunneling probability.

Unfortunately, Wannier functions have a serious drawback if computed by means of definition (4.13). Their behavior is quite erratic, and they are not well-localized. This stems from the fact that every Bloch function $\phi_q^{(n)}(x)$ has its own indeterminate phase factor. As long as the n^{th} band is energetically separate from all other bands, this problem can be circumvented by choosing the phases of $\phi_q^{(n)}(x)$ such that for a given point x (Klöckner, 2004)

$$\arg\left(\phi_q^{(n)}(x)\right) = \arg\left(\phi_{q'}^{(n)}(x)\right) \quad \text{for} \quad q, q' \in BZ. \tag{4.14}$$

In figure 4.4 the Wannier functions for a potential depth of $3\,E_\mathrm{r}$ and $10\,E_\mathrm{r}$ are shown. The Matlab© code for the numerical calculation of Wannier states is given in the appendix

A.5. Wannier functions describe atoms that are localized in a single lattice well. The side lobes of the Wannier functions, which are clearly visible for shallow lattice potentials, describe the probability of finding the atom in the neighboring sites through tunneling. The corresponding tunneling matrix element K can be obtained by the overlap integral

$$K = -\int dx \left[\frac{\hbar^2}{2m}\vec{\nabla} w_n(x - x_i)\vec{\nabla} w_n(x - x_{i+1}) + w_n(x - x_i)V_{\mathrm{latt}} w_n(x - x_{i+1})\right], \quad (4.15)$$

where V_{latt} is the lattice potential.

4.2.2 1D discrete nonlinear Schrödinger equation

The full 3D dynamics for a Bose-Einstein condensate in a horizontal waveguide with a superimposed 1D lattice potential is given by the Gross-Pitaevskii equation

$$i\hbar\frac{\partial}{\partial t}\Psi(\vec{r},t) = \left[-\frac{\hbar^2}{2m}\nabla^2 + V_{\mathrm{ext}}(\vec{r}) + g_0|\Psi(\vec{r},t)|^2\right]\Psi(\vec{r},t), \quad (4.16)$$

where the external potential

$$V_{\mathrm{ext}}(\vec{r}) = \frac{m}{2}(\omega_\perp^2 \vec{r}_\perp^{\,2} + \omega_\parallel^2 x^2) + s \cdot E_{\mathrm{r}} \cos^2(k_l x). \quad (4.17)$$

is the sum of the waveguide and the lattice potential. The amplitude of the lattice potential is given in recoil energies. In the tight binding limit the macroscopic wave function is well described by a sum of single condensate functions

$$\Psi(\vec{r},t) = \sqrt{N_{\mathrm{T}}}\sum_n \psi_n(t)\Phi(\vec{r} - \vec{r}_n), \quad (4.18)$$

where N_{T} is the total number of atoms and $\Phi(\vec{r} - \vec{r}_n)$, with $\int d\vec{r}\,\Phi_n^2 = 1$ is the localized spatial wave function at lattice site n. $\psi_n(t) = \sqrt{N_n(t)/N_{\mathrm{T}}}e^{i\theta_n(t)}$ is the n^{th} amplitude, where N_n and θ_n are the number of atoms and the phase at site n, respectively.

In this approximation the chemical potential in a lattice site is assumed to be much smaller than the vibrational level spacing. Therefore the spatial wave function $\Phi(\vec{r} - \vec{r}_n)$ can be well approximated by the transverse oscillator ground state wave function and the Wannier function in longitudinal direction $\Phi(\vec{r} - \vec{r}_n) \propto \exp(-\vec{r}_\perp^{\,2}/\sigma_\perp^2) \cdot w(x - x_n)$. Note that the spatial shape does not depend on the number of atoms. The trapping frequency in a single lattice well in longitudinal direction is given by $\omega_{\mathrm{latt}} = 2\sqrt{s}\cdot\omega_{\mathrm{r}}$ in harmonic approximation. For a typical lattice potential depth of $s \sim 10$ the ground state width $a_{HO} = \sqrt{\hbar/m\omega_{\mathrm{r}}}$ is much smaller than the lattice spacing $\lambda/2$. Thus, to a good approximation, neighboring wave functions do not overlap, i.e. $\int d\vec{r}\,\Phi_n\Phi_{n+1} \simeq 0$. With ansatz 4.18 the GPE 4.16 is integrated along the spatial degrees of freedom, to obtain the discrete nonlinear Schrödinger equation (DNLS) (Trombettoni, 2001)

$$i\frac{\partial\psi_n}{\partial\tau} = -\frac{1}{2}(\psi_{n-1} + \psi_{n+1}) + (\epsilon_n + \Lambda|\psi_n|^2)\psi_n. \quad (4.19)$$

This equation is governed by the dimensionless on-site energies

$$\epsilon_n = \frac{1}{2K}\int d\vec{r}\left[\frac{\hbar^2}{2m}(\vec{\nabla}\Phi_n)^2 + V_{\mathrm{ext}}\Phi_n^2\right], \quad (4.20)$$

the tunneling energy

$$K = -\int d\vec{r} \left[\frac{\hbar^2}{2m} \vec{\nabla}\Phi_n \cdot \vec{\nabla}\Phi_{n+1} + \Phi_n V_{\mathrm{ext}} \Phi_{n+1} \right], \tag{4.21}$$

the nonlinearity parameter

$$\Lambda = \frac{g_0 N_{\mathrm{T}}}{2K} \int d\vec{r}\, \Phi_n^4 \tag{4.22}$$

and the dimensionless time $\tau = t \cdot 2K/\hbar$.

The tunneling energy integral can be calculated assuming a 1D situation and using Wannier states as in eq. (4.15). The integration in transverse direction can be neglected, since $\int d\vec{r}\, \Phi_n \Phi_{n+1} \simeq 0$. Alternatively K can be calculated by means of the width of the lowest Bloch band (for the numerical calculation see section 3.1.1)

$$K = \left[\max(E_q^{(0)}) - \min(E_q^{(0)}) \right] /4. \tag{4.23}$$

For deep lattice potentials ($s \gg 1$) the tunneling energy is given approximately by the analytic expression (Zwerger, 2003)

$$K = \frac{4}{\sqrt{\pi}} E_{\mathrm{r}} (s)^{3/4} \exp(-2s^{1/2}). \tag{4.24}$$

From K the tunneling time $\tau = \hbar/(2K)$ can be obtained, which gives the time scale of the tunneling dynamics of the system and increases approximately exponentially with increasing potential depth (see figure 4.5).

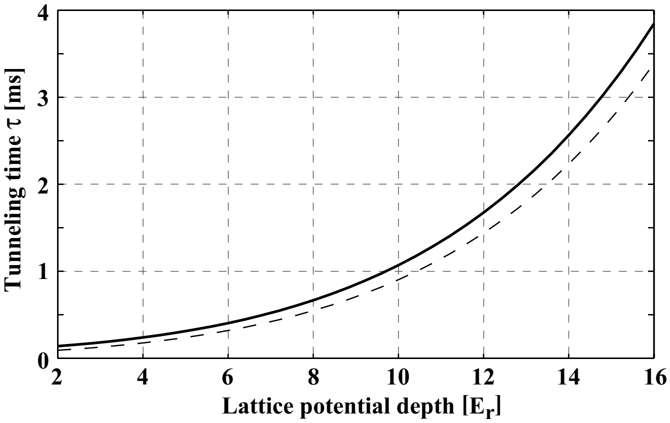

Figure 4.5: Tunneling time $\tau = \hbar/(2K)$ given by the numerically obtained width of the lowest Bloch band (black line) and by the analytic approximation (4.24) (dashed line). The time scale of the dynamics in a periodic potential is given by the tunneling time. Adiabatic changes of the potential depth, e.g. must be carried out on a time scale $T \gg \tau$.

Since the local spatial functions Φ_n have all the same shape, the lattice and the transverse trapping potential only contribute with an overall energy offset to the on-site energies ϵ_n. Only the weak longitudinal trapping potential of the waveguide shows a dependence on the lattice position n. Therefore the relevant on-site energies are given by

$$\epsilon_n = 1/2\, m\omega_{\|}^2 (n \cdot d)^2. \tag{4.25}$$

The nonlinearity parameter Λ is the ratio between the nonlinear energy with all the atoms concentrated in one site and the tunneling energy. The physical meaning of this ratio is discussed together with the effect of nonlinear self-trapping in section 4.4.2. In contrast to the calculation of K, here the 3D integral must be carried out, since both the lattice potential and the transverse trapping potential have an influence on the local atomic density $\rho = |\Phi_n|^2$. For the calculation of Λ the local condensate function can be approximated by a 3D Gaussian function $\Phi_n \propto \exp(-r^2/2\sigma_\perp^2) \cdot \exp(-x^2/2\sigma_{\mathrm{latt}}^2)$ and therefore

$$\Lambda = \frac{g_0 N_{\mathrm{T}}}{2K} \cdot \frac{1}{(2\pi)^{3/2}\sigma_\perp^2 \sigma_{\mathrm{latt}}} \tag{4.26}$$

4.2.3 General discrete nonlinear equation

A crucial point in the tight-binding approximation used in the previous section is the assumption of a local real wave function $\Phi(\vec{r} - \vec{r}_n)$, which does not depend on the local number of atoms $N_n(t)$. For experiments with ^{87}Rb, depending on the atomic density and the trap geometry, the local chemical potential can easily exceed the vibrational level spacing. In the experimental system considered in this thesis the large longitudinal trapping frequency $\omega_{\mathrm{latt}} > 2\pi \cdot 10^3$ Hz and the average local number of atoms $N_{\mathrm{loc}} \sim 100$ result in a longitudinal atomic density, which easily exceeds the maximum linear density of $\rho_x \sim 93$ atoms/μm (see section 2.1.3). The resulting nonlinear ground state will then broaden considerably in comparison to the noninteracting ground state.

In certain limits a 1D discrete nonlinear equation can still be obtained for such systems using the generalized tight binding ansatz (Smerzi, 2003)

$$\Psi(\vec{r}, t) = \sum_n \psi_n(t) \Phi_n\Big(\vec{r}, N_n(t)\Big). \tag{4.27}$$

The local complex amplitude is given by $\psi_n(t) = \sqrt{N_n(t)} e^{i\theta_n(t)}$, where $N_n(t)$ is the atom number and $\theta_n(t)$ is the phase of the n^{th} condensate. Φ_n is normalized to 1 (i.e. $\int d\vec{r}\, \Phi_n^2 = 1$). In contrast to the tight binding ansatz (4.18), the spatial wave function $\Phi_n(\vec{r}, N_n(t))$ depends implicitly on time through the local number of atoms $N_n(t)$.

Note that any explicit time-dependence, i.e. excitation of internal modes, is neglected. Only the adiabatic limit is considered, where Φ_n adapts adiabatically to the instantaneous number of atoms at site n. This approximation is satisfied if the tunneling time ($\sim \hbar/K$) is much longer than the time associated with the change of the shape of the wave function ($\sim \omega_\perp^{-1}, \omega_{\mathrm{latt}}^{-1}$) (Smerzi, 2003). By integrating the Gross-Pitaevskii equation (4.16) along the spatial degrees of freedom with ansatz (4.27) the following discrete nonlinear equation (DNL)

$$i\hbar \frac{\partial \psi_n}{\partial t} = \epsilon_n \psi_n - K(\psi_{n+1} + \psi_{n-1}) + \mu_n^{\mathrm{loc}} \psi_n \tag{4.28}$$

is obtained. The tunneling energy

$$K = -\int d\vec{r} \left[\frac{\hbar^2}{2m} \vec{\nabla}\widetilde{\Phi}_n \cdot \vec{\nabla}\widetilde{\Phi}_{n+1} + \widetilde{\Phi}_n V_{\mathrm{ext}} \widetilde{\Phi}_{n+1} \right], \tag{4.29}$$

which in principle also depends implicitly on time through $N_n(t)$, can be calculated using $\widetilde{\Phi}_n = \Phi_n(\vec{r}, N_0)$, where N_0 is the average number of atoms per site. This approximation is valid since the dependence of K on the absolute (N_n) and relative ($N_n - N_{n+1}$) atom number is very weak.

For an experimental setup with a horizontally oriented waveguide only the weak longitudinal trapping is of relevance for the on-site energies and thus

$$\epsilon_n = \int d\vec{r}\, \Phi_n V_{\mathrm{ext}} \Phi_n = 1/2 m\omega_{\|}^2 (n \cdot d)^2. \tag{4.30}$$

The chemical potential is given by

$$\begin{aligned} \mu_n^{\mathrm{loc}} &= \mu_n^{\mathrm{kin}} + \mu_n^{\mathrm{pot}} + \mu_n^{\mathrm{int}} \\ &= \int d\vec{r} \left[\frac{\hbar^2}{2m} (\vec{\nabla}\Phi_n)^2 + V_{\mathrm{ext}}(\vec{r})\Phi_n^2 + g_0 |\psi_n(t)|^2 \Phi_n^4 \right]. \end{aligned} \tag{4.31}$$

The tunneling energy K must be calculated via the width of the lowest Bloch band or using Wannier functions in the longitudinal direction (see previous section 4.2.2). As in the case of the DNLS, the integration in transverse direction can be neglected.

For the calculation of the local chemical potential μ_n^{loc} the local wave function $\Phi_n(\vec{r}, N_n(t))$ must be chosen according to the experimental situation. In the experiments described in this chapter the transverse trapping frequency $\omega_\perp = 2\pi \cdot 230$ Hz and the longitudinal trapping frequency in a single well is given by $\omega_{\mathrm{latt}} = 2\sqrt{s}\,\omega_{\mathrm{r}} \sim 2\pi \cdot 25$ kHz. With a local average number of atoms of $N_{av} \sim 100$, a local interaction potential $\mu^{\mathrm{int}}/\hbar \sim 2\pi \cdot 1$ kHz is obtained from a variational calculation (Baym/Pethick, 1996). Thus $\hbar\omega_{\mathrm{latt}} \gg \mu^{\mathrm{int}} > \hbar\omega_\perp$ and the system can be described as a horizontal pile of pancakes. A single condensate can be approximated by the product state

$$\Phi_n\Big(\vec{r}, N_n(t)\Big) \simeq \phi_{\mathrm{G},n}(x - x_n) \cdot \phi_{\mathrm{TF},n}\Big(\vec{R}, N_n(t)\Big), \tag{4.32}$$

with a Gaussian shape in axial direction

$$\phi_{\mathrm{G},n}(x - x_n) = (\sigma_{\mathrm{latt}}\sqrt{\pi})^{-1/2} e^{-(x-x_n)^2/2\sigma_{\mathrm{latt}}^2}, \tag{4.33}$$

with $\sigma_x = \sqrt{\hbar/m\omega_{\mathrm{latt}}}$ and a parabolic shape in radial direction

$$\phi_{\mathrm{TF},n}\Big(\vec{R}, N_n(t)\Big) = \Big(\frac{\mu_n^{\mathrm{TF}} - \frac{m}{2}\omega_\perp^2 \vec{R}^{\,2}}{\tilde{g}_0 N_n(t)}\Big)^{1/2}, \tag{4.34}$$

with $\tilde{g}_0 = g_0/(\sqrt{2\pi}\sigma_{\mathrm{latt}})$ (Thomas–Fermi approximation). In this approximation the local chemical potential, i.e the additional energy due to the atomic interaction, which is relevant for the dynamics, is given by

$$\mu_n^{\mathrm{loc}} = \mu_n^{\mathrm{TF}} = \int d\vec{r} \left[\frac{m}{2}\omega_\perp^2 \vec{R}^{\,2} \phi_{\mathrm{TF},n}^2 + g_0 |\psi_n(t)|^2 |\phi_{\mathrm{TF}}^{(n)}|^4 \right]. \tag{4.35}$$

and yields

$$\mu_n^{\mathrm{loc}} = \left(\frac{m\omega_\perp^2 g_0}{\sqrt{2\pi}\pi\sigma_{\mathrm{latt}}} \right)^{1/2} N_n^{1/2}. \tag{4.36}$$

The constant contributions, which do not depend on the atom number are neglected. The nonlinearity in the DNL can therefore be written as $\mu_n^{\mathrm{loc}} = U_1|\psi_n(t)|$ (Smerzi, 2003) with

$$U_1 = \sqrt{\frac{m\omega_\perp^2 g_0}{\sqrt{2\pi}\pi\sigma_{\mathrm{latt}}}} \tag{4.37}$$

Effective dimensionality
Generally the nonlinearity in the DNL can be written as

$$\mu_n^{\mathrm{loc}} = U_\alpha|\psi_n(t)|^\alpha, \quad \alpha = \frac{4}{2+D}, \tag{4.38}$$

where $D = 0, 1, 2, 3$ is the effective dimensionality of the system according to

$$D = \begin{cases} 0 & \text{if } \hbar\omega_a, \hbar\omega_b, \hbar\omega_c \gg \mu^{\mathrm{int}} \text{ (spherical)} \\ 1 & \text{if } \hbar\omega_a, \hbar\omega_b \gg \mu^{\mathrm{int}} \gg \hbar\omega_c \text{ (cigar)} \\ 2 & \text{if } \hbar\omega_a \gg \mu^{\mathrm{int}} \gg \hbar\omega_b, \hbar\omega_c \text{ (pancake)} \\ 3 & \text{if } \mu^{\mathrm{int}} \gg \hbar\omega_a, \hbar\omega_b, \hbar\omega_c \text{ (spherical)} \end{cases} \tag{4.39}$$

Note that for $D = 0$ the DNL reduces to the 1D discrete nonlinear Schrödinger equation DNLS with $\mu_n^{\mathrm{loc}} = U_2|\psi_n(t)|^2$.

Therefore Bose-Einstein condensates in a 1D lattice potential constitute a model system, which allows to investigate experimentally nonlinear wave propagation with different nonlinearities. In this work the cases for $D = 0$ and $D = 2$ are investigated numerically and compared with the experimental data.

4.2.4 Numerical implementation

Both the DNLS and the DNL can be implemented and solved numerically very easily. In this work an explicit Runge-Kutta (4,5) solver scheme (from the Matlab© package) is used to integrate the dynamical equations. The dynamic equation is written in vector form

$$|\dot{\psi_n}\rangle = \mathbf{M}|\psi_n\rangle + \Lambda|\psi_n\rangle\langle\psi_n| \cdot |\psi_n\rangle \tag{4.40}$$

and solved directly. Care must be taken to implement eq. (4.40) with sparse matrices or using the complete product, since most of the matrix elements of $\mathbf{M}$ are zero. For a typical longitudinal wave packet width between 10 and 100 μm only about 500 lattice points are needed. Thus the calculation is extremely ”low cost” and results can be obtained in a very short time. An example Matlab© program is given in Appendix A.6.

4.3 Theoretical Investigation of nonlinear self-trapping in lattice potentials

In this section the dynamics of expanding wave packets in deep 1D lattice potentials is investigated both analytically and numerically. For this purpose the results provided by the non-polynomial nonlinear Schrödinger equation (NPSE) and the discrete nonlinear Schrödinger equation (DNLS and DNL) are investigated. The effect of nonlinear self-trapping for atomic wave packets with repulsive interaction is analyzed in detail.

In the first part the global dynamics is investigated in terms of a variational solution of the DNLS (Trombettoni, 2001). The solution shows that the global dynamics of wave packets can be divided into two regimes, the diffusive and the self-trapping regime. The dynamics in the diffusive regime is characterized by a continuous expansion of the wave packet. In the self-trapping regime, after an initial expansion, the wave packet stops to expand and remains localized. The transition between both regimes is governed by a critical parameter, which can be identified by the ratio between the mean local interaction energy and the tunneling energy. In addition the situation in momentum space is investigated in more detail by numerically integrating the NPSE. In the self-trapping regime the initial wave packet expansion stops, once the Brillouin zone edges in quasi momentum space are populated. The further self-trapping dynamics can be interpreted as interaction-induced Bloch oscillations.

In the second part the local tunneling dynamics in the self-trapping regime is investigated by numerically integrating the DNL. The results show that the effect of self-trapping is of *local* nature and is due to the inhibited site-to-site tunneling at the edges of the wave packet. During the initial expansion the wave packets develop steep edges and thus large density gradients at the wave packet edges. These correspond to large differences of the interaction energy in adjacent lattice wells. Consequently the site-to-site tunneling at the edges of the wave packet is strongly suppressed and shows a dynamics, which is very similar to the “running-phase” and the “π-phase” macroscopic self-trapping modes known from the corresponding double well BJJ.

In section 4.3.3 the decay of self-trapped wave packets is investigated numerically. The results show that the self-trapping tunneling dynamics at the wave packet edges decays in time. This can be understood, since a single lattice well is coupled to two next neighbors, in contrast to the corresponding double well system. In this sense the transition between the diffusive and the self-trapping regime must be understood as a fast increase of the time, during which the wave packet remains localized. The critical parameter and the dimensionality of the system are identified as important parameters, that govern the decay.

The universal scaling behavior, which is obtained from the variational solution of the DNLS is described in section 4.3.4. The ratio between the initial width and the final width of the wave packet is shown to depend universally on the critical parameter.

4.3.1 Global picture of nonlinear self-trapping dynamics

Gaussian variational ansatz

To study the dynamical evolution of an atomic wave packet in a system, which is governed by the 1D discrete nonlinear Schrödinger equation, a variational ansatz is used in

(Trombettoni, 2001). The wave packet is described by a complex Gaussian profile

$$\psi_{\mathrm{G},n} = \sqrt{k} \cdot \exp\Big(- \frac{(n-\xi)^2}{\gamma^2} + ip(n-\xi) + i\frac{\delta}{2}(n-\xi)^2 \Big), \tag{4.41}$$

where $\xi(t)$ and $\gamma(t)$ are the center and the width of the density $\rho_n = |\psi_{\mathrm{G},n}|^2$ in lattice units. $p(t)$ and $\delta(t)$ are the associated momenta in units of inverse lattice units. k is a normalization constant. $\delta(t)$ describes the slope of the quadratic phase in real space, and thus determines the width of the wave function in momentum space. From the DNLS (4.19), together with the above ansatz (4.41) a variational principle (Lagrangian optimization) yields the coupled dynamic equations of the profile parameters

$$\begin{aligned} \dot{p} &= 0 \\ \dot{\xi} &= \sin(p)e^{-\eta} \\ \dot{\delta} &= \cos(p)(\frac{4}{\gamma^4} - \delta^2)e^{-\eta} + \frac{2\Lambda}{\sqrt{\pi}\gamma^3} \\ \dot{\gamma} &= \gamma\delta\cos(p)e^{-\eta}, \end{aligned} \tag{4.42}$$

where $\eta = (2\gamma^2)^{-1} + \gamma^2\delta^2/8$. Here a horizontally oriented lattice and waveguide are assumed. The weak axial trapping potential is neglected. Therefore the on-site energies ϵ_n, which are constant throughout the lattice, do not alter the dynamics. From the dynamical equations the effective Hamiltonian

$$H = \frac{\Lambda}{2\sqrt{\pi}\gamma} - \cos(p)e^{-\eta} \tag{4.43}$$

can be derived, which determines the character of the wave packet dynamics.

If the system is initially in the region of positive effective mass[2] $\cos(p_0) > 0$, then the critical nonlinearity $\Lambda_\mathrm{c} = 2\sqrt{\pi}\gamma_0\cos(p_0)e^{-1/2\gamma_0^2}$ is determined by $H = 0$ (Trombettoni, 2001). By increasing the nonlinearity Λ above the critical value Λ_c, the system moves from the diffusive regime to the self-trapping regime. The dynamics in the diffusive regime is characterized by a continuous expansion of the wave packet. In the self-trapping regime, after an initial expansion, the wave packet stops to expand and remains localized. The dynamics in the two regimes is depicted in figure 4.6.

In the region of negative effective mass $\cos(p_0) < 0$ the critical value, is determined by $H > |\cos(p_0)|$, and thus $\Lambda_\mathrm{c} = 2\sqrt{\pi}\,\gamma_0|\cos(p_0)|\,(1 - e^{-1/2\gamma_0^2})$.

The solution of the DNLS with a variational ansatz allows to identify the relevant physical quantities of nonlinear self-trapping. In the positive mass regime it predicts self-trapping for $\Lambda/\Lambda_\mathrm{c} > 1$ with

$$\frac{\Lambda}{\Lambda_\mathrm{c}} = \frac{g_0 N_\mathrm{T}}{2K} \int d\vec{r}\,\Phi_n^4 \cdot \frac{1}{2\sqrt{\pi}\gamma_0\cos(p_0)} e^{1/2\gamma_0^2} \sim \frac{\langle\mu_\mathrm{loc}^\mathrm{int}\rangle}{E_\mathrm{bw}}. \tag{4.44}$$

By identifying $\Lambda/\Lambda_\mathrm{c}$ with the ratio between the mean local interaction energy $\langle\mu_\mathrm{loc}^\mathrm{int}\rangle$ and the width of the lowest Bloch band E_bw, it becomes clear that the self-trapping regime can be reached by reducing the width of the lowest Bloch band of the lattice potential, i.e. by increasing the lattice potential depth. Alternatively the mean local interaction

---

[2] In the tight binding approximation the lattice dispersion relation is given by $E(p) = -\frac{E_0}{2}\cos p$.

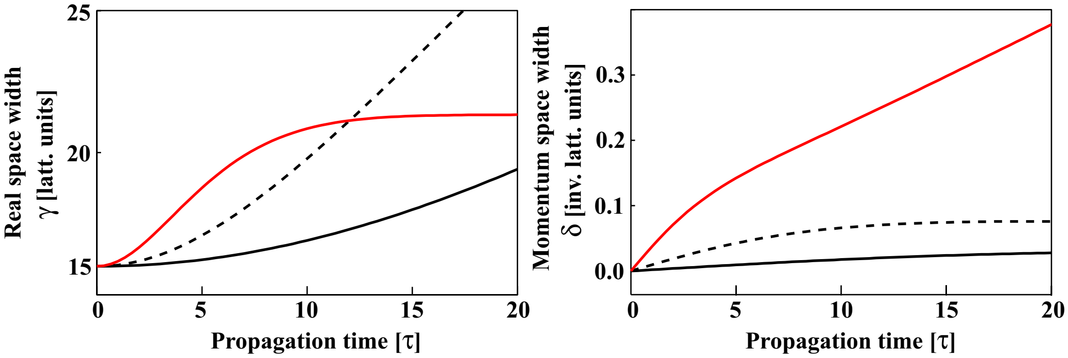

Figure 4.6: Dynamics of a wave packet in the diffusive and in the self-trapping regime obtained from the numerical integration of the coupled dynamical equations (4.42). The temporal evolution of the width $\gamma(t)$ in real space (left graph) and the width $\delta(t)$ in momentum space (right graph) are shown, with $\Lambda/\Lambda_c = 0.1$ (black line), $\Lambda/\Lambda_c = 1$ (dashed line) and $\Lambda/\Lambda_c = 4$ (red line). The time is given in units of $\tau = \hbar/2K$. Increasing the nonlinearity results in a faster initial expansion in real space. Above the critical value the initial expansion quickly stops and the wave packet remains localized without any external potential - hence the name self-trapping. In momentum space, in contrast, the width constantly increases in the self-trapping regime.

energy $\langle \mu_{\text{loc}}^{\text{int}} \rangle$ can be increased by either increasing the total number of atoms or by decreasing the initial wave packet width.

In addition the set of dynamical equations (4.42) shows that the self-trapping dynamics in real space is inversely correlated with the dynamics in momentum space. In the diffusive regime the wave packet width in real space increases constantly, while the width in momentum space stops to increase once the atomic density and therefore the nonlinear energy goes to zero. In the self-trapping regime, in contrast, the wave packet remains localized and the width in momentum space increases constantly due to the atomic interaction. This relation is depicted in figure 4.6.

Numerical integration of the NPSE

The relationship between the self-trapping dynamics in real space and the corresponding expansion dynamics in momentum space is investigated more closely by numerically integrating the effective 1D nonlinear Schrödinger equation

$$\begin{aligned} i\hbar\frac{\partial}{\partial t}A(x,t) &= \left[E(k) + \alpha_{\text{nl}}(q_0, V_0) g_{1\text{D}} N \frac{|A(x,t)|^2}{\sqrt{1+2a_s N|A(x,t)|^2}}\right] A(x,t) \\ &+ \left[\frac{\hbar\omega_\perp}{2}\left(\frac{1}{\sqrt{1+2a_s N|A(x,t)|^2}} + \sqrt{1+2a_s N|A(x,t)|^2}\right)\right] A(x,t) \end{aligned} \tag{4.45}$$

for the wave packet envelope $A(x,t)$. This dynamical equation is a combination of the 1D non-polynomial nonlinear Schrödinger equation (2.13) and the envelope equation (3.10). In contrast to eq. (3.10), here the effect of the lattice potential is included using the complete dispersion relation $E(k)$.

The numerical results for the expansion of a wave packet in the self-trapping regime are shown in figure 4.7. The density distributions both in real and in momentum space

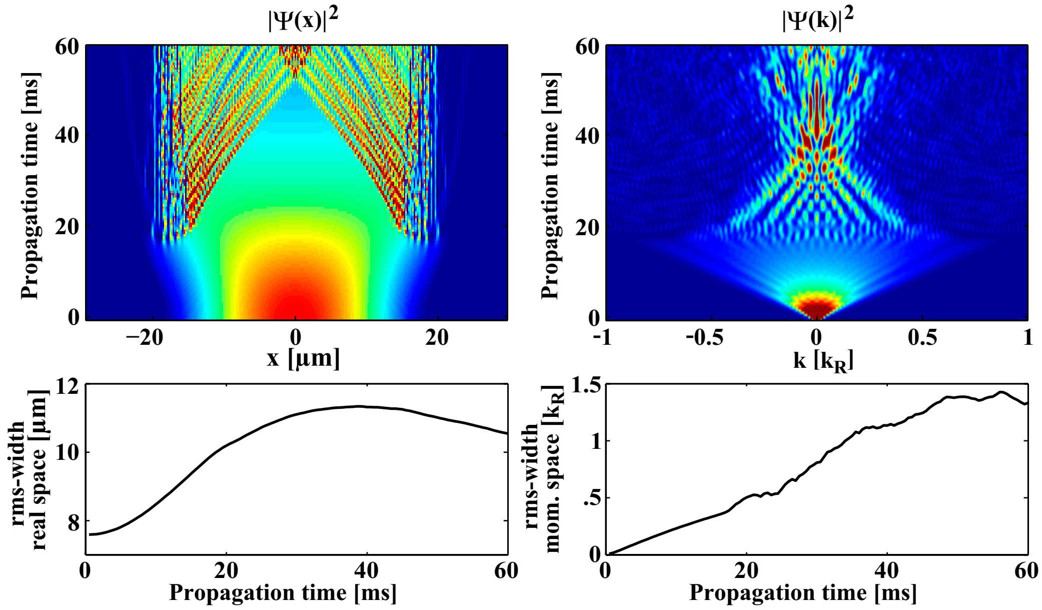

Figure 4.7: Wave packet dynamics in the self-trapping regime obtained from a numerical integration of eq.(4.45). The evolution of the density in real space (upper left graph) and in momentum space (upper right graph) is shown for a wave packet with $N_{\mathrm{T}} = 5000$, initial width $\sigma_0 = 7.6\,\mu\mathrm{m}$, $U_{\mathrm{latt}} = 11\ \mathrm{E_r}$ and $\omega_\perp = 2\pi \cdot 230$ Hz. The initial expansion in real space (lower left graph) stops at $t \sim 20$ ms. This coincides with a population of the Brillouin zone edge due to the expansion in momentum space. The further evolution of $|\Psi(x,t)|^2$ suggests that the atomic population moving outwards is reflected at the steep edges of the wave packet, i.e. reverses its velocity and moves inwards again. In this sense the effect of self-trapping is a consequence of the steep wave packet edges, which act as hard reflecting walls.

initially expand quickly due to the repulsive atomic interaction. While $|\Psi(k,t)|^2$ continues to expand (here the dynamics is reduced to a single Brillouin zone), $|\Psi(x,t)|^2$ stops to expand at $t \sim 20$ ms. At that time the density distribution develops sharp peaks at the edge of the wave packet, which coincides with a population of the Brillouin zone edge in momentum space. The further evolution of $|\Psi(x,t)|^2$ suggests that the steep wave packet edges act as a hard wall, which reflects the atomic population moving outwards back towards the center of the wave packet.

This behavior can be understood considering the dynamics in a periodic potential by means of the Bloch function description (see section 3.1.1). The atomic population at the edge of the wave packet is quickly accelerated across the Brillouin zone edge due to the repulsive atomic interaction. The corresponding group velocity changes its sign such that the atomic population moves back towards the center of the wave packet. This dynamics is closely related to the gravity induced Bloch oscillations (Anderson *et al.*, 1998), with the difference that here the Bloch oscillations are induced by the nonlinear atom-atom interaction.

Discussion

The results from the variational solution of the DNLS and the numerical investigation of the modified Gross-Pitaevskii equation provide the following global picture of nonlinear self-trapping. The self-trapping regime is entered, if the initial nonlinear energy is sufficient to populate the Brillouin zone edge during the initial expansion. This is described by the critical parameter $\frac{\Lambda}{\Lambda_c} \sim \frac{\langle \mu_{\mathrm{loc}}^{\mathrm{int}} \rangle}{E_{\mathrm{bw}}} > 1$, which governs the transition from the diffusive to the self-trapping regime.

Note that during the evolution the wave packet shape, both in real and in momentum space is altered significantly with respect to the initial parabolic/Gaussian[3] shape. This complex dynamics cannot be described in a global picture and, as is shown in the following, is governed by the local site-to-site tunneling dynamics.

4.3.2 Local tunneling picture of nonlinear self-trapping dynamics

In this section the effect of nonlinear self-trapping is investigated by numerically solving the 1D discrete nonlinear Schrödinger equation. In this equation the dynamics is reduced to the fundamental processes in the system, namely the tunneling between adjacent lattice sites and the nonlinear phase evolution due to the interaction of the atoms.

Numerical integration of the DNL

In figure 4.8 the temporal shape evolution of an atomic wave packet in the self-trapping regime is shown, which is obtained from a numerical integration of the DNL[4] (4.28). The characteristic shape dynamics in the self-trapping regime is described by a fast initial expansion, during which the shape changes from the initial Gaussian/parabolic to a more rectangular shape with steep edges. In the following strong side peaks appear which then decay towards the center of the wave packet, while the edges do not move. The internal dynamics shows a wave dynamics with multiple interferences, with the edges acting as reflecting walls.

The numerical investigation of the nonlinear self-trapping dynamics with the help of a discrete nonlinear Schrödinger equation allows to take a closer look at the local site-to-site dynamics. In analogy to the double well problem (see section 4.1.2), we chose to investigate the dynamics of the relative atom number difference $\Delta N_j = (N_{j+1} - N_j)/(N_{j+1} + N_j)$ and the phase difference $\Delta\phi_j = \phi_{j+1} - \phi_j$ between two adjacent sites.

Considering the different tunneling modes in a double well BJJ, the first quantity to investigate is the time average $\overline{\Delta N_j} = 1/T \int dt\, \Delta N_j$, which is plotted in figure 4.9(b) for the system considered in figure 4.8 and a total propagation time $T = 50$ ms. Clearly two different regions can be distinguished, the edge region (orange) with $\overline{\Delta N_j} \neq 0$ and the central region (yellow) with $\overline{\Delta N_j} \sim 0$. In figure 4.9(c) a representative example of the site-to-site dynamics in the central region is shown. Both the relative atom number difference as well as the phase difference oscillate around zero with a mutual temporal phase difference of $\pi/2$. This dynamics corresponds to the double well Boson-Josephson junction "zero-phase mode“ (see section 4.1.2, figure 4.3(b)). It is characteristic for superfluid tunneling dynamics (Cataliotti *et al.*, 2001).

---

[3] In the simulation a numerically obtained ground state is used.

[4] The findings of this section can equally be obtained by integrating the DNLS.

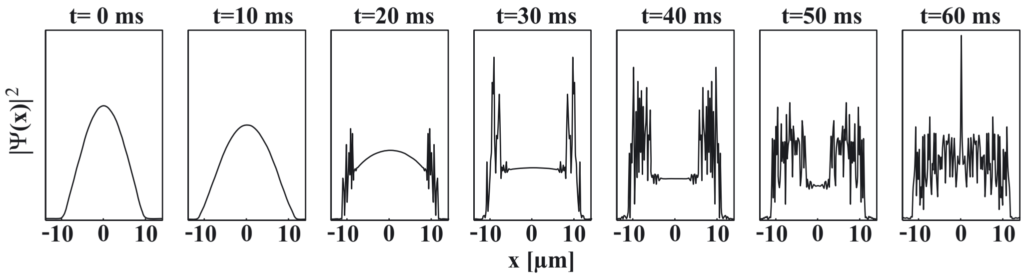

Figure 4.8: Temporal shape evolution of a wave packet in the self-trapping regime with $N_\mathrm{T} = 5000$, initial width $\sigma_0 = 7.6\,\mu$m rms, $\mathrm{U_{latt}} = 10\ \mathrm{E_r}$ and $\omega_\perp = 2\pi \cdot 230$ Hz. The dynamics is split into an initial expansion, during which the shape develops a rectangular shape with steep edges (0∼ 20 ms), and a subsequent dynamics, which is characterized by fixed steep edges and a complex internal wave dynamics with the edges acting as reflecting barriers. The shape evolution suggests a qualitatively different local dynamics at the edges compared to the central wave packet region.

A representative example of the dynamics in the outermost edge region is shown in figure 4.9(d). Here the characteristic initial phase dynamics in the self-trapping regime can be seen clearly. The atomic interaction accelerates the atomic population at the edge of the wave packet to the Brillouin zone edge, which corresponds to a phase difference of $|\Delta\phi_j| = \pi$. The phase difference then locks to a value $|\Delta\phi_j| \sim \pi$, while the dynamics of ΔN_j shows small amplitude oscillations. The corresponding tunneling modes in the double well BJJ are the ”π-phase macroscopic quantum self-trapping modes“ (see figure 4.3(g) and (h)). The value of the double well BJJ nonlinearity Λ, for which these modes occur, is given by $\Lambda_\mathrm{c} < \Lambda < 2 \cdot \Lambda_\mathrm{s}$. In a typical wave packet $\max\{\Delta N_j\} < 0.8$ and therefore $\max\{\Lambda_\mathrm{s}\} = \max\{1/\sqrt{1-(\Delta N_j)^2}\} \sim 2$. In the self-trapping regime $\langle\mu_\mathrm{loc}^\mathrm{int}\rangle/E_\mathrm{bw} > 1$ (see eq. (4.44)) and consequently

$$\Lambda \sim 2 \cdot \langle N_\mathrm{loc}\rangle\, U/(2K) = 4 \cdot \langle\mu_\mathrm{loc}^\mathrm{int}\rangle/E_\mathrm{bw} > 4, \tag{4.46}$$

where $\langle N_\mathrm{loc}\rangle$ is the average number of atoms in a single well. From this estimate we obtain that these tunneling modes are only possible at the outermost edge, where the number of atoms in a single site $N_j < \langle N_\mathrm{loc}\rangle$.

The typical tunneling dynamics in the edge region is shown in figure 4.9(e). During the initial expansion $|\Delta\phi_j|$ increases to a value close to π while at the same time ΔN_j increases due to the formation of a steep edge. Once a critical value is reached, the self-trapping tunneling dynamics sets in, which is characterized by $|\Delta N_j| \sim 1$ and a phase difference, that continuously winds up. The corresponding tunneling mode in the double well BJJ is the ”running phase macroscopic quantum self-trapping“ mode (see figure 4.3(i)).

Discussion

The the critical ratio $\langle\mu_\mathrm{loc}^\mathrm{int}\rangle/E_\mathrm{bw} > 1$ for nonlinear self-trapping, which is obtained from an investigation of the global self-trapping dynamics, predicts also the underlying local self-trapping tunneling dynamics at the edge of the wave packet, where the “running-phase MQST” tunneling mode will dominate. Only at the outermost edge of the wave

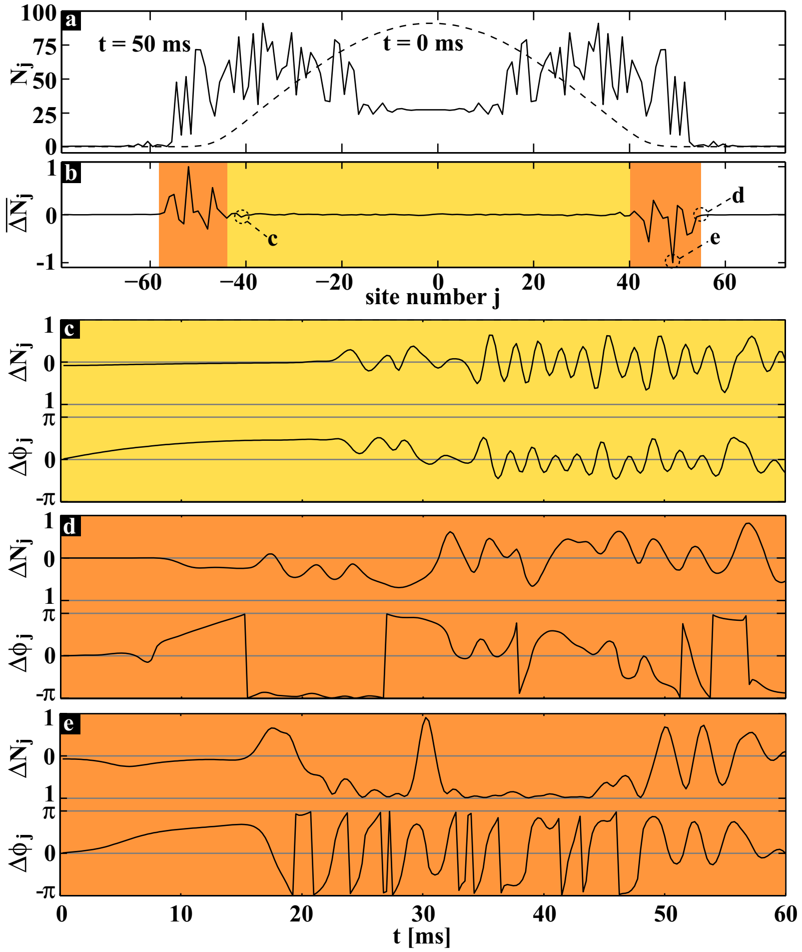

Figure 4.9: Numerical investigation of the local self-trapping dynamics of the system considered in figure 4.8. **(a)** Wave packet shape for $t = 0$ and $t = 50$ ms. **(b)** Time average $\overline{\Delta N_j}$ of the relative atom number difference. Clearly a central region with $\overline{\Delta N_j} \sim 0$ (yellow) and an edge region with $\overline{\Delta N_j} \neq 0$ (orange) can be distinguished. **(c)** The dynamics in the central region is described by a small amplitude oscillation of both ΔN_j and $\Delta\phi_j$ with a mutual temporal phase difference of $\pi/2$, characteristic for superfluid tunneling. This dynamics corresponds to the "zero-phase" tunneling mode in a double well BJJ. **(d)** In the outermost edge region with small absolute atom number self-trapping tunneling dynamics is possible, which corresponds to the "π-phase self-trapping" mode in the double well BJJ. It is described by long periods with $|\Delta\phi_j| \sim \pi$ and small amplitude oscillations of ΔN_j. **(e)** Typical self-trapping dynamics in the edge region characterized by long periods with $|\Delta N_j| \sim 1$, while the phase difference winds up quickly ($\Delta\phi_j$ is plotted modulo π). In the double well BJJ the "running-phase self-trapping mode" is the corresponding tunneling mode.

packet, where $N_j < \langle N_{\mathrm{loc}} \rangle$ and therefore $\Lambda_{\mathrm{c}} < \Lambda < 2 \cdot \Lambda_{\mathrm{s}}$, the "$\pi$-phase MQST modes" will occur.

In the center of the wave packet the numerical investigation shows that the phase difference does not exceed $\Delta\phi_j = \pi/2$. Consequently the critical value Λ_{c} is much larger in comparison to the edge region. We will therefore find a tunneling dynamics in the center of the wave packet, which allows the transport of atoms.

4.3.3 Temporal decay of self-trapped wave packets

The investigation in the previous section showed that self-trapping tunneling modes dominate the local tunneling dynamics in the edge region. But since a single well is coupled to two adjacent neighbors, the self-trapping tunneling modes between two sites will eventually decay in the course of time. As a result the wave packets in the self-trapping regime will continue to expand.

In this section the dependence of this decay on the different system parameters is investigated. The most important parameter is the nonlinear parameter Λ. In figure 4.10 the numerically obtained temporal evolution of the wave packet width is shown for different wave packets. The nonlinearity Λ is varied by increasing the atom number. For small nonlinearities the effect of self-trapping reduces to a temporal "slowing down" of the expansion, after which the effect of self-trapping decays and the wave packet continues to expand. With increasing nonlinearity the time during which the wave packet remains localized quickly increases. In this sense it is important to note that the transition between the diffusive and the self-trapping regime must be understood as a fast increase of the time, during which the wave packet remains localized.

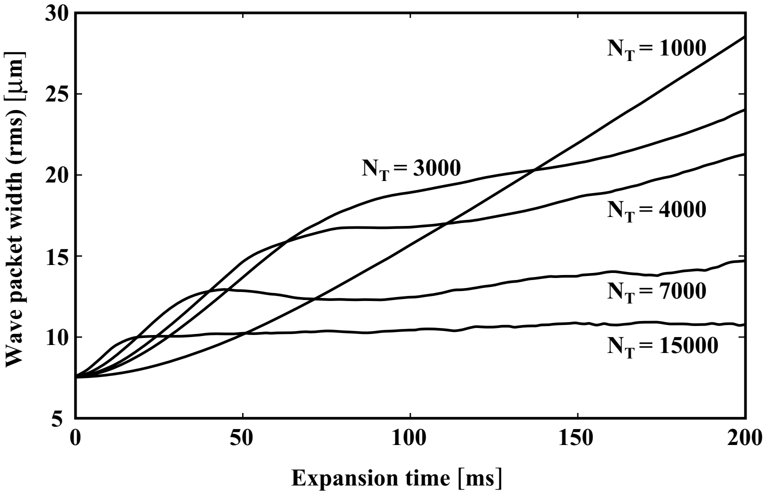

Figure 4.10: Temporal evolution of the wave packet width obtained by numerically integrating the DNL for the system considered in figure 4.8. Here the initial wave packet shape is Gaussian and the nonlinearity Λ is varied by choosing N_T =1000, 3000, 4000, 7000 and 15000. In the self-trapping regime the initial expansion is stopped temporarily and then the wave packet continues to expand. With increasing Λ the decay time quickly increases.

The numerical investigation of the decay of self-trapping with respect to the initial shape of the wave packet shows small differences for initially Gaussian and parabolic wave packets. A strong dependence could not be found.

The dimensionality of the system, i.e. wether it is described by the purely 1D DNLS or by the effective 1D DNL, on the other hand, does have a strong influence on the nature of the decay of self-trapping. This difference becomes clear only in the deep

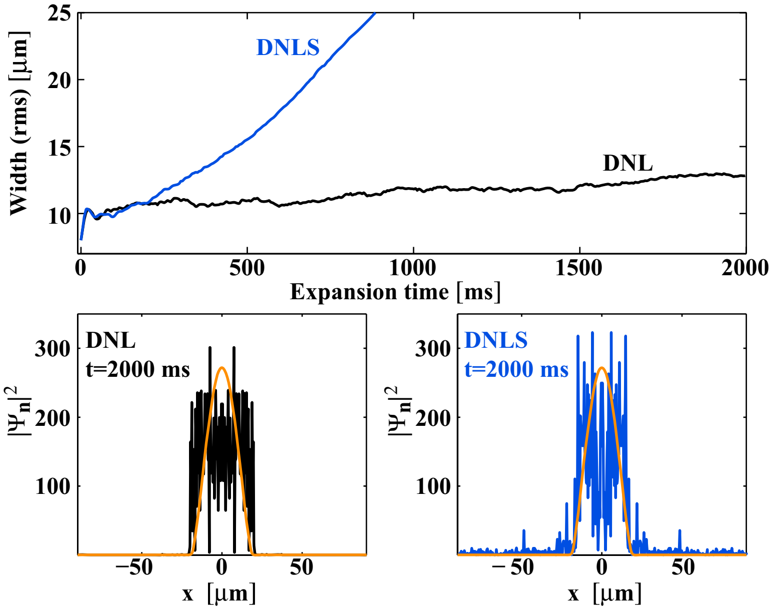

Figure 4.11: Decay of self-trapping in a system governed by the DNL and the DNLS. In the upper graph the temporal evolution of the wave packet width obtained from an integration of the DNL and the DNLS is shown. In the DNLS system self-trapping decays at $t \sim 100$ ms and the wave packet starts to expand with increasing velocity. In the DNL system, in contrast, the decay is described by a slow and steady expansion. The different nature of the breakdown is depicted in the lower graphs. In the DNLS system the steep edges break up during the evolution, which allows the whole packet to expand. In the DNL system, in contrast, the approximately square wave packet shape remains.

self-trapping regime. In figure 4.11 the expansion dynamics of a wave packet in the deep self-trapping regime is shown, which is obtained by numerically integrating the DNL and the DNLS. In both cases an initially parabolic[5] wave packet with total number of atoms $N_{\mathrm{T}} = 15000$ and an initial width of $7.6\,\mu$m rms is used. In order to compare the decay for both cases, a transverse trapping frequency of $\omega_\perp = 2\pi \cdot 230$ Hz and $\omega_\perp = 2\pi \cdot 53$ Hz is used for the integration of the DNL and the DNLS, respectively. For these parameters the initial mean atomic density is similar for both cases and the initial trapping occurs for both cases at $t \sim 10$ ms with a width of $\sim 10\,\mu$m.

In both systems the width remains approximately constant for $\Delta t \sim 100$ ms. In the following the wave packet in the DNLS system starts to expand with increasing velocity. In the DNL system, in contrast, a slow and steady expansion is observed. The different behavior results from the different nature of the decay of self-trapping. In the DNLS system the steep edges, which provide the necessary density gradient for the self-trapping modes, decay during the evolution and thus allow the whole wave packet to expand (see figure 4.11 lower right graph). For the DNL system the situation is different. Here the square wave packet shape remains during the evolution with the steep edges "conquering" one site at a time.

---

[5] Numerically obtained ground state of the initial harmonic trapping potential.

Discussion

The above results can be understood considering the different nonlinearities $U_1/2K \cdot \sqrt{N_j}$ and $U_2/2K \cdot N_j$, that determine the DNL and the DNLS, respectively (see eq. (4.37) and (4.26)). In figure 4.12 the nonlinearities and their gradients with respect to the local atom number N_j are plotted for the system considered in figure 4.11.

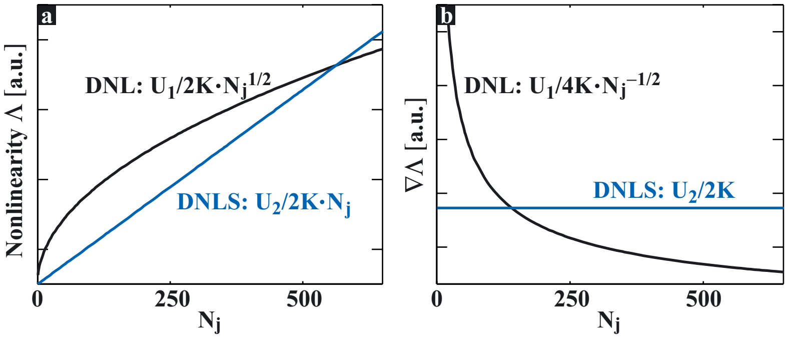

Figure 4.12: Nonlinearity and the corresponding gradient versus the local atom number N_j in the DNL and the DNLS system. In the wave packet edge region with small local atom numbers, the gradient of the nonlinearity and therefore the differences in the nonlinear energy in adjacent sites is much larger in the DNL compared to the DNLS. Consequently, self-trapping dynamics is favored by the DNL in this region.

The nonlinearity in the DNL system depends on the square root of the local atom number and therefore the gradient of the nonlinear energy for small atom numbers is larger in comparison to the DNLS system. At the edge of the wave packet, with small average atom numbers, large differences in the nonlinear energy and thus self-trapping dynamics is favored by the DNL system.

But since for small atom numbers the approximations, entering the derivation of the DNL, are not valid, questions concerning the applicability arise and are discussed together with the experimental results on the decay of self-trapping in section 4.4.3.

4.3.4 Scaling behavior of self-trapped wave packets

In addition to the critical parameter Λ_c for self-trapping, the variational solution of the DNLS yields an information about the final width γ_∞ of the wave packet. From the effective Hamiltonian $H = \Lambda/(2\sqrt{\pi}\gamma_0) - \cos(p_0)e^{-\eta}$ we obtain the final width $\gamma_\infty = \Lambda/(2\sqrt{\pi}H_0)$, since in the self-trapping regime $H_0 > 1$ and thus $\delta \to \infty$ for $t \to \infty$. Together with the critical parameter $\Lambda_c = 2\sqrt{\pi}\gamma_0 \cos(p_0)e^{-\eta}$ we obtain the universal ratio between the initial and the final width (Trombettoni, 2001)

$$\frac{\gamma_0}{\gamma_\infty} = 1 - \frac{\Lambda_c}{\Lambda} \text{ (DNLS).} \tag{4.47}$$

Following the same lines of calculation as in (Trombettoni, 2001) the corresponding result is obtained for the DNL (Trombettoni, priv.comm) with $\Lambda_c = 2.057\sqrt{\gamma_0}\cos(p_0)$ and

$$\frac{\gamma_0}{\gamma_\infty} = \left(1 - \frac{\Lambda_c}{\Lambda}\right)^2 \text{ (DNL).} \tag{4.48}$$

The universal ratio tells us that the dynamics of the wave packet width is solely determined by two global parameters, the initial density of the atoms and the depth of the periodic potential.

Please note that for the DNLS system $\Lambda/\Lambda_{\mathrm{c}} = g_0 N_{av} \int d\vec{r}\,\phi^4/2K \cdot 1/\sqrt{\pi} = \Lambda_{av}/\sqrt{\pi}$ and for the DNL system $\Lambda/\Lambda_{\mathrm{c}} = U_1\sqrt{N_{av}}/2K \cdot 1/\sqrt{2} = \Lambda_{av}/\sqrt{2}$, where $N_{av} = N_{\mathrm{T}}/2\gamma_0$ is the average local number of atoms, $\Lambda_{av} = \langle\mu_{\mathrm{loc}}^{\mathrm{int}}\rangle/2K$ is the average nonlinear parameter and $\langle\mu_{\mathrm{loc}}^{\mathrm{int}}\rangle$ is the average local interaction energy.

In order to compare the results for the DNLS and the DNL, the ratio γ_0/γ_∞ is plotted versus Λ_{av} in figure 4.13.

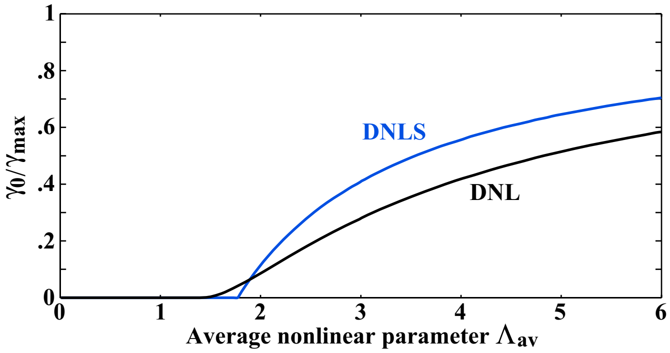

Figure 4.13: Scaling behavior of the effect of self-trapping. The variational results for the ratio between the initial and the final wave packet width are plotted versus the average nonlinear parameter for the DNLS and the DNL system. In both cases the ratio shows the critical behavior and depicts the nature of self-trapping: increasing the nonlinear parameter Λ (by, e.g., increasing the atom number) leads to a faster trapping and consequently to a smaller final width.

In both cases a critical behavior results, since for Λ_{av} below the critical value $\gamma_0/\gamma_\infty = 0$ with $\gamma_\infty \to \infty$ and above the critical value $\gamma_0/\gamma_\infty > 0$ with a finite value for γ_∞. With increasing Λ_{av} the ratio $\gamma_0/\gamma_\infty \to 1$ for both the DNLS and the DNL system. The differences between both models are discussed together with the experimental data on the scaling behavior in section 4.4.4.

4.4 Experimental observation of nonlinear self-trapping

In this section I report on the first experimental observation of nonlinear self-trapping. We observed the effect in real space by looking at the expansion dynamics of ^{87}Rb Bose-Einstein condensates in a deep 1D lattice potential.

In section 4.4.1 the relevant details of the experimental setup and the image analysis procedure are described.

In section 4.4.2 the experimental realization of the transition from the diffusive to the self-trapping regime is presented. By increasing the atom number of wave packets with otherwise identical parameters, we move the system from the diffusive regime, characterized by a continuous expansion of the wave packets, to the nonlinearity dominated self-trapping regime, where the initial expansion stops and the width of the wave packets remains finite. The detailed analysis of the shape dynamics in the self-trapping regime shows the theoretically predicted evolution from the Gaussian wave form to a rectangular wave form with steep density gradients at the wave packet edges.

In section 4.4.3 the decay of self-trapped wave packets is analyzed. In the experimental system additional dynamical effects, that are not included in the system described by the DNL/DNLS, such as transverse excitations, decoherence and heating, can affect the decay of self-trapping. In order to distinguish between these effects, a discrete non-polynomial Schrödinger equation (DNPSE) is developed by modifying the nonlinearity in the DNL, such that it correctly describes the relevant chemical potential both in the regime of small and in the regime of high atomic density. The comparison of the experimental data with the numerical results of the DNPSE shows unambiguously that the observed decay is *not* described by a discrete Schrödinger equation. Consequently it must be ascribed to transverse excitations, decoherence or heating.

In section 4.4.4 the experimental results of the experiments on the theoretically predicted scaling behavior are presented. By looking at the expansion of wave packets with different initial conditions, the scaling behavior is confirmed qualitatively. The ratio between the initial wave packet width and the final width in the self-trapping regime is found to depend universally on the ratio between the mean interaction energy and the width of the first Bloch band of the lattice potential.

At the end of this section the corresponding publication *Nonlinear Self-Trapping of Matter Waves in Periodic Potentials* is included as a summary of the results.

4.4.1 Experimental setup and wave packet preparation

In the experiments the expansion of wave packets inside a 1D waveguide with a superimposed deep lattice potential is investigated. The wave packets are realized with ^{87}Rb Bose-Einstein condensates, which are obtained by evaporative cooling in a 3D optical dipole trap. The trap consists of two crossed laser beams, the waveguide beam and a perpendicular oriented holding beam (for more details see section 2.2).

Important parameters in the preparation process are the atom number and the width in longitudinal (waveguide) direction of the wave packet. The number of atoms in the wave packet is adjusted by removing atoms from the condensate through evaporation. Both the waveguide beam and the holding beam intensity are reduced in such a way that a defined final atom number is reproducibly obtained. Subsequently the intensity of the waveguide and the holding beam are ramped up adiabatically, such that the waveguide

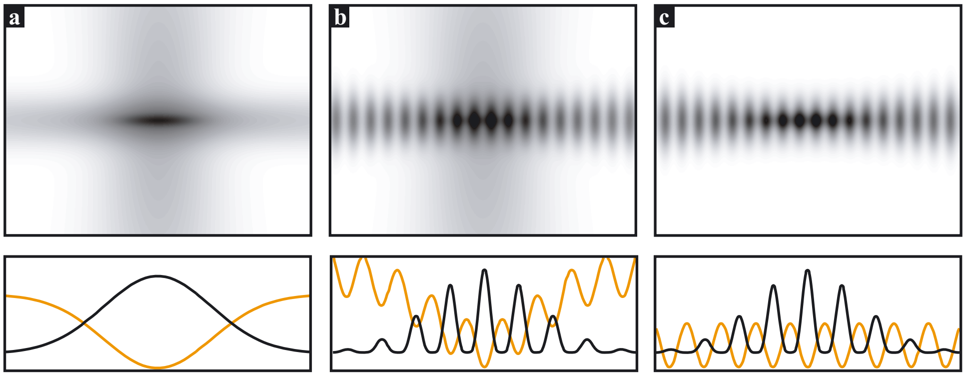

Figure 4.14: Schematic of the preparation of wave packets in a 1D waveguide with a superimposed deep lattice potential. **(a)** A coherent wave packet in a 3D optical trap of two crossed laser beams is created by Bose-Einstein condensation trough forced evaporative cooling. The holding beam (drawn vertically) defines the width of the wave packet in the horizontal waveguide direction **(b)** A deep lattice potential realized by the dipole force of a standing light wave along the waveguide is adiabatically ramped up. **(c)** The tunneling dynamics starts when the crossed laser beam of the 3D dipole trap is turned off.

offers tight transverse trapping with $\omega_\perp = 2\pi \cdot 230$ Hz. The final holding beam intensity is chosen such that the desired longitudinal wave packet width in the range of $7 - 20\,\mu$m rms is obtained (see figure 4.14).

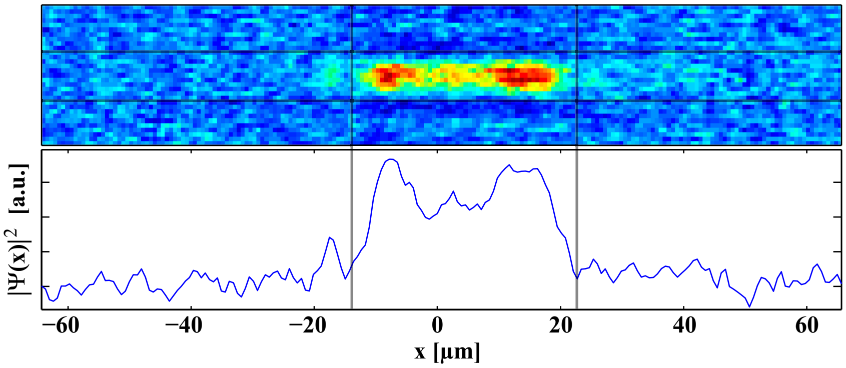

Figure 4.15: Analysis of the wave packet shape. In order to avoid large errors due to the background noise in the absorption image (upper graph) and non-condensed thermal background atoms, the region of interest (ROI), defined by the dark bars, is determined manually for each experiment. Relevant values such as the number of atoms and the rms-width are calculated using this ROI. The wave packet shape in x direction (lower graph) is obtained by integrating the ROI along the radial direction.

The lattice potential is realized by the dipole potential of two far red-detuned counter propagating laser beams, which are collinear with the waveguide (for details on the calibration see section 3.2). The intensity of the lattice beams is ramped up adiabatically[6] in 10 ms, such that the wave packet is prepared in the ground state of the combined

---

[6] The ramp up time is much longer than the maximum tunneling time $\max(\tau_T) \sim 2\,$ms.

trapping and lattice potential. Finally the holding beam is abruptly turned off and the resulting wave packet dynamics is observed for different propagation times by absorption imaging. The rms-width and the atom number of the wave packets are calculated from the manually selected image region, as depicted in figure 4.15, in order to avoid large errors due to the background noise in the absorption images.

4.4.2 Transition from the diffusive to the self-trapping regime

In the experiments described here, the dynamics of ^{87}Rb atoms with a repulsive atom-atom interaction is investigated. In free space this interaction tends to accelerate the expansion of an initially localized atomic wave packet. In a periodic potential, for moderate nonlinearity, the same accelerated expansion dynamics can be observed. This dynamical regime is referred to as the diffusive regime. When the nonlinearity is increased above a certain critical value, the initial expansion stops and the wave packet remains localized. This counterintuitive effect was first predicted theoretically in (Trombettoni, 2001) for the system considered here and is referred to as nonlinear self-trapping (see section 4.3 for a theoretical discussion).

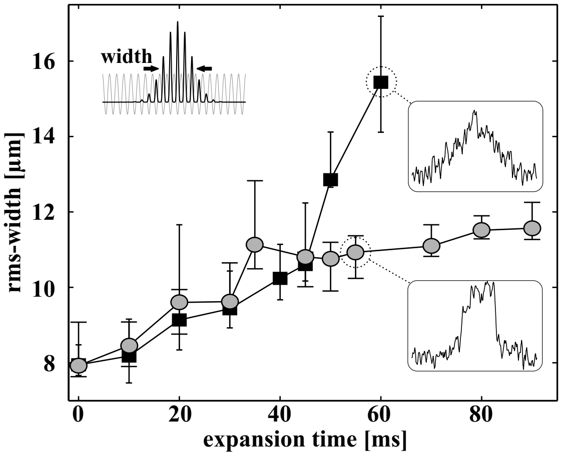

Figure 4.16: Observation of nonlinear self-trapping of Bose-condensed ^{87}Rb atoms. The dynamics of the wave packet width along the periodic potential is shown for two different initial atom numbers. By increasing the number of atoms from 2000 ± 200 (squares) to 5000 ± 600 (circles), the repulsive atom-atom interaction leads to the stopping of the global expansion of the wave packet. The insets show that the wave packet remains almost Gaussian in the diffusive regime but develops steep edges in the self-trapping regime.

Experimentally the transition from the diffusive to the self-trapping regime can be accomplished by increasing the nonlinear parameter Λ above the critical value, such that

$$\frac{\Lambda}{\Lambda_{\mathrm{c}}} \sim \frac{\langle \mu_{\mathrm{loc}}^{\mathrm{int}} \rangle}{E_{\mathrm{bw}}} > 1, \tag{4.49}$$

where $\langle \mu_{\mathrm{loc}}^{\mathrm{int}} \rangle$ is the mean local interaction energy and E_{bw} is the width of the lowest Bloch band. We have chosen to observe this effect by looking at the expansion of wave packets with identical initial width of $8\,\mu$m rms and identical parameters for the waveguide

($\omega_\perp = 2\pi \cdot 230$ Hz) and the periodic potential ($s = 11$). The transition is accomplished by increasing the number of atoms and thereby the atomic density in the wave packets.

In figure 4.16 the experimental signature of the transition from the diffusive to the self-trapping regime is shown. In the experiment wave packets with a number of atoms close to (2000 ± 200 atoms) and above (5000 ± 600 atoms) the critical value are prepared. Clearly both wave packets expand initially. At $t \sim 35$ ms the wave packet with the higher initial atomic density has developed steep edges and stops expanding (see inset in figure 4.16). In contrast, the wave packet with the lower initial atomic density continues to expand keeping its Gaussian shape. The theoretically expected faster initial expansion due to the increased repulsive interaction for wave packets with a larger number of atoms is also shown in the experimental results.

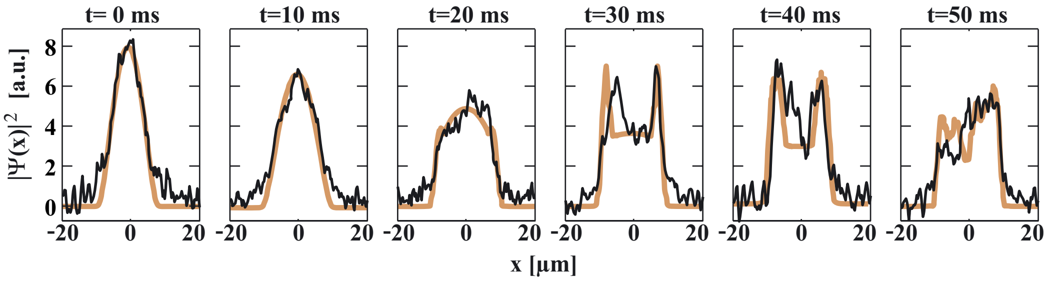

Figure 4.17: Detailed temporal evolution of the wave packet shape for $s = 10$; $7.6(5)\,\mu$m initial rms width and 5000 ± 600 atoms. The graphs show the measured density distribution for different propagation times (black). During the initial expansion in the self-trapping regime the wave packet develops steep edges which act as stationary boundaries for the subsequent internal dynamics. The results of the numerical integration of the DNL (4.28), depicted in orange, are in very good agreement. For $t = 50$ ms a 1.5 mrad deviation of the waveguides horizontal orientation (consistent with the experimental uncertainty) is taken into account and reproduces the experimentally observed asymmetry.

In figure 4.17 the experimental investigation of the detailed temporal shape dynamics of a wave packet in the self-trapping regime is shown. The experimental results clearly show the characteristic development of steep edges during the initial expansion and the subsequent development of strong side peaks. These pronounced side peaks disappear and a square shaped density distribution is formed finally. The observed asymmetry of the wave packet shapes (e.g. at $t = 50$ ms) appears due to the deviation from the perfect horizontal orientation of the waveguide (±2 mrad) which results from small changes in height of the pneumatic isolators of the optical table during the measurements.

In addition the experimental results are compared with the results of an integration of the DNL. The propagation of the DNL allows to reproduce all the experimentally observed features, including the observed asymmetry and the agreement is very good.

The experimental results presented in this section demonstrate for the first time the theoretically predicted effect of nonlinear self-trapping for a quasi 1D system of bosonic atoms in a deep lattice potential. The comparison with numerical calculations shows that the investigated experimental system can be described very well with the help of the DNL. This, in turn, allows us to use the results of the theoretical investigation of the effect of self-trapping (see section 4.3) to understand and to further investigate the experimental system.

4.4.3 Decay of self-trapping

In this section the experimental investigation of the decay of self-trapping is presented. In the theoretical investigation it was shown that essentially the nonlinear parameter Λ and the dimensionality of the system (DNL or DNLS) govern the decay of the effect of self-trapping. In the experimental system additional dynamical effects, that are not included in the DNL/DNLS, such as transverse excitations, decoherence and heating can affect the decay of self-trapping.

In order to distinguish between the *intrinsic* decay, i.e. the decay of self-trapping described by the discrete equations, and other *external* effects, the different dynamical equations and especially the relevant local chemical potential are reviewed. As a result a discrete non-polynomial Schrödinger equation (DNPSE) is developed by modifying the nonlinearity of the DNL, such that it correctly describes the relevant chemical potential both in the regime of small and in the regime of high atomic density.

Discrete non-polynomial Schrödinger equation

For the DNL the relevant chemical potential

$$\mu_j^{\mathrm{TF}} = U_1 \cdot \sqrt{N_j} = \left(\frac{m\omega_\perp^2 g_0}{\sqrt{2\pi}\pi\sigma_{\mathrm{latt}}} \right)^{1/2} \sqrt{N_j} \tag{4.50}$$

is the sum of the interaction energy in the Thomas-Fermi approximation and the potential energy in transverse direction due to the increased transverse width (see section 4.2.3). For the DNLS the relevant chemical potential

$$\mu_j^{\mathrm{lin}} = U \cdot N_j = g_0 N_j \cdot \frac{1}{(2\pi)^{3/2}\sigma_\perp^2 \sigma_{\mathrm{latt}}} \tag{4.51}$$

is only given by the interaction energy in the linear ground state approximation (see section 4.2.2). The dependence of μ_j^{lin} and μ_j^{TF} on the local number of atoms N_j is plotted in figure 4.18.

In the experiment the typical atomic densities are too large for the linear approximation (DNLS) and too small for the Thomas-Fermi approximation (DNL). In this intermediate regime the ground state function in a lattice site can be best approximated by a Gaussian wave function $\Phi(\vec{r}) = \exp(-x^2/\sigma_{\mathrm{latt}}^2) \cdot \exp(-r^2/\sigma_\perp^{\mathrm{var}}(N_j)^2)$, where the density dependent width $\sigma_\perp^{\mathrm{var}}(N_j)$ is obtained by a variational calculation (Baym/Pethick, 1996). The corresponding relevant chemical potential

$$\mu_j^{\mathrm{var}} = g_0 N_j \frac{1}{(2\pi)^{3/2}\sigma_\perp^{\mathrm{var}}(N_j)^2 \sigma_{\mathrm{latt}}} + \frac{1}{2}(m\omega_\perp^2 \sigma_\perp^{\mathrm{var}}(N_j)^2 - \hbar\omega_\perp) \tag{4.52}$$

is derived from the linear approximation, where $\sigma_\perp^{\mathrm{var}}(N_j)$ needs to be calculated numerically. The second term accounts for the increased potential energy due to the increased transversal width. In order to implement the corresponding discrete nonlinear equation, an explicit expression for μ_j^{var} is desired. In the derivation of the NPSE (Salasnich *et al.*, 2002) (see section 2.1.3) the explicit local transversal width

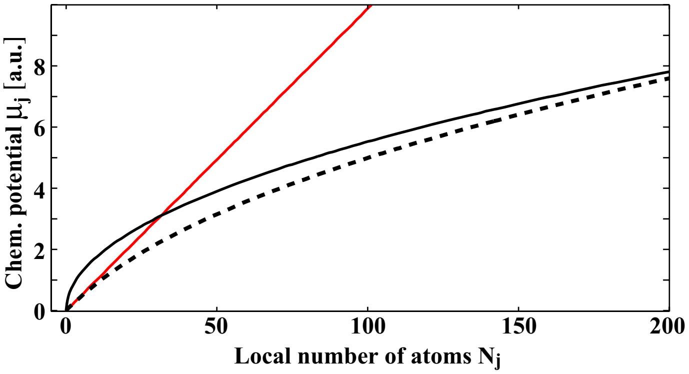

Figure 4.18: Local chemical potential μ_j for the different discrete nonlinear Schrödinger equations used in this thesis. The red line shows the chemical potential μ_j^{lin} for the linear approximation (DNLS), which is proportional to the local number of atoms N_j. The black line shows μ_j^{TF}, where the Thomas-Fermi approximation is used in transverse direction (DNL). The black dashed line shows μ_j^{var}, obtained from a variational calculation (DNPSE). μ_j^{var} describes the intermediate regime very well.

$\sigma_\perp(x)^2 = \sigma_\perp^2\sqrt{1+2a_s N_{\mathrm{T}}|\Psi(x)|^2}$ is obtained from a similar variational calculation as in (Baym/Pethick, 1996), where $N_{\mathrm{T}}|\Psi(x)|^2$ is the local linear density. In the case of a deep lattice potential the average linear density of a local condensate at site j can be approximated by $\rho_j = N_j/(4\sigma_{\mathrm{latt}})$. The variational relevant chemical potential can thus be written as

$$\mu_j^{\mathrm{var}} = g_0 N_j \frac{1}{(2\pi)^{3/2}(\sigma_\perp^{\mathrm{var}})^2\sigma_{\mathrm{latt}}} + \frac{1}{2}(m\omega_\perp^2(\sigma_\perp^{\mathrm{var}})^2 - \hbar\omega_\perp) \tag{4.53}$$

with $(\sigma_\perp^{\mathrm{var}})^2 = \sigma_\perp^2 \cdot \sqrt{1+2a_S N_j/(4\sigma_{\mathrm{latt}})}$. As can be seen in figure 4.18, the variational chemical potential μ_j^{var} describes the experimental system both in the regime of small and in the regime of high atomic density. The corresponding discrete non-polynomial Schrödinger equation

$$i\hbar\frac{\partial\psi_j}{\partial t} = \epsilon_j\psi_j - K(\psi_{j+1}+\psi_{j-1}) + \mu_j^{\mathrm{var}}\psi_n \tag{4.54}$$

called the DNPSE in this thesis[7] is used to investigate numerically the decay of the effect of self-trapping.

Experimental investigation of the decay of self-trapping

In figure 4.19 the experimental results on the long term expansion of wave packets is shown. In the first experiment the expansion of a wave packet with a total number of atoms $N_{\mathrm{T}} = 5000$, a lattice potential depth $U_{\mathrm{latt}} = 11\,\mathrm{E_r}$ and an initial width $\sigma_0 = 7.6\,\mu$m rms is investigated. For these system parameters the tunneling time is $t_T = \hbar/K \sim 2.4\,$ms, which is still larger than the transverse oscillation time $t_\perp = \omega_\perp^{-1} \sim 0.7\,$ms. The temporal evolution of the wave packet width is very well described by the three discrete

---

[7] Since a rigorous derivation is not done so far, the name is given for the use in this thesis only.

equations DNPSE, DNL and DNLS[8]. The observed decay of self-trapping is therefore mainly of *intrinsic* nature, i.e. a consequence of the coupling of single wells to two adjacent lattice sites.

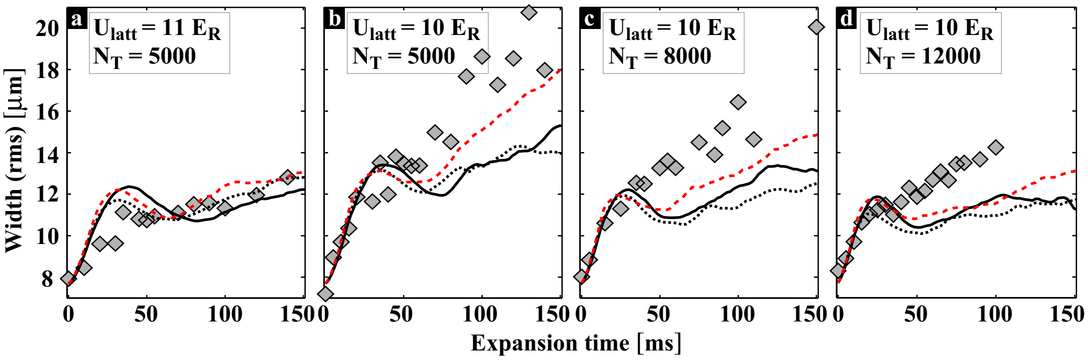

Figure 4.19: Experimental investigation of the decay of self-trapping. **(a)** For a lattice potential depth of $U_{\mathrm{latt}} = 11\,\mathrm{E_r}$ and $\omega_\perp = 2\pi \cdot 230$ Hz the experimentally observed decay of self-trapping is described by the discrete dynamical equations DNL (solid line), DNLS (dashed red line) and DNPSE (dotted line) and is thus mainly of *intrinsic* nature. **(b)** For $U_{\mathrm{latt}} = 10\,\mathrm{E_r}$ the decay is faster than predicted theoretically. This is mainly due to the reduced tunneling time and the corresponding increased probability of transversal excitations. **(c,d)** Moving deeper into the self-trapping regime by increasing the number of atoms does not prevent the fast decay.

In the second experiment the lattice potential depth is decreased to $U_{\mathrm{latt}} = 10\,\mathrm{E_r}$ with a corresponding tunneling time $t_T = \hbar/K \sim 1.8\,\mathrm{ms}$, which becomes comparable to the transverse oscillation time. Thus the probability of transverse excitations during the dynamics for these system parameters is increased. The experimental data shows the theoretically predicted evolution until the initial expansion is stopped. The wave packet remains trapped for $\sim 20\,\mathrm{ms}$ and then a fast decay is observed, which cannot be described by the discrete dynamical equations and must therefore be attributed to transverse excitations. Comparison with the numerical integration of the DNLS underlines that the experimentally observed decay is *not* due to the enhanced decay of a system described by the DNLS.

In the following experiments the number of atoms is increased to $N_{\mathrm{T}} = 8000$ and $N_{\mathrm{T}} = 12000$ and therefore the system is moved deeper into the self-trapping regime. Although the nonlinear parameter Λ is now comparable to the experimental system with $N_{\mathrm{T}} = 5000$ and $U_{\mathrm{latt}} = 11\,\mathrm{E_r}$, the transverse excitations due to the decreased tunneling time dominate and lead to a fast decay of the self-trapped wave packets.

The experimental results show that the tunneling time defined by the lattice potential depth is the most important parameter which governs the *external* decay of self-trapping. Other sources of heating and decoherence, such as the coupling to the non-condensed thermal cloud and possible phase fluctuations of the lattice potential may also play an important role.

---

[8] For the integration of the DNLS $\omega_\perp$ is chosen such that the average initial atomic density corresponds to the experimental situation.

4.4.4 Scaling behavior

In this section the results of the experimental investigation of universal scaling are presented. A simple variational solution of the DNLS/DNL system predicts a universal scaling behavior: the ratio between the initial and the final width γ_0/γ_∞ of a freely expanding wave packet in a deep lattice potential is only determined by the ratio between the initial average interaction energy and the band width of the lattice potential, i.e. the average nonlinear parameter $\Lambda_{\text{av}} = \langle \mu_{\text{loc}}^{\text{int}} \rangle / 2K$ (see section 4.3.4). In other words, varying the single system parameters such as the depth of the lattice potential, the initial width of the wave packet and the total number of atoms will not alter the ratio γ_0/γ_∞, as long as Λ_{av} is kept constant.

For a system with Λ_{av} less than the critical value[9] the final width is unbound and thus $\gamma_0/\gamma_\infty = 0$ (diffusive regime). Above the critical value the final width γ_∞ is finite (self-trapping regime) and $\gamma_0/\gamma_\infty \to 1$ for $\Lambda_{\text{av}} \to \infty$. This behavior is depicted by the theoretical curves shown in figure 4.20(a).

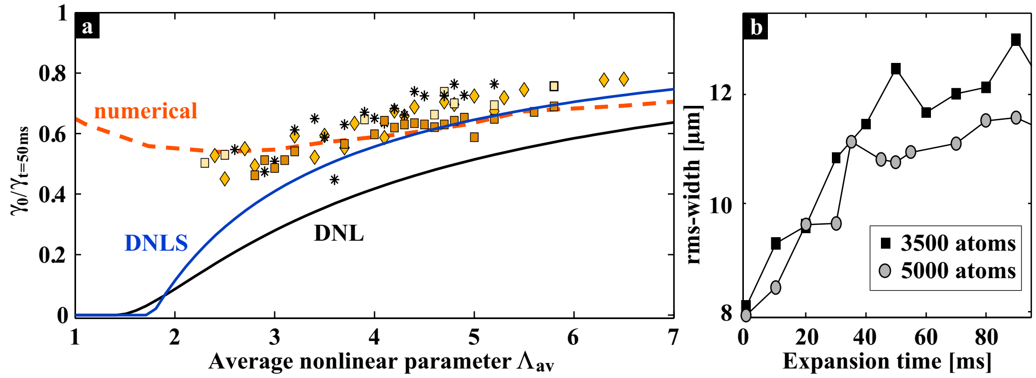

Figure 4.20: (a) Experimental investigation of the scaling behavior. The solid lines show the theoretical curves given by eq. (4.47) and (4.48). Experimentally the parameter Λ_{av} was varied by using three different periodic potential depths: $s = 10.6(3)$ (stars), 11.1(3) (squares), and 11.5(3) (diamonds). For each potential depth, wave packets with different atom numbers and initial widths are prepared and the width for $t = 50$ ms is measured. The experimental data show qualitatively the scaling behavior predicted theoretically and are in quantitative agreement with the results of the numerical integration of the DNL (dashed line). (b) The temporal evolution of two wave packets with different atom numbers depicts the nature of the scaling: increasing Λ_{av} (by, e.g., increasing the atom number) leads to a faster trapping and thus to a smaller final width.

In order to confirm the scaling behavior experimentally, the width $\gamma_{t=50\text{ms}}$ of the wave packet after 50 ms evolution is measured for different system parameters, i.e., total atom number, initial width of the wave packet, and depth of the periodic potential. For each experimental run the initial width of the wave packet is deduced from the measured number of atoms. To this end the initial width γ_0 of wave packets with different number of atoms with otherwise identical system parameters is recorded and fitted by a 1D Thomas-Fermi density distribution (see e.g. Ketterle *et al.*, 1998). For each experimental run the ratio $\gamma_0/\gamma_{t=50\text{ms}}$ is plotted in figure 4.20(a) versus the model

---

[9] The exact theoretical value depends on the model (DNLS or the DNL), which describes the system.

independent average nonlinear parameter

$$\Lambda_{\mathrm{av}} = \mu_{\mathrm{av}}^{\mathrm{var}}/2K, \tag{4.55}$$

where the average local chemical potential $\mu_{\mathrm{av}}^{\mathrm{var}}$ is calculated using eq. (4.53).

The experimental data show scaling in the sense that all data points collapse onto a single universal curve, i.e. data points with the same nonlinear parameter Λ_{av} show the same ratio $\gamma_0/\gamma_{t=50\mathrm{ms}}$. The experimental data show quantitative agreement with a numerical scaling curve obtained from an integration of the DNL (dashed line in figure 4.20a).

The experimental data points lie above the theoretical curves, i.e. the experimentally observed trapping occurs faster than theoretically predicted. This quantitative difference between the experimental data and the result of the variational calculation (solid lines) is mainly due to two reasons. In the variational calculation an initial Gaussian shape is assumed, while in the experiment the initial wave packet shape is nearly parabolic. In addition, the variational calculation assumes a Gaussian shape during the evolution, in contrast to the experimental situation, where a square shaped density distribution is formed during the dynamics.

The experimental investigation of the scaling behavior shows again that the ratio $\Lambda_{\mathrm{av}} = \langle \mu_{\mathrm{loc}}^{\mathrm{int}} \rangle / 2K$ governs the transition between the diffusive and the self-trapping regime and, in addition, governs the global dynamics of the wave packet width.

4.4.5 Publication: Nonlinear Self-Trapping of Matter Waves in Periodic Potentials

The experimental results on the nonlinear self-trapping of matter waves are published in (Anker *et al.*, 2005). As a summary, the publication is included below. In comparison to the original publication, here equation (4) is corrected.

Nonlinear Self-Trapping of Matter Waves in Periodic Potentials

Th. Anker[1], M. Albiez[1], R. Gati[1], S. Hunsmann[1], B. Eiermann[1], A. Trombettoni[2] and M.K. Oberthaler[1]
[1] *Kirchhoff Institut für Physik, Universität Heidelberg,*
Im Neuenheimer Feld 227, 69120 Heidelberg, Germany
[2] *I.N.F.M. and Dipartimento di Fisica, Universitá di Parma,*
parco Area delle Scienze 7A, I-43100 Parma, Italy

We report the first experimental observation of nonlinear self-trapping of Bose-condensed ^{87}Rb atoms in a one dimensional waveguide with a superimposed deep periodic potential . The trapping effect is confirmed directly by imaging the atomic spatial distribution. Increasing the nonlinearity we move the system from the diffusive regime, characterized by an expansion of the condensate, to the nonlinearity dominated self-trapping regime, where the initial expansion stops and the width remains finite. The data are in quantitative agreement with the solutions of the corresponding discrete nonlinear equation. Our results reveal that the effect of nonlinear self-trapping is of local nature, and is closely related to the macroscopic self-trapping phenomenon already predicted for double-well systems.

PACS numbers: N03.75.Lm,63.20.Pw
Keywords:

The understanding of coherent transport of waves is essential for many different fields in physics. In contrast to the dynamics of non-interacting waves, which is conceptually simple, the situation can become extremely complex as soon as interaction between the waves is of relevance. Very intriguing and counter intuitive transport phenomena arise in the presence of a periodic potential. This is mainly due to the existence of spatially localized stationary solutions.

In the following we will investigate the dynamics of Bose-condensed ^{87}Rb atoms in a deep one dimensional periodic potential, i.e. the matter waves are spatially localized in each potential minimum (tight binding) and are coupled via tunneling to their next neighbors. This system is described as an array of coupled Boson Josephson junctions [1]. The presence of nonlinearity drastically changes the tunneling dynamics [2] leading to new localization phenomena on a macroscopic scale such as discrete solitons, i.e. coherent non-spreading wave packets, and nonlinear self-trapping [3]. These phenomena have also been studied in the field of nonlinear photon optics where a periodic refractive index structure leads to an array of wave guides, which are coupled via evanescent waves [4].

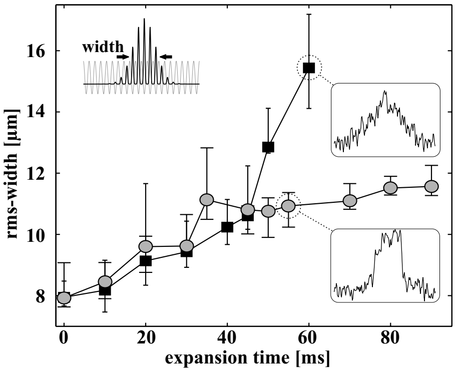

FIG. 1: Observation of nonlinear self-trapping of Bose-condensed ^{87}Rb atoms. The dynamics of the wave packet width along the periodic potential is shown for two different initial atom numbers. By increasing the number of atoms from 2000±200(squares) to 5000±600(circles), the repulsive atom-atom interaction leads to the stopping of the global expansion of the wave packet. The insets show that the wave packet remains almost gaussian in the diffusive regime but develops steep edges in the self-trapping regime. These edges act as boundaries for the complex dynamics inside.

In this letter we report on the first experimental confirmation of the theoretically predicted effect of nonlinear self-trapping of matter waves in a periodic potential [3]. This effect describes the drastic change of the dynamics of an expanding wave packet, when the nonlinearity i.e. repulsive interaction energy, is increased above a critical value. Here the counterintuitive situation arises that although the spreading is expected to become faster due to the higher nonlinear pressure, the wave packet *stops* to expand after a short initial diffusive expansion. Since we observe the dynamics in real space, we can directly measure the wave packet width for different propagation times. In Fig. 1 we show the experimental signature of the transition from the diffusive to the self-trapping regime. We prepare wave packets in a periodic potential and change only the nonlinear energy by adjusting the number of atoms in the wave packet close to (2000±200 atoms) and above (5000±600 atoms) the critical value. Clearly both wave packets expand initially. At $t \sim 35$ ms the wave packet with higher initial atomic density has developed steep edges and stops expanding (see inset in Fig. 1). In contrast, the wave packet with the lower initial atomic density continues to expand keeping its gaussian shape.

The coherent matter-wave packets are generated with ^{87}Rb Bose-Einstein condensates realized in a crossed light beam dipole trap ($\lambda = 1064n$m, $1/e^2$ waist 55μm, $600m$W per beam). Subsequently a periodic dipole potential $V_p = s{\cdot}E_r \sin^2(kx)$, realized with a far off-resonant standing light wave ($\lambda = 783n$m) collinear with one of the dipole trap beams is adiabatically ramped up . The depth of the potential is proportional to the intensity of the light wave and is given in recoil energies $E_r = \frac{\hbar^2 k^2}{2m}$ with the wave vector $k = 2\pi/\lambda$. By switching off the dipole trap beam perpendicular to the periodic potential the atomic matter wave is released into a trap acting as a one-dimensional waveguide $V_{dip} = \frac{m}{2}(\omega_\perp^2 r^2 + \omega_\parallel^2 x^2)$ with radial trapping frequency $\omega_\perp = 2\pi \cdot 230\,\text{Hz}$ and longitudinal trapping frequency $\omega_\parallel \approx 2\pi \cdot 1\,\text{Hz}$. The wave packet evolution inside the combined potential of the waveguide and the lattice is studied by taking absorption images of the atomic density distribution after a variable time delay. The density profiles $n(x,t)$ along the waveguide are obtained by integrating the absorption images over the radial dimensions and allow the detailed investigation of the wave packet shape dynamics with a spatial resolution of 3μm.

In Fig. 2 the measured temporal evolution of the wave packet prepared in the self-trapping regime ($s = 10$, 7.6(5) μm initial rms-width, 5000±600 atoms) is shown. The evolution of the shape is divided into two characteristic time intervals. Initially ($t < 20$ ms) the wave packet expands and develops steep edges. This dynamics can be understood in a simple way by considering that the repulsive interaction leads to a broadening of the momentum distribution and thus to a spreading in real space. Since the matter waves propagate in a periodic potential the evolution is governed by the modified dispersion (i.e. band structure) $E(q) = -2K\cos(dq)$ where $d = \lambda/2$ is the lattice spacing, $\hbar q$ is the quasimomentum and K is the characteristic energy associated with the tunneling. The formation of steep edges is a consequence of the population of higher quasimomenta around $q = \pm\pi/2d$ where the dispersion is strongly reduced and the group velocity is extremal. In order to populate quasimomenta $|q| > \pi/2d$ the initial interaction energy has to be higher than the characteristic tunneling energy K and thus the critical parameter depends on the ratio between the on-site interaction energy and the tunneling energy as we will discuss in detail. While in the linear evolution the steep edges move with the extremal group velocity [5], in the experiment reported here they stop after their formation. As we will show this is a consequence of the high atomic density gradient at the edge which suppresses tunneling between neighboring wells. The further evolution is characterized by stationary edges acting as boundaries for the complex internal behavior of the wave packet shape. The formation of the side peaks is an indication that atoms moving outwards are piled up because they cannot pass the steep edge. Finally the pronounced features of the wave packet shape disappear and a square shaped density distribution is formed.

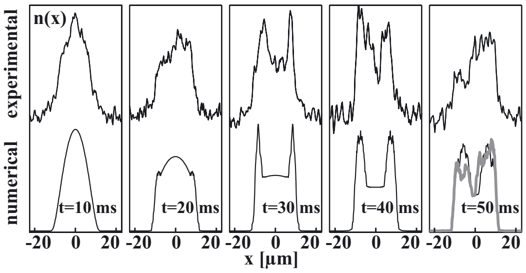

FIG. 2: Comparison between theory and experiment for $s =$ 10, 7.6(5) μm initial rms-width, and 5000±600 atoms. The upper graphs show the measured density distribution for different propagation times. During the initial expansion in the self-trapping regime the wave packet develops steep edges which act as stationary boundaries for the subsequent internal dynamics. The results of the numerical integration of eq. 2 (depicted in the lower graphs) are in very good agreement. For $t = 50$ ms a 1.5 $m$rad deviation of the wave guides's horizontal orientation (consistent with the experimental uncertainty) is taken into account and reproduces the experimentally observed asymmetry (gray line).

In order to understand in detail the ongoing complex self-trapping dynamics we compare quantitatively our experimental findings with numerically obtained solutions (see Fig. 2). For our typical experimental parameters of $s \sim 11$ and ~ 100 atoms per well we are in the regime where the dynamics can be described by a macroscopic wave function $\Psi(\vec{r},t)$ and thus by the Gross-Pitaevski equation (GPE) [6]. Since we use deep optical lattices the description can be reduced to a one dimensional discrete nonlinear equation, which includes the fundamental processes, namely tunneling between the wells and nonlinear phase evolution due to the interaction of the atoms [3, 7]. In our experiment the trapping frequency in a single well along the lattice period is on the order of $\omega_x \approx 2\pi \cdot 25$ kHz, whereas the transverse trapping frequency of the wave guide is $\omega_\perp = 2\pi \cdot 230\,\text{Hz}$. Thus our system can be described as a horizontal pile of pancakes, and the transverse degree of freedom cannot be neglected. In [7] a one dimensional discrete nonlinear equation (DNL) is derived which takes into account the adiabatic change of the wave function in the transverse direction due to the atom-atom interaction. A generalized tight binding ansatz

$$\Psi(\vec{r},t) = \sum_j \psi_j(t)\Phi_j(\vec{r},N_j(t)) \qquad (1)$$

is used, with $\psi_j(t) = \sqrt{N_j(t)}e^{i\phi_j(t)}$, where $N_j(t)$ is the atom number and $\phi_j(t)$ is the phase of the jth condensate. Φ_j is normalized to 1 (i.e. $\int d\vec{r}\Phi_j^2 = 1$) and $\Psi(\vec{r}, t)$ is normalized to the total number of atoms N_T (i.e. $\sum_j |\psi_j|^2 = N_T$). The spatial real wave function $\Phi_j(\vec{r}, N_j(t))$ is centered at the minimum of the j-th well and is time dependent through $N(t)$. Integrating over the spatial degrees of freedom, the following DNL is obtained from the GPE :

$$i\hbar\frac{\partial\psi_j}{\partial t} = \epsilon_j\psi_j - K(\psi_{j+1} + \psi_{j-1}) + \mu_j^{loc}\psi_j. \quad (2)$$

K is the characteristic tunneling energy between adjacent sites. $\epsilon_j = \int d\vec{r}\frac{m}{2}\omega_\parallel^2 x^2\Phi_j^2$ is the on-site energy resulting from the longitudinal trapping potential, which is negligible in the description of our experiment. The relevant chemical potential is given by $\mu_j^{loc} = \int d\vec{r}\left[\frac{m}{2}\omega_\perp^2 r^2\Phi_j^2 + g_0|\psi_j(t)|^2\Phi_j^4\right]$ with $g_0 = 4\pi\hbar^2 a/m$ (a is the scattering length). It can be calculated approximately for our experimental situation assuming a parabolic shape in transverse direction (Thomas-Fermi approximation) and a Gaussian shape in longitudinal direction for $\Phi_j(\vec{r}, N_j(t))$ ($\omega_x \gg \mu_j^{loc}/\hbar > \omega_\perp$). This leads to $\mu_j^{loc} = U_1|\psi_j(t)|$ with

$$U_1 = \sqrt{\frac{m\omega_\perp^2 g_0}{\sqrt{2\pi}\pi\sigma_x}}. \quad (3)$$

Here $\sigma_x = \lambda/(2\pi s^{\frac{1}{4}})$ is the longitudinal Gaussian width of Φ_j in harmonic approximation of the periodic potential minima. Please note, that if the local wave function Φ_j does not dependent on N_j eq. 2 reduces to the well known discrete nonlinear Schrödinger equation with $\mu_j^{loc} \propto N_j$ [3, 8].

We compare the experimental and numerical results in Fig. 2 and find very good agreement. The theory reproduces the observed features such as steepening of the edges, the formation of the side peaks and the final square wave packet shape. It is important to note that all parameters entering the theory (initial width, atom number, periodic potential depth and transverse trapping frequency) have been measured independently. The observed asymmetry of the wave packet shapes (e.g. see Fig. 2, $t = 50ms$) appears due to the deviation from the perfect horizontal orientation of the wave guide ($\pm 2m$rad) which results from small changes in height of the pneumatic isolators of the optical table during the measurements.

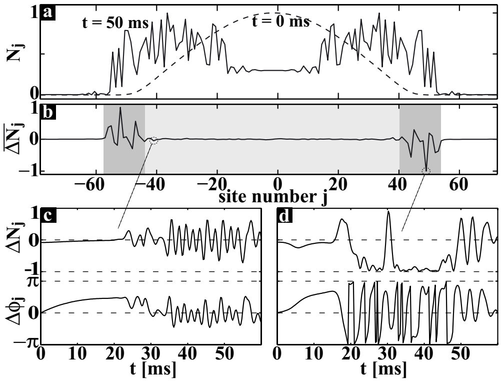

FIG. 3: A numerical investigation of the site to site tunneling dynamics. (a) The atomic distribution N_j of the wave packet for $t = 0$ and 50 ms. (b) The relative population difference ΔN_j time averaged over the expansion time indicates two regions with different dynamics. (c) The dynamics of ΔN_j and the phase difference $\Delta\phi_j$ for the marked site oscillate around zero known as the zero-phase mode of the Boson Josephson junction. (d) The dynamics in the edge region is characterized by long time periods where $|\Delta N_j|$ is close to 1 while at the same time $\Delta\phi_j$ winds up very quickly (phase is plotted modulo π) known as 'running phase self-trapping mode' in Boson Josephson junctions. Thus the expansion of the wave packet is stopped due to the inhibited site to site tunneling at the edge of the wave packet.

In the following we will use the numerical results to get further insight into the self-trapping dynamics. We investigate the local tunneling dynamics and phase evolution by evaluating the relative atom number difference $\Delta N_j = (N_{j+1} - N_j)/(N_{j+1} + N_j)$ and the phase difference $\Delta\phi_j = \phi_{j+1} - \phi_j$ between two neighboring sites. In Fig. 3a) the wave packet shapes for $t = 0$ and $t = 50ms$ are shown. In Fig. 3b) we plot the relative atom number difference ΔN_j averaged over the whole propagation duration of $50ms$. The graph indicates two spatial regions with different characteristic dynamics. While the average vanishes in the central region (shaded in light gray) it has significant amplitude in the edge region (shaded in dark gray). The characteristic dynamics of ΔN_j and $\Delta\phi_j$ in the central region is depicted in Fig. 3c). The atom number difference as well as the phase difference oscillate around zero. This behavior is known in the context of BEC in double-well potentials. It is described as the Boson Josephson junction 'zero-phase mode' [2] and is characteristic for superfluid tunneling dynamics if the atom number difference stays below a critical value. At the edge in contrast, ΔN_j crosses the critical value during the initial expansion (steep density edge) and locks for long time periods to high absolute values showing that the tunneling and thus the transport is inhibited. At the same time the phase difference winds up. This characteristic dynamics has been predicted within the Boson Josephson junction model for a double-well system and is referred to as the 'running phase self-trapping mode' [2]. This analysis makes clear that the effect of nonlinear self-trapping as observed in our experiment is a *local* effect and is closely related to Boson Josephson junctions dynamics in a double-well system.

Although the local dynamics just described is very complex, the evolution of the root mean square width of the wave packet, i.e. the global dynamics, can be predicted analytically within a very simple model. In [3] a Gaussian profile wave packet $\psi_j(t) \propto \exp(-(\frac{j}{\gamma(t)})^2 + i\frac{\delta(t)}{2}j^2)$ parameterized by the width $\gamma(t)$ (in lattice units) and the quadratic spatial phase $\delta(t)$, is used as an ansatz for quasimomentum $q = 0$ to solve the discrete nonlinear Schrödinger equation. The time evolution of the width $\gamma(t)$ is obtained analytically applying a variational principle. The result of this simple model is, that the dynamics of the wave packet width is solely determined by two global parameters - the density of the atoms and the depth of the periodic potential. Also a critical parameter Λ/Λ_c can be deduced, which governs the transition from the diffusive to the self-trapping regime. The transition parameter Λ/Λ_c for the 2D case described by eq. 2 is obtained following the same lines of calculation as in [3]. Assuming that the initial width $\gamma_0 \gg 1$ (in the experiment typically $\gamma_0 \approx$40) we obtain

$$\Lambda = \frac{U_1\sqrt{N_T}}{2K} \quad \text{and} \quad \Lambda_c = \frac{3}{2}\left(\frac{9\pi}{8}\right)^{\frac{1}{4}}\sqrt{\gamma_0}.$$

A surprising result of this model is the prediction of the following scaling behavior (shown in Fig. 4):

$$\frac{\gamma_0}{\gamma_\infty} = \left(1 - \frac{\Lambda_c}{\Lambda}\right)^2 \qquad (4)$$

for $\Lambda/\Lambda_c > 1$, where γ_∞ is the width of the wave packet for $t \to \infty$. For $\Lambda/\Lambda_c < 1$ the width is not bound and thus the system is in the diffusive regime. In the regime $\Lambda/\Lambda_c > 1$ the width is constant after an initial expansion (see inset Fig. 4). Since $\Lambda/\Lambda_c \propto \mu_{av}^{loc}/K$, the self-trapping regime is reached by either reducing the initial width, increasing the height of the periodic potential or, as is shown in Fig. 1, by increasing the number of atoms.

Scaling means that all data points (i.e. different experimental settings with the same Λ/Λ_c) collapse onto a single universal curve. In order to confirm the scaling behavior experimentally we measure the width of the wave packet after 50*ms* evolution for different system parameters, i.e. atom number, initial width of the wave packet, and depth of the periodic potential. The experimental results shown in Fig. 4 confirm the universal scaling dependence on Λ/Λ_c and follow qualitatively the prediction of the simple model. The dashed line in Fig. 4 is the result of the numerical integration of the discrete nonlinear equation given in eq. 2 evaluated at t =50*ms*. It shows quantitative agreement with the experiment. The difference between the numerical (dashed line) and analytical calculation (solid line) is due to the initial non-gaussian shape (numerically obtained ground state) and the strong deviation from the gaussian shape for long propagation times.

Concluding we have demonstrated for the first time the predicted effect of nonlinear self trapping of Bose-Einstein condensates in deep periodic potentials. The detailed analysis shows that this is a *local* effect, which occurs due to nonlinearity induced inhibition of site to site tunneling at the edge of the wave packet. This behavior is closely connected to the phenomenon of macroscopic self trapping known in the context of double-well systems. Furthermore we quantitatively confirm in our experiments the predicted critical parameter which discriminates between diffusive and self trapping behavior.

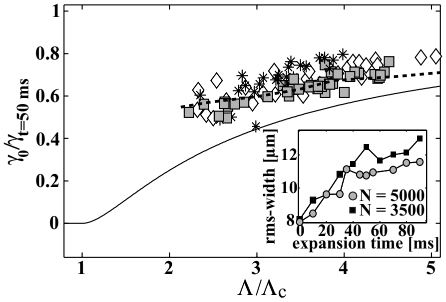

FIG. 4: Experimental investigation of the scaling behavior. The solid line shows the curve given by eq. 4. Experimentally the parameter Λ/Λ_c was varied by using three different periodic potential depths: s = 10.6(3) (stars), 11.1(3) (squares) and 11.5(3) (diamonds). For each potential depth wave packets with different atom numbers and initial widths are prepared and the width for t = 50 *ms* is determined. The experimental data show qualitatively the scaling behavior predicted by eq. 4 and are in quantitative agreement with the results of the numerical integration of the DNL (dashed line). The inset depicts the nature of the scaling: increasing Λ/Λ_c (by e.g. increasing the atom number) leads to a faster trapping and thus to a smaller final width.

We wish to thank A. Smerzi for very stimulating discussions. This work was supported by the Deutsche Forschungsgemeinschaft, Emmy Noether Programm, and by the European Union, RTN-Cold Quantum Gases, Contract No. HPRN-CT-2000-00125.

[1] F.S. Cataliotti, S. Burger, C. Fort, P. Maddaloni, F. Minardi, A. Trombettoni, A. Smerzi, and M. Inguscio, Science **293**, 843 (2001).

[2] A. Smerzi, S. Fantoni, S. Giovanazzi, and S. R. Shenoy Phys. Rev. Lett. **79**, 4950 (1997); S. Raghavan, A. Smerzi, S. Fantoni, and S.R. Shenoy, Phys.Rev. A **59**, 620 (1999); G.J. Milburn, J. Corney, E.M. Wright, D.F. Walls, Phys.Rev. A **55**, 4318 (1997).

[3] A. Trombettoni and A. Smerzi, Phys. Rev. Lett. **86**, 2353 (2001).

[4] for example: D.N. Christodoulides and F. Lederer and Y. Silberberg, Nature **424**, 817 (2003).

[5] B. Eiermann, P. Treutlein, Th. Anker, M. Albiez, M. Taglieber, K.-P. Marzlin, and M.K. Oberthaler, Phys. Rev. Lett. **91**, 060402 (2003).

[6] W. Zwerger J.Opt.B: Quantum semiclass. Opt. **5**, S9 (2003).
[7] A. Smerzi and A. Trombettoni, Phys.Rev. A **68**, 023613 (2003).
[8] D. Hennig and G.P. Tsironis, Phys.Rep. **307**,333 (1999); P.G. Kevrekidis, K.O. Rasmussen, and A.R. Bishop, Int.J.Mod.Phys.B **15**, 2833 (2001); M. Johansson and S. Aubry, Nonlinearity **10**, 1151 (1997).

5 Outlook

Bose-Einstein condensates in 1D optical lattice potentials constitute a very versatile model system. The implementation of dispersion management, the realization of bright atomic gap solitons and the observation of nonlinear self-trapping, described in this work, demonstrate some of the possibilities offered by this system. In this context I summarize in the following some ideas for future investigations concerning the field of quantum mechanics, chaos and atomic physics.

Following the lines of (Raghavan *et al.*, 1998), the equations of motions for the local fractional population difference and the local relative phase for a system described by the DNLS can be derived analytically. Based on these equations, the derivation of an analytic expression for intrinsically localized modes (IlM), such as discrete solitons (Ahufinger *et al.*, 2004) and stable edges (Darmanyan *et al.*, 1999) should be possible. ILM are important for the quantum transport in lattice potentials and allow a deeper understanding of the local self-trapping dynamics.

Also from a theoretical point of view, a comparison of the results of self-trapping in lattice potentials with the results of the recent observation of self-trapping in random potentials (Clément *et al.*, 2005) should provide additional information on the process of self-trapping.

Our experimental setup allows the implementation of the atom optics realization of the delta kicked rotor (Moore *et al.*, 1995) with Bose-Einstein condensates and thus with a very small width in momentum space. The atom optics system has enabled the experimental study of the transition between quantum and classical behavior. For example, the effects of decoherence, i.e the mechanism whereby quantum interference effects are destroyed via environmental coupling (Zurek, 1991), have been studied in the quantum system. More classical-like behaviour is observed when decoherence is added, e.g. by spontaneous emission (Klappauf *et al.*, 1998).

The *standard map*, a pair of mathematical transformation equations known in the field of chaos, represents the physical system of the delta kicked rotor. It is useful for studying the basic features of chaotic motion. In this context, the implementation of the standard map by means of the atom optics realization of the delta kicked rotor with Bose-Einstein condensates allows to study localization effects and possibly the formation of an Arnol'd stochastic web (Gardiner *et al.*, 2000).

By adding two pairs of counter propagating laser beams perpendicular to the waveguide axis, an array of tube potentials with large transversal trapping frequencies can be realized. Together with the lattice potential along the waveguide (Paredes *et al.*, 2004) and its velocity control, this system allows to investigate the regime of strongly interacting atoms in a moving system (Altman *et al.*, 2005).

Since the author will leave the working field of experimental research at the university,

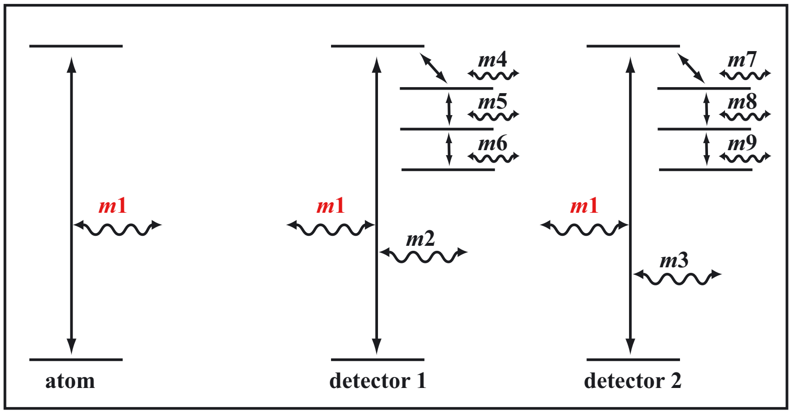

Figure 5.1: Complete quantum system. An initially excited two-level atom is coupled to the electro-magnetic field mode $m1$. Two spatially separated photon detectors are coupled resonantly to mode $m1$. The detection of the photon $m1$ is given by an increase of the temperature of the heat reservoirs, to which the top detector levels are coupled, e.g. via phonons $m4$ - $m9$. The environment is included in form of far detuned and *not* necessarily identical modes $m2$ and $m3$ (photon or phonon), which are coupled to the detectors.

the personal future project will be the numerical investigation of the collapse of the wave function, i.e. the measurement problem in quantum mechanics. The hope is, to identify the quantum process of measurement by investigating numerically the unitary evolution of a complete quantum system that comprises the system of interest, the detectors and the environment.

An example model system is described in figure 5.1. We first think of detectors 1 and 2 as two-level systems which are coupled only to mode $m1$. Then, during the evolution, the energy of the excited atom is transferred into mode $m1$ and subsequently absorbed by the detectors and we find the system in a state, where both detectors are in an equal superposition of ground and excited state. In a second step we introduce an *environment* by a coupling of detectors 1 and 2 to different far detuned modes $m2$ and $m3$, respectively. The difference of the two modes $m2$ and $m3$ is due to e.g. the different spatial positions of detector 1 and 2. This environment has the form of a perturbation and consequently does not induce decoherence (Braun *et al.*, 2001). Preliminary calculations have shown that such a perturbation can lead to a small asymmetry in the excitation of the two detectors.

In the future calculations the detectors will be coupled to a *macroscopic* heat reservoir, here described by a strong coupling to many initially empty phonon modes $m4$ - $m9$. Then the detection is described by an increase of the temperature of the spatially separated heat reservoirs, to which the detectors are coupled. The calculations shall provide an understanding of the influence of an environment in the case of *macroscopic* detectors.

The numerical implementation of the photon(phonon)-atom interaction can be done using the Jaynes-Cummings model (Cohen-Tannoudji *et al.*, 1992). The technical challenge is to reduce the very large number ($>10^3$) of basis states of this many-particle system.

A Appendix

A.1 Matlab© code for the wave packet propagation in 1D with the NPSE

```
% numerical propagation of the NPSE with a split-step Fourier method
clear
tic
% --------- constants ---------------------------------------
m = 1.4445e-25;           % Mass of 87 Rb
h = 6.626e-34;hbar=h/2/pi;% well ...
a = 5.32e-9;              % scattering length
lambda = 783e-9           % wavelength of beam realizing lattice pot
kr = 2*pi/lambda;         % recoil momentum
Er = (hbar^2*kr^2/2/m);   % recoil energy
% --------- numerical propagation parameters ---------------
N = 2^13;                 % number of discrete points of Psi(x) / Psi(k)
G = 2*kr;                 % lattice recoil vector
dk = 8*G/N;               % momentum sampling length (# of B-zones)/N
k = [-(N-1)/2*dk:dk:(N-1)/2*dk]-1/2*dk;  % momentum vector
dx = 2*pi/(dk*N)          % corresponding real space sampling length
x = [-(N-1)/2*dx:dx:(N-1)/2*dx]-dx/2;min(x),max(x)  % real space vector
dt = 5e-6;                % single time step dt
% --------- physical system parameters ----------------------
omega = 2*pi*0.1;         % axial frequency of harm. waveguide pot.
omega_perp = 2*pi*200;    % radial frequency of harm. waveguide pot.
atoms = 1000;             % number of atoms in wave packet
g1d = atoms*2*hbar*a*omega_perp; % 1d coupling cons. in meanfield energy
Ek = hbar^2*k.^2/(2*m)/Er;% vacuum dispersion relation
sigma0 = 10e-6;           % 1/e^2-width of initial gaussian wave packet
psi_x = exp(-(x).^2/(sigma0)^2); % Initial Gaussian wave function
Norm = sum(abs(psi_x).^2);% Norm
psi_x = psi_x/sqrt(Norm); % Psi normalized
T = 50e-3;                % propagation time
save_t = 5e-3;             % time between saved wave functions
% -------- program variables ----------------------------------
counter=0;
steps = round(T/dt);   % # of single propagation steps
save_steps = round(save_t/dt); % # of s. prop. steps between saved Psi's
```

```
saves = 1+floor(T/save_t);% # of saved wave functions
PSI_x = zeros(saves,N);  % empty matrix with wave functions Psi(t,x)
PSI_k = zeros(saves,N);  % empty matrix with wave functions Psi(t,k)
psi_k =fftshift(fft(psi_x));% initial momentum distribution
PSI_k(1,:)  = psi_k;      % save initial functions
PSI_x(1,:)  = psi_x;
% ------ propagation -------------------------------
toc
psi_k = exp(-i*Ek*Er/hbar*dt/2).*psi_k;  % dt/2 in momentum space
psi_x = ifft(psi_k);      % FFT^-1 -> real space
for i2=1:steps
  Vx  = 1/2*m*omega^2*x.^2;             % axial wg potential
  V2x = g1d*abs(psi_x).^2/dx./sqrt(1+2*a*atoms.*abs(psi_x).^2/dx)...
       +0.5*hbar*omega_perp.*(1./sqrt(1+2*a*atoms.*abs(psi_x).^2/dx)...
       +sqrt(1+2*a*atoms.*abs(psi_x).^2/dx)); % mean field energy
  psi_x = exp(-i*(Vx+V2x)/hbar*dt).*psi_x; % dt in real space
  psi_k = fft(psi_x);                      % FFT -> k-space
  psi_k = exp(-i*Ek*Er/hbar*dt).*psi_k;    % dt in k-space
  psi_x = ifft(psi_k);                     % FFT^-1 -> real space
  if i2/save_steps==round(i2/save_steps);  % save/plot intermediate steps
    counter=counter+1;
    PSI_k(counter,:)=psi_k;PSI_x(counter,:)=psi_x;
    subplot(2,2,1);
    plot(x,abs(psi_x).^2,x,Vx*max(abs(psi_x).^2)/max(Vx));
    axis([-100e-6 100e-6 -inf inf]);
    str1(1)={['propagation time=' num2str(i2*dt*1000,3) 'ms']};
    str1(2)={['elapsed calc. time=' num2str(toc)]};
    str1(3)={['remaining calc. time=' num2str(toc*(steps-i2)/i2,3)]};
    text(-20e-6,0.5*max(abs(psi_x).^2),str1)
    subplot(2,2,3);
    plot(k/kr,abs(psi_k).^2);
    axis([-.5 .5 -inf inf]);
    subplot(2,2,2);
    plot(x,atan(imag(psi_x)./(real(psi_x))))
    axis([-100e-6 100e-6 -inf inf]);
    subplot(2,2,4);
    plot(k/kr,atan(imag(psi_k)./(real(psi_k))))
    axis([-.5 .5 -inf inf]);
    drawnow;
  end;
end;
```

A.2 Matlab© code for the numerical calculation of the optical imaging

```
% numerical fourier optics to propagate the imaging beam
% system:
% 1. Light@BEC -> free propagation to lens
% 2. phase imprint @ the lens (ideal lens with finite size)
% 3. Light@lens -> free propagation from lens to CCD-camera
% 4. record Intensity @ CCD-camera
%---------------------------------------------------------------

% ----- constants ---------
lambda=780e-9;          % wavelength
width_beam=1.8e-3;      % 1/e^2 width of the imaging beam
N=2^19;                 % Number of discrete points
Length_xaxis=.1;        % size system
dx=Length_xaxis/(N-1); %smallest step size of x-axis
x=[-(N-1)/2*dx:dx:(N-1)/2*dx]-1/2*dx; % x-axis
k=2*pi/lambda;          % wave vector
M=10;                   % Magnification
f_lens=0.08;            % focal length of lens
xlens=0e-19;            % distance of lens from beam axis
lens_size=50e-3;        % diameter of lens
z1=(M+1)/M*f_lens;      % distance from bec -> lens
z2=(M+1)*f_lens;        % distance from lens -> CCD-camera
sigma=2e-6;             % width of the BEC
OD=1;                   % optical density
delta=0;                % detuning from resonance
amplitude=exp(-OD);

% ----------------BEC profile and phase due to detuning---
beam_int=exp(-2*x.^2/width_beam^2);
int_attenuation=(1-(1-amplitude)*exp(-2*x.^2/sigma^2));
Int_att_beam=beam_int.*int_attenuation; Norm=sum(Int_att_beam);
Ex_bec=sqrt(Int_att_beam)/sqrt(Norm);
Ex_bec=Ex_bec.*exp(-i*k*delta*exp(-2*x.^2/sigma^2));

% ---------------- free propagation for z1----------------
% free propagation is convolution of every position x with
% exp(i*k*geo_l) where geo_l=sqrt(x.^2 + z1^2) =z1+1/(2*z1)*x^2 is
% the geometric distance of point x' on final plane at z1 to
% point x on initial plane  (approx: ampl. does not change !)
% convolution = multiplication in k-space !
Ek_bec=fft(Ex_bec); Ek_freeprop=fft(exp(i*k/(2*z1)*x.^2));
% --- shift, so that profile is centered
Ex_before_lens=ifftshift(ifft(Ek_bec.*Ek_freeprop));
```

```
% --------------- phase shift at the lens in real space---
% exp(-i*k*(f_lens+sqrt(f_lens^2+(x-xlens).^2))) is exact,
% numerically its better to use the second order Taylor approx.
phase_lens=exp(-i*k/(2*f_lens)*(x+xlens).^2);
finite_lens=-theta(x-xlens-lens_size/2)+theta(x-xlens+lens_size/2);
Ex_after_lens=Ex_before_lens.*phase_lens.*finite_lens;

% ----------- free propagation for z2 after the lens -----
Ek_after_lens=fft(Ex_after_lens);
Ek_freeprop=fft(exp(i*k/(2*z2)*x.^2));
Ex_ccd=ifftshift(ifft(Ek_after_lens.*Ek_freeprop));

% ------------ calculate normalized intensity ------------
Intensity_ccd=abs(Ex_ccd).^2;
Norm=sum(Intensity_ccd);
Intensity_bec=Intensity_ccd/Norm;

% ----------- and plot it -------------------------------
figure(1);
plot(x/M,Intensity_bec);
axis([-30e-6 30e-6 -inf inf]);
```

A.3 Experiment control software flow diagram

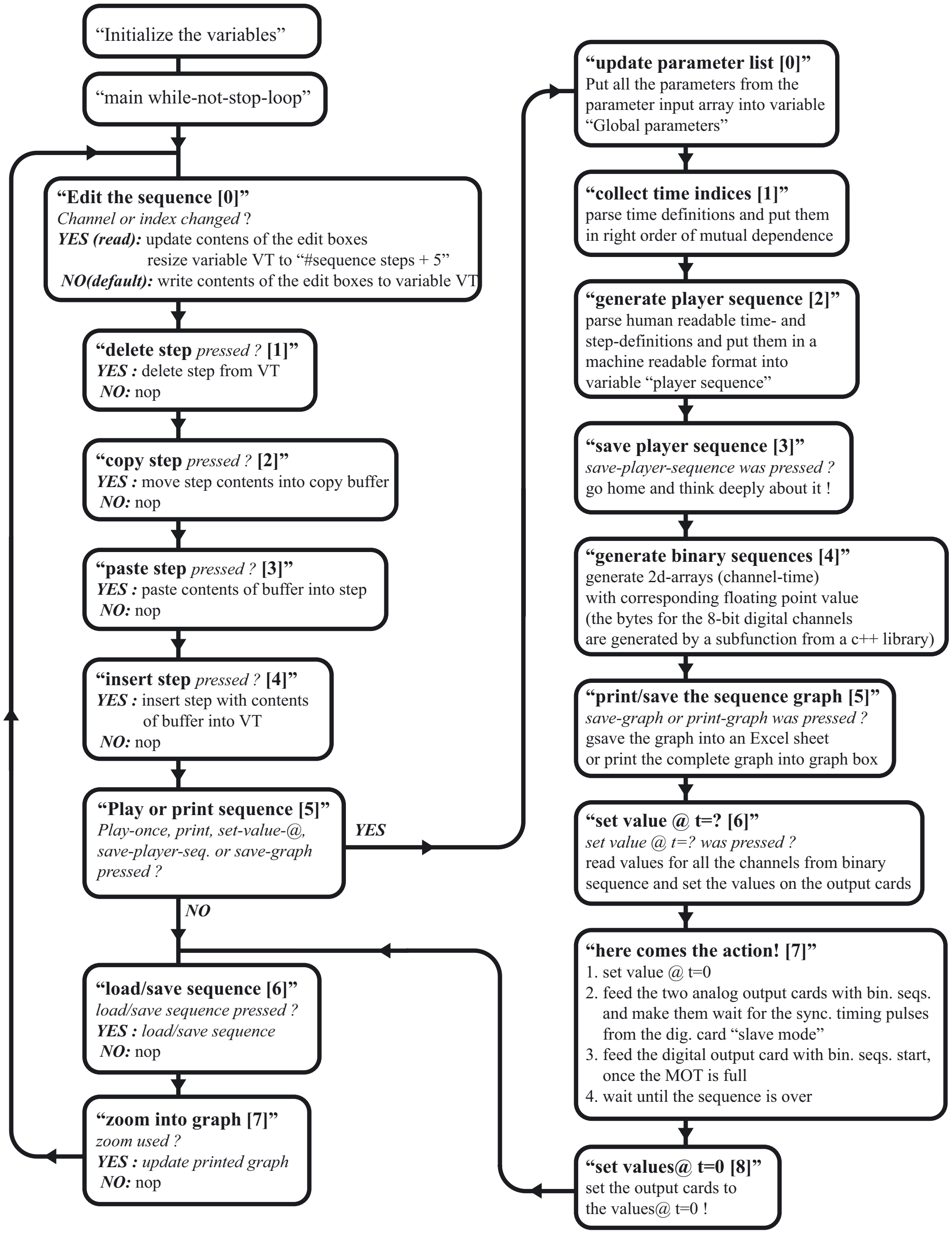

Figure A.1: Flow diagram of the experiment control software written in Labview©. The program can be divided into a main loop (left), which cares about the editing of the human readable experiment sequence, and the "run" part (right), where a binary sequence is generated and executed. The program uses the main variable "VT" for the human readable sequences, and the "player-sequence", where the machine readable sequence is stored.

A.4 Matlab© code to obtain Bloch-bands and Bloch-functions

```
% Calculate Bloch bands E_n(q) and Bloch functions Phi_(n,q)(x)
% --------------------------------------------------------------
s=1.20;                       % Potential depth V_0=s E_r
                              %(energies in units of E_r !!)
Vq=-s/4;                       % coefficients in fourier series of
                              % V(x)=V_0 cos^2(k_l x)
E0=[];E1=[];E2=[];            % clear all arrays
m=15;                         % number of bands -- must be odd !
Q=2;                          % reciprocal lattice vector Q=2 k_l
                              % (all reciprocal vectors in unit of k_l)
K=-(m-1)/2*Q:Q:(m-1)/2*Q;     % reciprocal lat. vectors in Hamilt. matrix
quasimomentum=[-1.5:.05:1.5]; % all quasi momenta q for which
                              % E_(q) is calculated
% ------------ calculate --------------------------------------
for q=quasimomentum;
  H1=diag((q-K).^2);
  H2=diag(ones(m-1,1)*Vq,1);
  H3=diag(ones(m-1,1)*Vq,-1);
  H=H1+H2+H3;                 % generate Hamiltonian matrix H_(m,m')
  [Cq,Eq]=eig(H);             % diagonalize H_(m,m')
                              % -> eigenvalues Eq and eigenvector coeff. Cq
  E0=[E0,Eq(1,1)];            % generate array E(q) for bands 1,2 and 3
  E1=[E1,Eq(2,2)];
  E2=[E2,Eq(3,3)];
end;
% ----------- calculate Bloch function for q=1 -----------
q=1; H1=diag((q-K).^2);
H2=diag(ones(m-1,1)*Vq,1);
H3=diag(ones(m-1,1)*Vq,-1);
H=H1+H2+H3;                   % generate Hamiltonian matrix H_(m,m')
[Cq,Eq]=eig(H);               % diagonalize H_(m,m')

lambda=780e-9;                % periodicity of the potential is lambda/2
dx=lambda/2/100;
x=[-2*lambda/2:dx:2*lambda/2];                  % range in real space
XX=(ones(size(x,2),size(Cq(:,1),1))'*diag(x))'; % generate matrix with m
                                                % columns of x-rows
argument=i*XX*diag(K*2*pi/lambda);              % generate matrix with
                                                % arguments: (i*m*2k*x)
% ------- calc Eigenfunc=exp(iqx)*SUM_m[ exp(-imQx) ] ---------------
eigenfunc=sum((exp(argument)*diag(Cq(:,1)))').*exp(i*q*2*pi/lambda*x);
Neigenfunc=eigenfunc/sqrt(sum(abs(eigenfunc).^2)*dx); % normalize
density=abs(Neigenfunc).^2; % probability density
realpart=real(Neigenfunc);  % real part of eigen function
```

A.5 Matlab© code for the generation of Wannier functions

```
% Calculate Wannier functions from Bloch functions for cosine potential
clear
% physical and system constants
Mass=1.443e-25;         % Mass of 87 Rb Isotop
h=6.626e-34;
hbar=h/2/pi;            % Plank constant
s=3;                    % Potential depth s[E_r] ( V=s*E_r*cos(k*x)^2 )
lambda=783e-9;          % wavelength of the standing wave laser light
d=lambda/2;             % lattice periodicity in real space
k=2*pi/lambda;          % laser light wave vector
N=1e3;                  % Number of points in one period d (N even !)
dx=d/N;                 % sampling in real space
x=[-4.5*N*dx:dx:4.5*N*dx]; % x-range in real space
wannier=zeros(size(x)); % "empty" wannier state
J=11;                   % Number of Bloch Bands (J odd!)
Ks=2;                   % Periodicity in reciprocal lattice [k_laser]
K=-(J-1)/2*Ks:Ks:(J-1)/2*Ks; % reciprocal lattice vectors
q=s/4;                  % fourier coefficient of lattice potential [E_r]

%---------------- 1. generate Bloch functions "phi=exp(iqx)*u_q"
%----------------    for all quasi momenta q in a Brillouin zone
%---------------- 2. generate Wannier functions
%----------------    w=sum_q[ exp(-i q x_0)* phi_q] @ x=x_0
dm=0.001;               %sampling of q in a Brillouin zone
for m=[-1:dm:1];
    M1=diag((m-K).^2);
    M2=diag(ones(J-1,1)*q,1);
    M3=diag(ones(J-1,1)*q,-1);
    M=M1+M2+M3;
    [Ck,Ek]=eig(M);
    n=1;
    u_q=zeros(size(x));
    for l=(-(J-1)/2:(J-1)/2); % generate u_q
        u_q=u_q+Ck(n,1)*exp(-i*l*2*k*x);
        n=n+1;
    end;
    phi=exp(i*m*k*x).*u_q; % generate Bloch function phi_q
    phi=phi*exp(-i*angle(phi(round(size(phi,2)/2)))); % !! important !!
                        % assure that the global phase
                        % of phi_q = 0 for all q at x=0 !!
    wannier=wannier+exp(-i*m*k*lambda/4).*phi; % generate Wannier function
end;
Norm=sqrt(sum(abs(wannier).^2)*dx); % normalization
wannier=wannier/Norm;
```

A.6 Matlab© code for the wave packet propagation with the DNL

```
% Propagate 1D DNL with Runge-Kutta function "ode45"
function Propagate_DNL

%--------------- physical constants
h=6.626e-34;
hbar=h/2/pi;                            % Plank constant
m=1.443e-25;                            % Mass of 87Rb Isotop
a=5.6124e-009;                          % scattering length 87Rb
lambda=783e-9;                          % wavelength d2 line
omega_r=hbar*(2*pi/lambda)^2/2/m;       % recoil frequency
E_r=hbar*omega_r;                       % recoil energy
d=lambda/2*1e6;                         % inter well distance [m]
DimPsi=501;                             % Number of Wells !ODD!
xrange=[-d*(DimPsi-1)/2:d:d*(DimPsi-1)/2];
                                        % hole x-range [m]

%--------------- experimental parameters
s=12;                                   % lattice potential depth [E_r]
omega_perp=230*2*pi;                    % transverse frequency of waveguide
omega_long=0.500*2*pi;                  % longitudinal frequency of waveguide
N=5000;                                 % total number of atoms
TOF=50e-3;                              % propagation time [s]
sigma_xwave=10;                         % width of the initial. w-packet [m]

%--------------- build wave function
PSI=(exp(-xrange.^2/sigma_xwave^2))';   % initial wave function
Norm=sqrt(sum(abs(PSI).^2));            % well ...
PSI=PSI/Norm*sqrt(N);
PSI_in=PSI;                             % start wave function for the propagation
%Psis=[];
PSI_save=zeros(100,DimPsi);             % array where the  wave f's are stored

%--------------- calculate relevant values for the propagation of the DNL
omega_latt=2*omega_r*sqrt(s);           % approx. harmonic frequency in one well
sigma_x=sqrt(hbar/m/omega_latt);        % long. length of wave f. in single well
eps=(0.5*m*omega_long^2*xrange.^2*1e-12/hbar)';
                                        % on-site energies
U_1=sqrt(m*omega_perp^2*4*pi*a/m/(sqrt(2*pi)*pi*sigma_x));
                                        % nonlinear par. U1
%K=E_bandwidth(s)/4/hbar;               % tunn. energy K, calc. with Band width
K=4/sqrt(pi)*omega_r*s^(3/4)*exp(-2*sqrt(s));
                                        % alternative: K from ref: "w. Zwerger"
```

```
%--------------- the propagation with 100 intermediate saved time steps
options=odeset('RelTol',3e-8,'AbsTol',1e-8,'Stats','off','MaxStep',1e-5);
dt=TOF/99;                              % time between two saved time steps
for counter=1:100
    [TT,PSI_out]=ode45(@DGLFUNC,[0 dt/2 dt],PSI_in,options);
                                        % solve DNL for one time step dt
    PSI_in=PSI_out(3,:);                % start function for next time step
    subplot(2,2,2);                     % plot |psi|^2
    plot(xrange,abs(PSI_in).^2,xrange,abs(PSI).^2,'r');
    title(['Prop. time = ' num2str(counter*dt*1e3,4) ' ms / ' ...
        num2str(counter*dt/TOF*100,3) ' %']);
    xlabel('lattice site n');
    subplot(2,2,4);                     % plot angle(psi)
    plot(xrange,unwrap(angle(PSI_in))/2/pi);
    title('angle [2\pi]');
    xlabel('lattice site n');
    PSI_save(counter,:)=PSI_out(3,:);   % save time step
    drawnow;
end;

%--------------- calculate and plot the rms-width versus time
rms_width=zeros(length(TT),1); for t=1:100
    PSI_out2=abs(PSI_save(t,:)).^2;
    Ewx=sum(PSI_out2.*xrange)/sum(PSI_out2);
    Erw2x=sum(PSI_out2.*(xrange.^2))/sum(PSI_out2);
    Var=2*sqrt(Erw2x-Ewx^2);
    rms_width(t)=Var;
end; subplot(1,2,1); plot([0:dt:TOF]*1e3,rms_width/2);
xlabel('Propagation time [ms]'); ylabel('rms-Width [m]');

%--------------- save data
%filename=['testS10N5000_DNL.mat'];
%save(filename)

%--------------- nested DNL function
    function DPSI= DGLFUNC(t,PSI);
        psi_j=PSI;
        psi_jm1=[0; PSI(1:DimPsi-1); ];
        psi_jp1=[PSI(2:DimPsi); 0;];
        DPSI=-i*(eps+U_1*abs(psi_j)).*psi_j+i*K*(psi_jm1+psi_jp1);
    end % DGLFUNC

end % Propagate_DNL
```

A.7 Matlab© code for propagation of the two-mode DGL's for double well MQST

```
% --- Propagate double well macroscopic self-trapping DGL for population
% --- imbalance z and relative phase phi with Runge-Kutta function "ode45"
function Propagate_MQST_DGL
%-------------- experimental parameters
TOF=5.0;                % propagation time [tunneling time hbar/2K]
z0=.6;                  % initial fractional imbalance
phi0=-0*pi;             % initial relative phase
%-------------- build initial function (point in phase plane)
PSI=[z0;phi0];          % initial coordinates in phase plane
PSI_in=PSI;             % start function for the propagation
phi_save=zeros(1000,1); % array for time series of phase_point's
z_save=zeros(1000,1);   % array for time series of imbalance_points's
%-------------- calculate relevant values for the propagation of the DNL
Lambda_c=(1+sqrt(1-z0^2)*cos(phi0))*2/z0^2; % Lambda critiacal
Lambda_s=1/sqrt(1-0.6^2);                   % Lambda stationary
Lambda=Lambda_c*0.991;                      % Lambda for DGL
%-------------- the propagation with 1000 intermediate saved time steps
options=odeset('RelTol',3e-8,'AbsTol',1e-8,'Stats','off','MaxStep',1e-4);
dt=TOF/999;             % time between two saved time steps
for counter=1:1000  % solve DGL
    [TT,PSI_out]=ode45(@twomodeDGLFUNC,[0 dt/2 dt],PSI_in,options);
    PSI_in=[PSI_out(3,1);PSI_out(3,2)]; % start function for next time step
    phi_save(counter)=PSI_out(3,2);
    z_save(counter)=PSI_out(3,1);
    plot(phi_save/pi,z_save,'-r');
    axis([-2 2 -1 1]);
    title(['Prop. time = ' num2str(counter*dt,2) ' T_{tunnel} / ' ...
        num2str(counter*dt/TOF*100,3) ' %']);
    xlabel('relative phase \phi');
    ylabel('population imbalance z');
    drawnow;
end;

%-------------- save data
filename=['2mode_z0_0.6_phi0_0Lc0.91.mat'];
save(filename)

%-------------- nested DGL function
    function DPSI= twomodeDGLFUNC(t,PSI);
        DPSI=[-sqrt(1-PSI(1)^2)*sin(PSI(2)) ; ...
              Lambda*PSI(1)+PSI(1)/sqrt(1-PSI(1)^2)*cos(PSI(2))];
    end % twomodeDGLFUNC
end % Propagate_MQST_DGL
```

Bibliography

G.P. Agrawal. *"Applications of Nonlinear Fiber Optics"*, Academic Press, San Diego, 2nd edition, (2001).

G.P. Agrawal. *"Nonlinear Fiber Optics"*, Academic Press, San Diego, (1995).

V. Ahufinger, A. Sanpera, P. Pedri, L. Santos, and M. Lewenstein. *"Creation and mobility of discrete solitons in Bose-Einstein condensates"*, Phys. Rev. A **69**, 053604 (2004).

M. Albiez, R. Gati, J. Fölling, S. Hunsmann, M. Cristiani, and M.K. Oberthaler. *"Direct Observation of Tunneling and Nonlinear Self-Trapping in a Single Bosonic Josephson Junction"*, Phys. Rev. Lett. **95**, 010402 (2005).

E. Altman, A. Polkovnikov, E. Demler, B.I. Halperin, and M.D. Lukin. *"Superfluid-Insulator Transition in a Moving System of Interacting Bosons"*, Phys. Rev. Lett. **95**, 020402 (2005).

B.P. Anderson and M. Kasevich. *"Macroscopic quantum interference from atomic tunnel arrays"*, Science **282**, 1686 (1998).

M.H. Anderson, J.R. Ensher, M.R.Matthews, C.E.Wieman, and E.A. Cornell. *"Observation of Bose-Einstein condensation in a dilute atomic vapor"*, Science **269**, 198 (1995).

M. R. Andrews, C. G. Townsend, H.-J. Miesner, D. S. Durfee, D. M. Kurn, W. Ketterle. *"Observation of Interference Between Two Bose Condensates"*, Science **275**, 637 (1997).

Th. Anker, M. Albiez, B. Eiermann, M. Taglieber and M. K. Oberthaler. *"Linear and nonlinear dynamics of matter wave packets in periodic potentials"*, Optics Express **12**, 11 (2003).

Th. Anker, M. Albiez, R. Gati, S. Hunsmann, B. Eiermann, A. Trombettoni and M. K. Oberthaler. *"Nonlinear self-trapping of matter waves in periodic potentials"*, Phys. Rev. Lett. **94**, 020403 (2005).

M. Arndt , O. Nairz, J. Voss-Andreae, C. Keller, G. van der Zouw and A. Zeilinger. *" Wave-particle duality of C60"*, Nature **401**, 680-682 (1999).

N. W. Ashcroft and N. D. Mermin. *"Solid state physics"*, Saunders College Publishing, Fort Worth, (1976).

G. Baym and C. J. Pethick *"Ground-State Properties of Magnetically Trapped Bose-Condensed Rubidium Gas"*, Phys. Rev. Lett. **76**, 6 (1996).

B. Paredes, A. Widera, V. Murg, O. Mandel, S. Fölling, I. Cirac, G.V. Shlyapnikov, T.W. Hänsch and I. Bloch. *"Tonks–Girardeau gas of ultracold atoms in an optical lattice"*, Nature **429**, 277 (2004).

I. Bloch, T. W. Hänsch, and T. Esslinger. *"Atom Laser with a cw Output Coupler"*, Phys. Rev. Lett. **82**, 3008 (1999).

N. Bogoliubov. *"On the theory of superfluidity"*, J. Phys. **11**, 23 (1947).

S. N. Bose. *"Plancks Gesetz und Lichtquantenhypothese"*, Zeitschrift für Physik, 26 (1924).

D. Braun, F. Haake, and W.T. Strunz. *"Universality of Decoherence"*, Phys. Rev. Lett. **86**, 2913 (2001).

S. Burger, K. Bongs, S. Dettmer, W. Ertmer, K. Sengstock, A. Sanpera, G.V. Shlyapnikov, and M. Lewenstein. *"Dark solitons in Bose-Einstein condensates"*, Phys. Rev. Lett. **83**, 5198 (1999).

S. Burger, F.S. Cataliotti, C. Fort, F. Minardi, M. Inguscio, M.L. Chiofalo, and M.P. Tosi. *"Superfluid and dissipative dynamics of a Bose-Einstein condensate in a periodic optical potential"*, Phys. Rev. Lett. **86**, 4447 (2001).

O. Carnal and J. Mlynek. *"Young's double-slit experiment with atoms: A simple atom interferometer"*, Phys. Rev. Lett. **77**, 5315 (1991).

Y. Castin and R. Dum. *"Bose-Einstein Condensates in Time Dependent Traps"*, Phys. Rev. Lett. **77**, 5315 (1996).

F.S.Cataliotti, S. Burger, C. Fort, P. Maddaloni, F. Minardi, A. Trombettoni, A. Smerzi, M. Inguscio. *"Josephson Junction Arrays with Bose-Einstein Condensates"*, Science **293**, 843 (2001).

S. Chu, L. Hollberg, J. E. Bjorkholm, A. Cable, and A. Ashkin. *"Three-dimensional viscous confinement and cooling of atoms by resonance radiation pressure"*, Phys. Rev. Lett. **55**, 48 (1985).

D. Clément, A.F. Varón, M. Hugbart, J.A. Retter, P. Bouyer, L. Sanchez-Palencia, D.M. Gangardt, G.V. Shlyapnikov, and A. Aspect. *"Suppression of Transport of an Interacting Elongated Bose-Einstein Condensate in a Random Potential"*, cond-mat/00005568 (2005).

C. N. Cohen-Tannoudji. *"Manipulating atoms with photons"*, Rev. Mod. Phys. **70** (1998).

C. Cohen-Tannoudji, J. Dupont-Roc und G. Grynberg. *"Atom-Photon Interactions, Basic Processes and Applications"* Wiley-Interscience (1992).

M.B. Dahan, E. Peik, J. Reichel, Y. Castin and C. Salomon. *"Bloch oscillations of atoms in an optical potential"* Phys. Rev. Lett. **76**, 4508 (1996).

J. Dalibard and C. Cohen-Tannoudji. *“Laser cooling below the doppler limit by polarization gradients: simple theoretical models”* J. Opt. Soc. Am. B **6**, 2023 (1989).

F. Dalfovo, S. Giorgini, L. P. Pitaevskii, and S. Stringari. *“Theory of Bose-Einstein condensation in trapped gases”*, Rev. Mod. Phys. **71**(3), 463 (1999).

S. Darmanyan, A. Kobyakov, F. Lederer, L. Vazquez. *“Discrete fronts and quasirectangular solitons”*, Phys. Rev. B **59**, 5994 (1999).

K. B. Davis, M.-O. Mewes, M. R. Andrews, N. J. van Druten, D. S. Durfee, D. M. Kurn, and W. Ketterle *“Bose-Einstein Condensation in a Gas of Sodium Atoms”*, Phys. Rev. Lett. **75**, 3969 (1995).

L. Deng, E. W. Hagley, J.Wen, M. Trippenbach, Y. Band, P. S. Julienne, J. E. Simsarian, K. Helmerson, S. L. Rolston and W. D. Phillips. *“Four-wavemixing with matterwaves”*, Nature **398**, 218 (1999).

K. Dieckmann, R.J.C. Spreeuw, M. Weidemüller, and J.T.M Walraven. *“Two-dimensional magneto-optical trap as a source of slow atoms”*, Phys. Rev. A **58**, 3891 (1998).

B. Eiermann, P. Treutlein, Th. Anker, M. Albiez, M. Taglieber, K.-P. Marzlin, and M. K. Oberthaler. *“Dispersion Management for Atomic MatterWaves”* Phys. Rev. Lett. **91**, 060402 (2003).

B. Eiermann, Th. Anker, M. Albiez, M. Taglieber, P. Treutlein, K.-P. Marzlin and M. K. Oberthaler. *“ Bright Bose-Einstein Gap Solitons of Atoms with Repulsive Interaction”* Phys. Rev. Lett. **92**, 230401 (2004).

B. Eiermann. *“Kohärente nichtlineare Materiewellendynamik - Helle atomare Solitonen”*, PhD thesis at the University of Konstanz (2004).

A. Einstein. *“Quantentheorie des einatomigen idealen Gases”*, Zweite Abhandlung. Sitzungber. Preuss. Akad. Wiss., 3 (1925).

S.A. Gardiner, D. Jaksch, R. Dum, J.I. Cirac, and P. Zoller. *“Nonlinear matter wave dynamics with a chaotic potential”*, Phys. Rev. A **62**, 023612 (2000).

R.M. Godun, M.B. D’Arcy, G.S. Summy and K. Burnett. *“Prospects for atom interferometry”*, Contemp. Phys. **42**, 77 (2001).

M. Greiner, I. Bloch, O. Mandel, T.W. Hänsch, and Tilman Esslinger. *“Exploring Phase Coherence in a 2D Lattice of Bose-Einstein Condensates”*, Phys. Rev. Lett. **87**, 160405 (2001).

M. Greiner, O. Mandel, T. Esslinger, T.W. Hänsch und I. Bloch. *”Quantum phase transition from a superfluid to a Mott insulator in a gas of ultracold atoms”*, Nature **415**, 39 (2002).

M. Greiner. *“Ultracold quantum gases in three-dimensional optical lattice potentials”*, PhD thesis at the Ludwig-Maximilians-Universität München (2003).

M.P.A. Fisher, P. B. Weichman, G. Grinstein, D. S. Fisher. *“Boson localization and the superfluid-insulator transition”*, Phys. Rev. B **40**, 546 (1989).

J. H. Denschlag, J.E. Simsarian, H. Häffner, C. McKenzie, A. Browaeys, D. Cho, K. Helmerson, S.L. Rolston and W.D. Phillips. *“A BoseEinstein condensate in an optical lattice”*, J. Phys. B **35**, 3095 (2002).

S. Inouye, M.R. Andrews, J. Stenger, H.-J. Miesner, D.M. Stamper-Kurn, and W. Ketterle. *"Observation of Feshbach resonances in a Bose-Einstein condensate"*, Nature **392**, 151 (1998).

D. Jaksch, C. Bruder, J. I. Cirac, C.W. Gardiner, and P. Zoller. *“Cold bosonic atoms in optical lattices”*, Phys. Rev. Lett. **81**, 3108 (1998).

D. Jaksch, H.-J. Briegel, J.I. Cirac, C.W. Gardiner, and P. Zoller. *“Entanglement of Atoms via Cold Controlled Collisions”*, Phys. Rev. Lett. **82**, 1975 (1999).

M. Jona-Lasinio, O. Morsch, M. Cristiani, N. Malossi, J. H. Müller, E. Courtade, M. Anderlini, and E. Arimondo. *“Asymmetric Landau-Zener Tunneling in a Periodic Potential”*, Phys. Rev. Lett. **91**, 230406 (2003).

D. W. Keith, M. L. Schattenburg, Henry I. Smith, and D. E. Pritchard. *“Diffraction of Atoms by a Transmission Grating”*, Phys. Rev. Lett. **61**, 1580 (1988).

W. Ketterle, D.S. Durfee, D.M. Stamper-Kurn. *“Making, probing and understanding Bose-Einstein condensates”*, Proceedings of the Varenna conference on Bose-Einstein condensation, July 1998 and cond-mat/9904034.

L. Khaykovich, F. Schreck, F. Ferrari, T. Bourdel, J. Cubizolles, L.D. Carr, Y. Castin, and C. Salomon. *“Formation of a matter wave bright soliton”*, Science **296**, 1290 (2002).

B.G. Klappauf, W.H. Oskay, D.A. Steck and M.G. Raizen. *“...”*, Phys. Rev. Lett. **81**, 1203 (1998).

A. Klöckner *“On the Computation of Maximally Localized Wannier Functions”*, Diploma Thesis, University of Karlsruhe, (2004).

M. Kozuma, L. Deng, E.W. Hagley, J. Wen, R. Lutwak, K. Helmerson, S.L. Rolston, and W.D. Phillips. *“Coherent splitting of Bose-Einstein condensed atoms with optically induced bragg diffraction”*, Phys. Rev. Lett. **82**, 871 (1999).

F. London. *“On the Bose-Einstein condensation”*, Phys. Rev. **54**, 947 (1938).

K.W. Madison, F. Chevy, W. Wohlleben, and J. Dalibard. *“Vortex Formation in a Stirred Bose-Einstein Condensate”*, Phys. Rev. Lett. **84**, 806 (2000).

E. Majorana. Nuovo Cimento **9**, 43 (1932).

N. Masuhara, J. M. Doyle, J. C. Sandberg, D. Kleppner, T. J. Greytak, H. F. Hess, and G. P. Kochanski. *“Evaporative Cooling of Spin-Polarized Atomic Hydrogen”*, Phys. Rev. Lett. **61**, 935 (1988).

A. Messiah. *"Quantenmechanik"*, Volume 2. ,de Gruyter, Berlin, (1990).

H. J. Metcalf, P. Straten *"Laser Cooling and Trapping"*, Springer Verlag, (1999).

M.-O. Mewes, M. R. Andrews, D. M. Kurn, D. S. Durfee, C. G. Townsend, and W. Ketterle. *"Output Coupler for Bose-Einstein Condensed Atoms"*, Phys. Rev. Lett. **78**, 582 (1997).

P. Meystre. *"Atom Optics"*, Springer Series on Atomic, Optical, and Plasma Physics, Vol. **33**, Springer Verlag (2001).

G.J. Milburn, J. Corney, E.M. Wright, D.F. Walls. *"Quantum dynamics of an atomic Bose-Einstein condensate in a double-well potential"*, Phys. Rev. A **55**, 4318 (1997).

L.F. Mollenauer, R.H. Stolen, and J.P. Gordon. *"Experimental observation of picosecond pulse narrowing and solitons in optical fibers"*, Phys. Rev. Lett. **45**, 1095 (1980).

F.L. Moore, J.C. Robinson, C.F. Bharucha, B. Sundaram, and M.G. Raizen. *"Atom Optics Realization of the Quantum δ-Kicked Rotor"*, Phys. Rev. Lett. **75**, 4598 (1995).

W. Nolting *"Grundkurs Theoretische Physik: 5 Quantenmechanik"*, Friedr. Vieweg & Sohn Verlag, (1997).

W. Petrich, M. H. Anderson, J.R. Ensher, and E. A. Cornell. *"Behaviour of atoms in a compressed magneto-optical trap"*, J. Opt. Soc. Am. B **11**, 1332 (1994).

W. Petrich, M. H. Anderson, J. R. Ensher, and E. A. Cornell. *"Stable, Tightly Confining Magnetic Trap for Evaporative Cooling of Neutral Atoms"*, Phys. Rev. Lett. **74**, 3352 (1995).

H. Pu, L. O. Baksmaty, W. Zhang, N.P. Bigelow, and P. Meystre. *"Effective-mass analysis of Bose-Einstein condensates in optical lattices: Stabilization and levitation"*, Phys. Rev. A **67**, 043605 (2003).

E. L. Raab, M. Prentiss, A. Cable, S. Chu, and D.E. Pritchard. *"Trapping of neutral sodium atoms with radiation pressure"*, Phys. Rev. Lett. **59**, 2631 (1987).

S. Raghavan, A. Smerzi, S. Fantoni, and S.R. Shenoy. *"Coherent oscillations between two weakly coupled Bose-Einstein condensates: Josephson effects, p oscillations, and macroscopic quantum self-trapping"*, Phys. Rev. A **59**, 620 (1998).

E. Riis, D.S. Weiss, K.A. Moler, and S. Chu. *"Atom funnel for the production of a slow, high-density atomic beam"*, Phys. Rev. Lett. **64**, 1658 (1990).

J.S. Russell. *"Report on Waves"*, Report of the 14th Meeting of the British Association for the Advancement of Science. London 311 (1844).

L. Salasnich, A. Parola, and L. Reatto. *"Effective wave equations for the dynamics of cigar-shaped and disk-shaped Bose condensates"*. Phys. Rev. A **65**, 043614 (2002).

Y. Shin, M. Saba, T. A. Pasquini, W. Ketterle, D. E. Pritchard, and A. E. Leanhardt. *"Atom Interferometry with Bose-Einstein Condensates in a Double-Well Potential"*, Phys. Rev. Lett. **92**, 050405 (2004).

A. Smerzi, S. Fantoni, S. Giovannazzi, and S.R. Shenoy. *"Quantum Coherent Atomic Tunneling between Two Trapped Bose-Einstein Condensates"*, Phys. Rev. Lett. **79**, 4950 (1997).

A. Smerzi and A. Trombettoni. *"Nonlinear tight-binding approximation for Bose-Einstein condensates in a lattice"*, Phys. Rev. A **68**, 023613 (2003).

A. Smerzi and A. Trombettoni. *"Discrete nonlinear dynamics of weakly coupled Bose-Einsein condensates"*, Chaos **13**, 766 (2003).

D. M. Stamper-Kurn, M. R. Andrews, A. P. Chikkatur, S. Inouye, H.-J. Miesner, J. Stenger, and W. Ketterle. *"Optical Confinement of a Bose-Einstein Condensate"*, Phys. Rev. Lett. **80**, 2027 (1998).

M.J. Steel and W. Zhang. *"Bloch function description of a Bose-Einstein condensate in a finite optical lattice"*, arXiv:cond-mat/9810284, (1998).

C.M. de Sterke and J.E. Sipe. *"Application of the split operator fourier transform method to the solution of the nonlinear Schrodinger equation"*, AIP Conference Proceedings **160**, 269 (1986).

K.E. Strecker, G.B. Partridge, A.G. Truscott, and R.G. Hulet. *"Formation and propagation of matter wave soliton trains"*, Nature **417**, 150 (2002).

G. Timp, R. E. Behringer, D. M. Tennant, and J. E. Cunningham. *"Using light as a lens for submicron, neutral-atom lithography"*, Phys. Rev. Lett. **69**, 1636 (1992).

P. Treutlein. *"Dispersionsmanagement für Materiewellen"*. Diplomarbeit, Universität Konstanz, (2002).

A. Trombettoni. Private communication, (2004).

A. Trombettoni and A. Smerzi. *"Discrete Solitons and Breathers with Dilute Bose-Einstein Condensates"*, Phys. Rev. Lett. **86**, 2353 (2001).

W.H. Zurek. *"Decoherence and the transition from quantum to classical"*, Phys. Today **44**, 36 (1991).

W. Zwerger. *"Mott-Hubbard transition of cold atoms in optical lattices"*, J. Opt. B **5**, S9 (2003).

Danksagung

An dieser Stelle möchte ich mich bei allen Personen bedanken, die zum Gelingen dieser Arbeit beigetragen haben. Mein spezieller Dank gilt dabei:

Prof. Markus Kurt Oberthaler, der mir die Gelegenheit gegeben hat, an einem spannenden und exzellent ausgestatteten Experiment mitzuarbeiten. Die Arbeit in seiner Gruppe war geprägt von der Faszination an der Physik und dem Glauben an den Erfolg. Sein Enthusiasmus, seine Energie und seine Großzügigkeit waren für mich immer erstrebenswerte Tugenden.

Prof. Jörg Schmiedmayer, der sich bereit erklärt hat, die vorliegende Arbeit zu begutachten.

Meinem Mitdoktoranden Bernd Eiermann, der mir immer ein geduldiger Zuhörer war, bei meinen philosophischen Ausschweifungen. Danken möchte ich ihm für die spannenden Diskussionen, die stimmige Zusammenarbeit, die langen Nächte, das erste Kondensat, die geteilte Freude und das geteilte Leid. Wir sind einen langen und wichtigen Lebensabschnitt zusammen gelaufen und ich habe ihn als Partner sehr schätzen gelernt.

Meinem Mitdoktoranden Michael Albiez, mit dem ich durch Himmel und Hölle ging. Unsere beiden Holzköpfe stießen oft aneinander, doch zurück bleibt die Erinnerung an die vielen gesungenen Lieder und die Freude an gemeinsamen Erfolgen. Sein "Dampf" und sein Humor machten die Arbeit im Labor zum Fest.

Meinem Kollegen Ralf Stützle für die häufige lebensrettende Hilfe in "bürokratischer" Not. Sein trockener Humor wird mir immer in Erinnerung bleiben.

Unseren Hiwis Alex Weber und Jiri Tomkovic. Alex verdanke ich die numerische Fourier-Optik und Jiri den schnellen Wiederaufbau der "Maschine" in Heidelberg.

Den Diplomanden Karen Forberich, Philipp Treutlein, Matthias Taglieber und Stefan Hunsmann, dem späteren Mitdoktoranden Rudolf Gati, sowie den Post-Docs Marie-Jo Bellanca und Björn Brezger, die alle zum Erfolg dieser Arbeit beigetragen haben.

Den anderen Gruppenmitgliedern der Atomoptikgruppe: Martin Göbel, Alex Greiner, Anja Habenicht, Thomas Hörner, Lisa Kierig, Dirk Jürgens, Igor Mourachko und Martin Störzer. Sie waren stets hilfsbereite und freundliche Kollegen.

Unseren Nachbarn Oliver Vogelsang und Dennis Weise. Ohne ihr Laserlicht und ihr gut sortiertes Labor wäre so manches Experiment zum Scheitern verurteilt gewesen.

Allen wissenschaftlichen und nicht-wissenschaftlichen Mitarbeitern der Universitäten Konstanz und Heidelberg. Der spezielle Dank gilt dabei Ute Hentzen und Stefan Eggert. Bei letzterem habe die Elektronik lieben gelernt.

Mein innigster Dank gilt meiner Frau Barbara Boldrini. In endlosen wissenschaftlichen Diskussionen stand sie mir mit ihrer Erfahrung und ihrem Rat zur Seite. Bei allen menschlichen Problemen war sie ein treuer Partner. Mit ihrer Liebe und ihrer Freude konnte ich meinen Energietank immer wieder neu füllen und mit neuer Kraft voranschreiten.

Mein weitester Dank gilt meiner Mutter. Durch ihr Vorbild lernte ich, die Schönheit dieser Welt zu sehen und zu erforschen.